Computational Analysis Techniques using Fast Radio Bursts to Probe Astrophysics

E. Platts

Supervised by A. Weltman and J. P. Shock

A Thesis Presented for the Degree of
Doctor of Philosophy in Applied Mathematics

Department of Mathematics and Applied Mathematics
The University of Cape Town
South Africa
December 2020

Abstract

This thesis focuses on Fast Radio Bursts (FRBs) and presents computational techniques that can be used to understand these enigmatic events and the Universe around them. Chapter 1 provides a theoretical overview of FRBs; providing a foundation for the chapters that follow. Chapter 2 details current understandings by providing a review of FRB properties and progenitor theories. In Chapter 3, we implement non-parametric techniques to measure the elusive baryonic halo of the Milky Way. We show that even with a limited data set, FRBs and an appropriate set of statistical tools can provide reasonable constraints on the dispersion measure of the Milky Way halo. Further, we expect that a modest increase in data (from fewer than 100 FRB detections to over 1000) will significantly tighten constraints, demonstrating that the technique we present may offer a valuable complement to other analyses in the near future. In Chapter 4, we study the fine time-frequency structure of the most famous FRB: FRB 121102. Here, we use autocorrelation functions to maximise the structure of 11 pulses detected with the MeerKAT radio telescope. The study is motivated by the low time-resolution of MeerKAT data, which presents a challenge to more traditional techniques. The burst profiles that are unveiled offer unique insight into the local environment of the FRB, including a possible deviation from the expected cold plasma dispersion relationship. The pulse features and their possible physical mechanisms are critically discussed in a bid to uncover the nature and origin of these transients.

Acknowledgements

Firstly I would like to thank my supervisors, Amanda Weltman and Jonathan Shock, without whom this would not have been possible. Amanda, thank you for all the support you have given me over the years, for your belief in me, and for the amazing opportunities you have given me. Jon, thank you for always being there for me and for enthusiastically sharing your knowledge and expertise with me.

Thank you to Xavier Prochaska, my supervisor at the 2019 Kavli Summer Program in Astrophysics (KSPA) at the University of California, Santa Cruz (UCSC). Thank you for the time and care you took in teaching me. Thank you also inviting me to join the Fast and Fortunate for FRB Follow-up (F^4) team[1]—such a wonderful group of people whom I shall certainly miss.

Thank you to all others I collaborated with, especially (in order of appearance in my life) Shriharsh Tendulkar, Casey Law, Manisha Caleb, Ben Stappers and Kasper Heintz. You were all such fun to work with and taught me so much.

Regarding software installation: thank you to Kaustubh Rajwade for the hours spent trying to help me set up SIGPROC on my laptop, and thank you to Rob Lyon for writing the Docker image that I ended up using at Kaustubh's suggestion.[2] Regarding coding issues: thank you to Stack Exchange and to all those that contribute.

Thank you to the students and post-doctorates in the High Energy Physics, Cosmology and Astrophysics Theory (HEPCAT) group.[3] Thank you for the memes, the drinks and the laughs.

Thank you to all the students at the 2019 Kavli Summer Program—an inspiring and humble group of individuals. I cannot wait to see what you all go on to achieve.

Thank you to my friends. Jess, thank you for being there for me, even from a far. Your strength is an inspiration and our friendship brightens my days. Ash, thank you for your for kindness and for always being there. Jay Jay: thank you for our coffees and adventures over the years—they mean more than you know and I cannot wait till we live closer together again. Dani, Felix, Jimmy, Jono, Nicole, Tom, Will: thank you for the drinks, the dinners, the braais, the boardies and the betrayals.

Finally, thank you to my family. To my late dad, who inspired me to love physics and maths from a young age: growing up, I thought I would be a medical doctor like you, but I suppose this is close enough. I miss you so much. To my mum: thank you for all the sacrifices you have made for me over the years and for your undying support and encouragement. Thank you for helping me to believe in myself and for being there for me when the wheels fall off. To my little brother, Al: thank you for grounding me and always helping me to see the light. You're an inspiration to me and I'm so proud of you. To my cousin, Sammy: thank you for your support, love and kindness, and for humbly accepting when I beat you at cards. And to my partner Chace: thank you for everything. For always making me laugh, even when I think I'm falling apart; for helping me see the bigger picture; for believing in me; and for making me so happy through it all. I love you all.

[1] https://sites.google.com/ucolick.org/f-4
[2] https://github.com/scienceguyrob/Docker/tree/master/Images/pulsardsd
[3] http://hepcat.group

"Science over glory."

– J. P. Macquart

Declaration

The content of this thesis is based on collaborations with the following individuals:

A. Weltman,[1] J. P. Shock,[1] J. X. Prochaska,[2] C. J. Law,[3] M. Caleb,[4] B. W. Stappers,[4] S. P. Tendulkar,[5] R. A. Main,[6] G. E. B. Jordin,[1] A. Walters,[7] and S. Kandhai.[1]

[1] *University of Cape Town, South Africa*
[2] *University of California Santa Cruz, USA*
[3] *California Institute of Technology, USA*
[4] *University of Manchester, UK*
[5] *McGill University, Canada*
[6] *Max-Planck-Institut für Radioastronomie, Germany*
[7] *University of KwaZulu-Natal, South Africa*

In particular, the following sections are associated with publications:

Chapter 2.3: Platts E., Weltman A., Walters A., Tendulkar S. P., Gordin J. E. B., Kandhai S., 2019, Physics Reports, 821, 1

Chapter 3 : Platts E., Prochaska J. X., Law C. J., 2020, Astrophysical Journal Letters, 895, L49

Chapter 4 : Platts E., Caleb M., Stappers B. W., Main R. A., Weltman A., Shock J. P., et al., in preparation

I am also a co-author in the two papers listed below. I detail my contribution to the first in §2.1.7. The second is Paper I of Platts et al. (2021). Here, I provided some results necessary for calculations in Paper I, but that are only presented in Paper II.

i. Heintz K. E., Prochaska J. X., Simha S., Platts E., Fong W.-F, Tejos N., Ryder S. D., et al., 2020, Astrophysical Journal, 903, 2

ii. Caleb M., Stappers B. W., Abbott T. D., Barr E. D., Bezuidenhout M. C., Buchner S. J., et al, 2020, Monthly Notices of the Royal Astronomical Society, 496, 4

I hereby declare that this thesis has not been submitted, either in the same or different form, to this or any other university for a degree and that it represents my own work.

Emma Danielle Platts
PhD Candidate

Date

Contents

List of Figures

List of Tables

Preface

Discovered in 2007, Fast Radio Bursts (FRBs) are one of the newest enigmas to grace astronomy. With only ∼120 observed to date, little has been ascertained about their origins or physical mechanisms. The field, however, is evolving at an accelerating rate. When I began my PhD less than three years ago, there were more FRB progenitor theories than actual FRB observations (52 theories versus 40 FRBs). And while only a hundred or so FRBs have been published, it has been reported that over a thousand FRB detections are patiently awaiting their public debut.

FRBs have garnered much enthusiasm, both in the scientific community and in the general public. Where there is a mystery, there is a story, and the tale of FRBs is one I am sure you will enjoy. In §2.3 you'll find a summary of all (peer-reviewed, published) FRB theories. This includes controversial theories for completeness. My team (understandably) vetoed me from adding details of a particular theory to our catalogue, but here I include it. Besides, sometimes great ideas are born in the area where science and science fiction blur. I will also include the tale of FRBs and microwave ovens: a romance that was not meant to be. But most importantly, I will critically examine all theories and give due attention to those with more clout. When we released our catalogue in 2018, we chose to take a largely agnostic stance. But things have changed and we know far more now than we did back then.

Chapter 1 provides an introduction to FRBs and relevant background in astronomy.

Chapter 2 reviews FRB properties and theories. §2.1.7 includes my contribution to Heintz et al. (2020) and §2.3 is based on the literature review by Platts et al. (2019), with major updates.

Chapter 3 demonstrates a novel way in which one can probe the baryonic density of the Milky Way halo using FRBs and non-parametric statistical models. The chapter is based on Platts et al. (2020), which was initiated as part of the 2019 Kavli Summer Program in Astrophysics (KSPA)[5] at the University of California, Santa Cruz (UCSC).

Chapter 4 presents an analysis of the time-frequency structure of FRB 121102 using autocorrelation functions and coherent power spectra to study the substructure of 11 bursts detected by the South African MeerKAT radio telescope in 2019. The chapter is based on Platts et al. (2021).

[5] https://kspa.soe.ucsc.edu/

CHAPTER 1

Fast Radio Bursts: Introduction and Background

Fast Radio Bursts (FRBs) recently emerged as one of the most mysterious events in astronomy and quickly proved themselves to be invaluable probes of the Universe around us. These extremely bright (50 mJy–100 Jy) and brief ($\mathcal{O}$(ms) or less) extragalactic pulses have already illuminated previously unseen baryons in the circumgalactic medium (CGM, see Chapter 3; Macquart et al., 2020)—solving a decades long physical problem—and hold the potential to set physical constraints in a variety of other contexts. Despite our ability to harness them as probes, little is known about FRBs themselves. They exist in the radio band, occupying a wide range of frequencies (120 MHz–8 GHz; Pastor-Marazuela et al., 2020), and very few have been observed with persistent radio or high-energy counterparts. Some FRBs give a series of bursts (known as repeaters), however most appear to be one-offs. To date, only one FRB has shown definite periodicity in its observed activity (Amiri et al., 2020), no FRBs have been found to have a rotational period and only thirteen have been localised to host galaxies (Chatterjee et al., 2017; Tendulkar et al., 2017; Bannister et al., 2019; Prochaska et al., 2019; Bhandari et al., 2020; Heintz et al., 2020). From these observations, FRBs do not seem to show a preference for host galaxy type. The pulses themselves have a broad range of features, and it is not yet clear whether FRBs form part of the same population or if they fall into different classes. FRBs are clearly a complicated phenomena, however within the last few years, huge strides have been made in uncovering their nature.

This chapter provides a brief history of FRBs (§1.1), followed by an overview of astronomical transients (§1.2), emission mechanisms (§1.3), and propagation effects (§1.4).

1.1 A (Very) Brief History

The first FRB was discovered fortuitously in 2007 by student David Narkevic and supervisor Duncan Lorimer (Lorimer et al., 2007). Found in archival pulsar data taken by the Parkes telescope in 2001 (Manchester et al., 2006), the Lorimer Burst—later called FRB 010724—was so bright that it saturated the telescope's single-bit digitiser. As well as its staggering brightness, the signal was extremely brief; on the order of milliseconds. What made this burst particularly exceptional, however, was its large dispersive delay. The group velocity of an electromagnetic (EM) wave depends on the density of free electrons (n_e) through which it passes. Higher frequency signals will arrive before lower frequency signals, resulting in a delay in arrival time, going as $\Delta t \sim \nu^{-2}$. This spread in frequency is quantified by a dispersion measure (DM), where the larger the column density of free electrons, the farther the implied distance.[1] So high was the DM of the Lorimer Burst, the implied distance was extragalactic. This in contrast to pulsars, whose brightness only allows observations within the Milky Way (MW) and Magellanic Clouds. For example, some of the brightest pulses from the Crab pulsar would only be observable out to ∼100 kpc using the Parkes telescope (Lorimer et al., 2007). It was evident that the Lorimer Burst represented an entirely new type of astronomical event.[2]

For four years, no other FRB was reported. During this time, the astronomical origin of the Lorimer Burst was formally brought to question. Burke-Spolaor et al. (2011) reported 16 bursts

[1] Note, however, that this also depends on the line of sight through the interstellar medium (ISM). Overdense regions will give a higher DM.

[2] Scepticism, however, was present in the community, and would remain for the next few years.

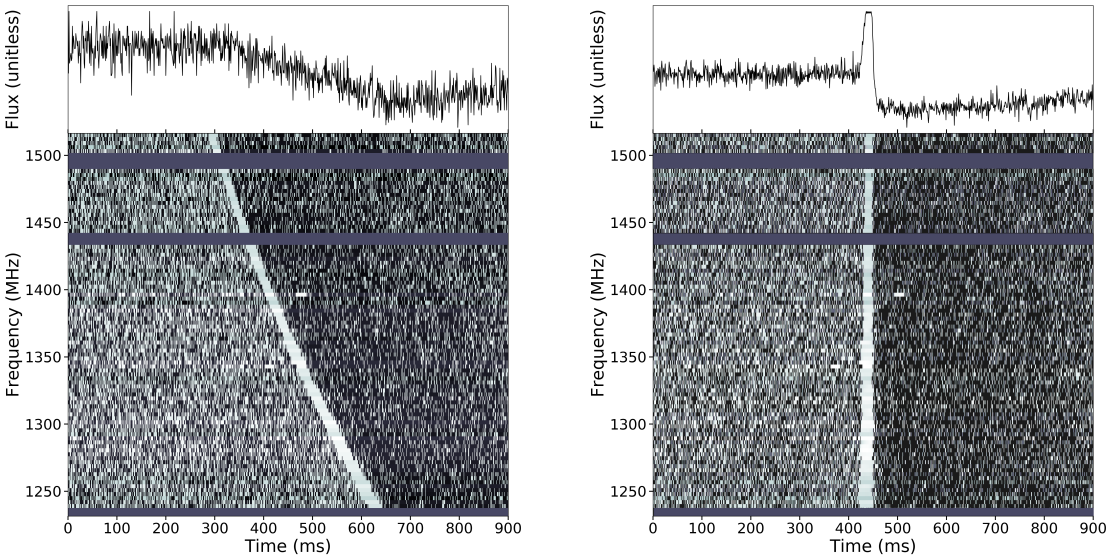

Figure 1.1: The Lorimer Burst. Data provided by the Parkes Radio Telescope (Keane & Petroff, 2015).[4] The left panel shows the pulse as it was observed with the characteristic frequency sweep $\Delta t \sim \nu^{-2}$. Higher frequencies arrive at the receiver first, followed by the lower frequencies. The right panel shows the burst de-dispersed to DM $= 375\,\mathrm{pc\,cm^{-3}}$.

from the Parkes telescope that appeared similar to the Lorimer Burst. These signals exhibited frequency sweeps akin to that of the FRB, but were clearly of a terrestrial nature: they appeared in many beams of the Parkes Multi-beam Receiver, and hence were not in the far-field. They were dubbed "Perytons"; a reference to the mythological winged elk that casts the shadow of a man. Over the next three years, another 9 Perytons were reported (Kocz et al., 2012; Bagchi et al., 2012; Saint-Hilaire et al., 2014). In 2015, an investigation was undertaken (Petroff et al., 2015b). Three Perytons were detected within one week in January, all of whom arrived during lunch hour. By comparing these observations to other FRB detections, Petroff et al. (2015b) conclusively demonstrated that the Lorimer Burst was not a Peryton. Moreover, the authors demonstrated that true Perytons were created by the microwave oven on site.

It was not until 2011 that another FRB was reported: FRB 010621 (Keane et al., 2011; also see Keane et al., 2012). Owing to its relatively low DM excess, however, it is not clear whether it is Galactic or extragalactic (Bannister & Madsen, 2014). As such, it was considered a tentative FRB detection. Concrete sources of extragalactic FRBs emerged in 2013, when Thornton et al. (2013) reported four high-DM pulses discovered at the Parkes telescope in the High Time Resolution Universe pulsar survey (HTRU; Keith et al., 2010). It was at this point that the name "Fast Radio Burst" emerged, along with the naming convention FRB YYMMDD corresponding to the date of the event. Soon, interest was piqued at observatories around world and dedicated FRB searches were initiated. Since then, about 120 FRBs have been reported in published work (Petroff et al., 2016).[3] These have a broad range of features: some repeat, while others are as of yet one-off events (e.g. Spitler et al., 2016); they display a broad range of polarisation properties (e.g. Caleb et al., 2018); some pulses have intricate structure, while others appear to be single peaked (e.g. Hessels et al., 2019); some have rotation measures (RMs) far higher than others (e.g. Michilli et al., 2018b; Gajjar et al., 2018); and they occupy a broad range of galaxy types (e.g. Heintz et al., 2020).

[3] See the FRB Catalogue (FRBCAT) at http://frbcat.org.
[4] Available at http://researchdata.ands.org.au/fast-radio-bursts-parkes/468266.

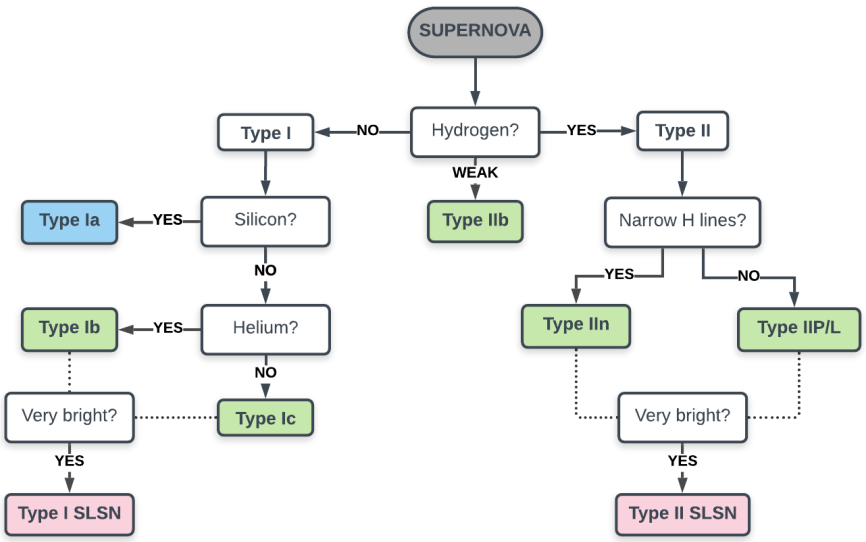

Figure 1.2: Supernova Classifications. The blue and green shaded boxes denote thermonuclear and core-collapse SN, respectively. The red boxes denote SLSNe.

1.2 A Quick Refresher on Transients

FRBs are a type of astronomical transient, which is broadly defined as any event that appears and fades on a human-observable timescale. Short duration transients—such as radio emission from pulsars (Hewish et al., 1968)—have timescales of seconds or less; and long duration transients—such as gamma-ray burst (GRB) afterglows (Chandra & Frail, 2012)—last hours to decades. While FRBs represent a new phenomenon, there is likely a link between their emission mechanisms and known transient populations (Bhandari et al., 2020; Li & Zhang, 2020; Heintz et al., 2020). Indeed, FRB 200428 has been associated with the Galactic magnetar SGR 1935+2154 (Bochenek et al., 2020b; Andersen et al., 2020) and coincident X-ray bursts (Li et al., 2020a; Mereghetti et al., 2020b,a). As such, we will briefly review other transients relevant to FRBs.

1.2.1 Supernovae

Supernovae mark the deaths of stars. They were first classified by Minkowski (1941) into two groups: Type I (hydrogen-poor) and Type II (hydrogen-rich). Subcategories continued to be added over the years, also based on spectroscopy (Figure 1.2). This resulted in dated nomenclature that is not based on the physics that drives the SN but that is still widely used today (for a detailed history, see da Silva, 1993). For clarity going forward, below is a summary of SN types, broadly grouped according to their physical trigger; either thermonuclear runaway or core-collapse.

1.2.1.1 *Thermonuclear Runaway*

Type Ia: Type Ia SNe are classified by a lack of hydrogen and a strong silicon absorption line near the maximum luminosity. They occur in binary systems in which at least one of the stars is a compact carbon-oxygen white dwarf (WD; Chandrasekhar, 1957). A slowly rotating WD has a critical mass of $1.44\,M_\odot$—the Chandrasekhar mass[5]—above which the core of the star reignites. When a WD accretes matter (or merges with another WD) to reach the Chandrasekhar mass, carbon fusion is initiated, which triggers a runaway nuclear reaction that engulfs the star. Owing to the fixed mass limit, the luminosities of Type Ia SNe are consistent. As such, they are used as "standard candles" to measure cosmological distances. For a review on Type Ia SN, see Parrent et al. (2014).

[5]Note that this is different to the Chandrasekhar limit, a point at which the electron degeneracy pressure can no longer support the gravitational weight of a star.

1.2.1.2 *Core-collapse Explosions*

Type Ib and Ic: These are formed by the core-collapse of massive stars that have lost their outer layers of hydrogen and (in the case of Type Ic) helium, either via strong stellar winds or mass transfer to a companion (e.g. Pols, 1997; Woosley & Eastman, 1997). As such, they are also known as stripped core-collapse supernovae (CC-SNe). They are distinguishable from Type Ia SNe by their lack of a silicon absorption line at a wavelength of 635.5 nm. Type Ic SNe are distinguishable from Type Ib SNe by their lack of a helium absorption line at 587.6 nm. Progenitor stars have masses of $\geq 40\,M_\odot$and have very high metallicities (Heger et al., 2003).

Type I SLSN: SLSNe are a rare subclass of hydrogen-poor CC-SNe that are $\sim$10−100 times brighter than regular SNe (MacFadyen et al., 2001; Kasen & Bildsten, 2010; Nicholl et al., 2017a).

Type II: The collapse of a star which has not lost its hydrogen shell results in a Type II SN.

Type IIb: Type IIb SNe have a weak hydrogen line their initial spectrum, which later fades as the ejecta expands. Progenitor stars have masses of $25-40\,M_\odot$with very high metallicities (Heger et al., 2003).

Type IIP/L: Type IIP/L SNe have relatively broad hydrogen lines (Doggett & Branch, 1985). Type IIP SNe progenitor stars have masses of $9-40\,M_\odot$with low or solar metallicities, and Type IIL SNe progenitor stars have masses of $25-40\,M_\odot$with very high metallicities (Heger et al., 2003).

Type IIn: Type IIn SNe have relatively narrow hydrogen lines (Filippenko, 1997).

Type II SLSN: Hydrogren-rich SLSNe typically have narrow hydrogen lines, however there is evidence of a population of SLSNe with broad lines (Inserra et al., 2018).

1.2.2 Gamma-ray Bursts

GRBs are short, intense flashes of soft ($\sim$MeV) γ-rays that last between tens of milliseconds and thousands of seconds. In the 1980s, an apparent bi-modality in GRB durations was recognised (Mazets et al., 1981; Norris et al., 1984) and by the 1990s, the existence of two distinct GRB populations became widely accepted (Kouveliotou et al., 1993). Below is a summary of these two classes: long-duration gamma-ray bursts (LGRBs) and short-duration gamma-ray bursts (sGRBs).

1.2.2.1 *LGRB:*

Long-duration gamma-ray bursts (or long gamma-ray bursts) last minutes or less, and are followed by X-ray emission that may be observable for hours to days (Costa et al., 1997), optical emission that may be observable for weeks (van Paradijs et al., 1997), and radio emission that may be observable for years (Frail et al., 1997). The optical afterglow allowed for sub-arcsecond localisations, revealing the LGRB host galaxies and redshifts (Kulkarni et al., 1998). Eventually, a physical picture of LGRBs emerged: a catastrophic event involving a stellar mass object. The expectation that LGRBs and CC-SNe should exist within similar galaxy types, however, was proven false (Fruchter et al., 2006; Yoon et al., 2006). Instead, LGRBs exist within the brightest regions of irregular, low-metallicity galaxies. This gave rise to the "collapsar" model, where LGRBs are born in Type I SLSNe.

1.2.2.2 *sGRB:*

Short-duration gamma-ray bursts (or short gamma-ray bursts) are $\lesssim 2\,s$ and are typically of higher energy (harder) than LGRBs (Kouveliotou et al., 1993). sGRBs also have afterglows in different wavelengths, but are generally much more faint than those of LGRBs (Paterson et al., 2020). sGRBs are thought to be from relativistic jets formed in binary neutron star (BNS) and neutron star (NS)–black hole (BH) mergers (Eichler et al., 1989; Narayan et al., 1992; Nakar, 2007). Evidence first emerged when a "kilonova" was observed with a coincident sGRB (Tanvir et al., 2013; Berger et al., 2013). Upon coalesence, a significant quantity of neutron-rich radioactive species are created, whose decay is observable as a kilonova (Li & Paczyński, 1998; Rosswog, 2005; Metzger

et al., 2010). The association between sGRBs and mergers/kilonovae was soon directly confirmed by observations of the gravitational wave (GW) 170817 events (Abbott et al., 2017b; Savchenko et al., 2017; Valenti et al., 2017; Cowperthwaite et al., 2017). Giant flares in Galactic (and nearby) magnetars also produce sGRBs (Thompson & Duncan, 1993). These magnetars—known as soft gamma-ray repeaters (SGRs)—emit γ- and short X-ray bursts in irregular intervals (Hurley et al., 2005; Frederiks et al., 2008). As mentioned previously, an FRB has been associated with a Galactic SGR and a short X-ray burst (Bochenek et al., 2020b; Andersen et al., 2020; Mereghetti et al., 2020b,a).

1.2.3 Neutron Stars

Neutron stars are born when a massive star ($\sim$8$-$25 $M_\odot$) collapses in a CC-SN. Once a main sequence star has exhausted its fuel, it may become a WD, where the core of the star is supported by the electron degeneracy pressure. Otherwise—if the mass of the core exceeds the Chandrasekhar limit (1.4 $M_\odot$)—it will collapse, forcing electrons and protons together to become neutrons. Simultaneous to this electron capture—where a proton absorbs an electron—is the release of electron neutrinos. When the core reaches nuclear density, the strong force and neutron degeneracy may stop further collapse (Bombaci, 1996). The neutrinos push the infalling outer envelope of the star outwards, to create a CC-SN. The angular momentum of the star is conserved, leaving behind a rapidly rotating neutron star. Typically, NSs have a mass of $\sim$1.2$-$2 $M_\odot$ and a radius of only 10–15 km (derived from theory; e.g. Abbott et al., 2017b).

There are three main types of NSs that emit detectable radiation, classed according to the source of energy: rotation-powered (or radio) pulsars, accretion-powered (or X-ray) pulsars, and magnetars. Radio pulsars are powered by their spin down, X-ray pulsars by the gravitational potential energy of matter accreted from a companion, and magnetars by the decay of their extremely strong magnetic fields.

1.2.3.1 *Radio Pulsars*

Radio pulsars are the archetype of radiating NSs (Pacini, 1967; Gold, 1968). Their discovery provided the first observational proof of NSs (Hewish et al., 1968), whose theoretical existence was predicted more than 30 years prior (Landau, 1932; Baade & Zwicky, 1934). Pulsars act as particle accelerators, emanating beams of radio emission from the open field lines of their magnetic poles. Since the magnetic field is misaligned with the NS rotation axis, each time the pulsar rotates, the beam sweeps across the sky to create a periodic series of radio pulses with durations of $\sim$0.1$-$1000 ms. The emission mechanism itself remains much of a mystery (Mitra, 2017).

The spin periods and surface magnetic field strengths of pulsars are distributed bimodally, leading to two reasonably distinct pulsar groups: "classical" and "millisecond" pulsars (Phinney & Kulkarni, 1994; Manchester et al., 2005). Classical pulsars are young ($\tau \sim 10^3$$-$$10^7$ yr) and strongly magnetised ($B \sim 10^{11}$$-$$10^{13}$ G) with relatively long periods ($P \sim 0.1$$-$10 s). They are often isolated and are associated with supernova remnants (SNRs), which dissipate after $\sim$$10^5$ years. Millisecond pulsars are old ($\tau \sim 10^8$$-$$10^{10}$ yr) and weakly magnetised ($B \sim 10^8$$-$$10^9$ G) with very short periods ($P \sim 1$$-$20 ms). Also known as recycled pulsars, these old NSs are spun up by accretion from a companion in a low-mass X-ray binary (Alpar et al., 1982; Taam & van den Heuvel, 1986; Bhattacharya, 1995). They often occur in globular clusters, where the occurrence of stellar interactions in which a NS can acquire a companion is significantly higher than in the Galactic field.

1.2.3.2 *X-ray binaries*

NSs that accrete matter from a binary companion are powerful X-ray sources (Guseinov & Zel'dovich, 1966). In-falling matter may be channeled along the magnetic field lines to the poles of the NS, where X-ray emitting hot spots form (though the exact mechanism is still under debate; Wang, 2016, for a review). X-ray binaries predominantly fall into one of two classes: low-mass X-ray binaries (LMXBs) or high-mass X-ray binaries (HMXBs; Bradt & McClintock, 1983). HMXBs are wind-fed with massive ($\geq$ 10 $M_\odot$) companions—typically early-type Be or OB supergiant stars (Liu et al., 2005, 2006). Since they are associated with young stars, HMXBs are largely confined to the Galactic plane. They have spin periods of 1$-$$10^3$ s and magnetic field strengths of $B \sim 10^{11}$$-$$10^{13}$ G.

LMXBs are fed by Roche-lobe overflow from late-type main-sequence stars, WDs, or F-G subgiant stars of low mass ($\leq 1\,M_\odot$; van Paradijs & McClintock, 1995; Liu et al., 2007). As such, they are largely concentrated in the Galactic bulge, with a relatively large distribution about the Galactic plane. They have millisecond periods and magnetic fields of $B \sim 10^8 - 10^9$ G (van der Klis, 2000).

1.2.3.3 *Magnetars*

The existence of NSs with super strong magnetic fields ($B \sim 10^{14} - 10^{15}$ G) was first evidenced by the extraordinarily bright giant flare of SGR 0526–66 (Mazets et al., 1979; Cline et al., 1980), which could not be attributed to a standard pulsar. Initially, the burst was attributed to classical GRBs, but consequent burst repetitions rendered this unlikely. Further, the bursts had softer spectra than classical GRBs, leading to the name "soft gamma-ray repeaters" (SGRs). The term "magnetar" was coined by Duncan & Thompson (1992), who later showed that spontaneous magnetic field decay could account for the bursts and persistent emission seen in SGRs (Thompson & Duncan, 1995, 1996). At the same time, an apparently new class of celestial X-ray sources (Gregory & Fahlman, 1980; Seward et al., 1986; Helfand, 1994; Israel et al., 1994) had been dubbed "anomalous X-ray pulsars" (AXPs; Mereghetti & Stella, 1995; van Paradijs et al., 1995). These appeared as isolated persistent X-ray pulsars whose luminosity exceeded the available energy budget from spin-down. Their emission, however, was noted by Thompson & Duncan (1996) to be similar to the persistent soft X-rays observed in SGRs (Rothschild et al., 1994; Vasisht et al., 1994; Murakami et al., 1994). The suspicion that AXPs are in fact magnetars was confirmed by the discovery of SGR-like bursts from two AXPs (Gavriil et al., 2002; Kaspi et al., 2003). Since then, bursting has become known as a characteristic property of AXPs, and the divide between SGRs and AXPs has faded to become essentially non-existent (for a full review, see Kaspi & Beloborodov, 2017).

There are at least two distinct types of X- and γ-ray bursts produced by the magnetar population within our Galaxy: short bursts and giant flares. SGRs emit short (5–500 ms), bright ($10^{39} - 10^{42}$ erg s^{-1}) bursts of soft γ-rays with two-blackbody fits (Israel et al., 2008) consistent with the trapping of plasma in the magnetosphere over a large region of the NS (e.g. Kumar et al., 2010; Collazzi et al., 2015). Giant flares are much more luminous ($10^{44} - 10^{47}$ erg s^{-1}) with a hard leading spectral spike, indicative of relativistic outflow and electron-positron (e^+e^-) pair fireball creation (Thompson & Duncan, 1995; Thompson & Duncan, 2001; van Putten et al., 2016). Short bursts also have lower spectral peaks (typically $\lesssim 100$ keV) and do not have strong pulsating afterglows (for a review, see Turolla et al., 2015).

1.3 Emission Mechanisms in Astronomy

In a bid to explain FRB origins, theorists have invoked numerous radiation mechanisms. Given their high implied brightness temperatures (§2.1.3) and intrinsic brevity (down to a few microseconds; e.g. Nimmo et al., 2021), there is general consensus that FRB emission is coherent (i.e. particles emit in phase with each other). In this chapter we will first review possible radiation mechanisms and their astrophysical context, and then describe the relevant processes to generate coherence.[6]

1.3.1 Radiation

1.3.1.1 *Bremsstrahlung*

German for "braking radiation," bremsstrahlung broadly describes any radiation that occurs as a process of particle deceleration. This extends to cylotron/synchrotron radiation (§1.3.1.3) and beta decay. When a charged particle is deflected by another particle—i.e. the path of the charged particle is bent—the law of conservation dictates that the loss in kinetic energy be transferred into radiation. When bremsstrahlung occurs in a plamsa it is commonly referred to as "free-free" radiation.[7] Here, the particle of interest is not part of an ion, an atom or a molecule both before and after its deflection.

[6] Also see Platts et al. (2019).

[7] Free-free absorption is the opposite effect, whereby a free electron absorbs energy or radiation when passing an ion.

Thermal bremsstrahlung is the dominant emission in clusters of galaxies. It has long been postulated that in order to bind the high speed galaxies of a cluster together, the space between them must be filled with some unseen gravitating material (Zwicky, 1937). It was not until the 1970s that this medium was evidenced when extended sources of X-ray emission were associated with rich clusters of galaxies (Gursky et al., 1971; Forman et al., 1972; Kellogg et al., 1972). Soon after, this emission was attributed to bremsstrahlung (e.g. Lea et al., 1973). Bremsstrahlung is also the dominant cause of radio emission in ionised atomic hydrogen (HII) regions, or emission nebulae, which are created when young, massive stars ionise the surrounding gas with high-energy UV radiation.

1.3.1.2 *Atomic and Molecular Transitions*

When an electron bound to an atom transitions from one energy level to another, there is a transfer of energy. This is a discrete process where quantised EM radiation is emitted or absorbed in the form of a photon, where the photon energy corresponds to the energy difference between the two states. Molecules also emit and absorb photons discretely when changing energy states. As well as through atomic transitions, molecular energy transfer occurs via rotational, vibrational, and vibronic transitions. Here, vibronic transitions are a combination of electronic and vibrational transitions. The former occurs when electrons in a molecule are excited to a higher energy level. Each transition has a specific energy difference and each is unique to the type of atom or molecule. Since the frequency of radiation is related to its energy via $E = h \cdot \nu$ (where h is Planck's constant), each atom or molecule has a distinct signature when changing states.

Atomic and molecular transitions form the basis of astronomical spectroscopy. A well-known example of atomic emission in astronomy is the HI 21 cm (1420 MHz) line. Its existence was predicted by van de Hulst in 1944, who showed that a hyperfine transition in the ground state of neural hydrogen (HI) would release a 5.87 μeV photon. Although this is a highly forbidden transition,[8] the sheer abundance of HI in the observable Universe and the collisions present in H gas led scientists to believe its detection was inevitable. Indeed, a few years later Ewen & Purcell (1951) observed the 21 cm line emanating from within the MW. A year later, astronomers started to use HI emission to map the MW.

1.3.1.3 *Synchrotron Radiation*

Also known as magnetobremsstrahlung, synchrotron emission occurs when an ultra-relativistic charged particle accelerates radial to the local magnetic field direction.[9] The curvature of the particles' trajectory dictates the energy and intensity of the resultant radiation, and the possible emission frequency ranges across the entire electromagnetic spectrum. Since the electric field vector is at an angle to the magnetic field, synchrotron radiation is polarised. As we will see later, this has important implications for FRB theories.

Although typically a radio band phenomenon, synchrotron radiation is ubiquitous in astronomy. The process is so efficient that with high enough magnetic fields it can produce γ-ray emission. In fact, sychrotron radiation has recently been revived as a candidate for GRBs—the most energetic EM sources in the Universe (e.g. Oganesyan et al., 2017; Ravasio et al., 2018, 2019; Burgess et al., 2020). It is the dominant form of radio emission in active galactic nuclei (AGN) and plays a key role in the radio and X-ray emission of pulsars and SNRs. Diffuse synchrotron emission in galaxy clusters has also confirmed the presence of relativistic electrons and magnetic fields in the intra-cluster medium (ICM).

1.3.1.4 *Curvature Radiation*

Curvature radiation is closely related to synchrotron radiation. Picture the helical path of a charged particle as it travels through a strong magnetic field. As the particle loses its rotational energy to synchrotron radiation, the curvature of the magnetic field line will begin to dominant over that of the helix. At this point, synchrotron radiation transitions to curvature radiation. Given the

[8] The excited ground state of HI lasts for ∼10 million years.

[9] Similarly, there is cyclotron and gyro-synchrotron radiation, which involve non-relativistic and moderately relativistic particles, respectively.

relatively low energies associated with it, curvature radiation is predominantly observed in the radio band.

Curvature radiation is a strong contender for radio pulsar emission, where relativistic particles stream out along the open field lines of the magnetosphere.

1.3.1.5 *Inverse Compton Scattering*

In contrast to Compton scattering, this is the process by which a low-energy photon is scattered to a higher energy by an ultra-relativistic electron. The energy transfer can be significant, resulting in X- or γ-ray photons. The newly created photons will have a new spectral energy distribution based on the initial spectrum, and dependent on the momentum distribution of the electrons and the optical depth of the electron-photon interaction.

Inverse Compton scattering has important consequences in astronomy. In AGNs, it is responsible for X-ray emission. As cool gas falls towards the supermassive black hole (SMBH) at the center of an AGN, it forms an accretion disk. As the gas dissipates inwards, its angular momentum is distributed outwards. The disk is heated, causing it to emit optical-UV photons. A hot corona forms above the cold accretion disk, whose relativistic electrons scatter the photons of the accretion disk to X-rays. The Sunyaev-Zel'dovich (SZ) effect is another example of inverse Compton scattering, where the cosmic microwave background (CMB) radiation is distorted when scattered by high-energy electrons in galaxy clusters.

Whilst on the topic of radiation mechanisms, it is worth noting that inverse Compton scattering is far more prevalent in synchrotron radiation than in curvature radiation. In the latter, the electron and photon momenta are closely aligned, whereas in the former they are not. As such, X- and γ-ray emission are expected counterparts to sychrotron radiation but not to curvature.

1.3.2 Generating Coherence

The high brightness and short timescales of FRBs necessitates coherence in their radiation. Here we detail the three main coherence mechanisms invoked in FRB progenitor theories: particle bunching, masers and Dicke's superradiance (DSR).

1.3.2.1 *Bunched Particles*

Coherence is reached when particles accelerating along magnetic field lines have the same oscillatory phase. This can be attained by grouping—or "bunching"—the particles. Three scenarios that induce bunching are described below.

i) Two-stream plasma instability: A two-stream plasma instability is the result of a beam of highly energetic positrons and electrons interacting with a dense plasma of less energetic positrons and electrons. Consider a plasma in steady-state and force-free magnetosphere with positrons and electrons streaming along curved field lines. As the net charge density of the plasma varies, so too will the velocity of the streams. Counter-streaming regions of oppositely charged plasma will excite unstable electrostatic plasma waves. The electrons and positrons become trapped in the electric field of the wave, forming bunches that are accelerated along the magnetic field lines.

ii) Magnetic braking: Magnetic braking is the process by which a differentially rotating stellar object loses angular momentum when ionised material is captured and expelled by the objects magnetic field. The particles are accelerated along the magnetic field lines in bunches.

iii) Magnetic reconnection: Disturbances in a magnetic field can cause a change in the field line topology, where the field lines violently snap and splice together. This process releases vast amounts of kinetic and thermal energy, and drives bunches of particles to accelerate.

1.3.2.2 *Masers*

We next consider the microwave amplification by stimulated emission of radiation, or maser. If an excited electron absorbs an incoming photon, it will emit two photons (of the same wavelength)

when it drops to its lowest energy state (stimulated emission). In the right conditions, this can trigger a chain reaction: the two emitted photons are absorbed by two excited electrons, who each emit two photons, and those four photons are absorbed by four excited electrons, and so on. To achieve this effect, one requires population inversion, where the amount of the electrons in an excited state outnumber those in the ground state. Here, the rate of stimulated emission exceeds absorption, and the radiation is amplified. This is best illustrated with an example: consider an EM wave travelling parallel to a magnetic field and an incoming beam of electrons that spiral around the magnetic field lines. If the frequency of the EM wave is near that of the incoming electron beam, the phase of the electrons around the field lines will become synced, causing phase bunching. The excited electrons thus all drop to the ground state simultaneously, triggering a chain of stimulated emission and forming a maser. Maser radiation is linearly polarised, which makes it an attractive emission mechanism for FRBs (e.g. Michilli et al., 2018b; Gajjar et al., 2018; Osłowski et al., 2019). The circular polarisation or lack of linear polarisation observed in some FRBs (e.g. Masui et al., 2015) would thus be attributed to propagation effects, such as Faraday rotation or Faraday conversion into circular polarisation (Michilli et al., 2018b; Vedantham & Ravi, 2019; Gruzinov & Levin, 2019). Both sychrotron and curvature masers have been considered in the context of FRBs, however only the former is viable (Ghisellini & Locatelli, 2018).

1.3.2.3 *Dicke's Superradiance*

Developed by R. H. Dicke in 1954, DSR occurs in the field of quantum optics, which considers the interactions between photons and matter at a submicroscopic level (Dicke, 1954; see Cong et al., 2016 for a recent review). When a group of entangled atoms or molecules drops to its ground state, the resultant emission is said to be superradiant. Consider a single atom that emits a photon via a transition. The timescale for the process is predefined. Should a large collection of atoms be entangled, however, the transition timescale is markedly reduced.[10] The atoms simultaneously emit photons at a higher energy, resulting in coherent radiation.

DSR has only recently been considered in astrophysics, where it has been shown that ISM hosts regions congruous to population inversion (Rajabi & Houde, 2016a,b). If triggered, DSR would generate strong radiation bursts that could propagate across cosmological distances with timescales that are sub-second (Houde et al., 2018a; Houde et al., 2018b) or several years (Rajabi & Houde, 2016b).

1.4 Propagation Effects

The medium through which an FRB travels influences the signal, and so the FRB that reaches the telescope receiver is not the FRB it once was. One's immediate reaction may be despair, but in actuality this affords us valuable research opportunities; albeit with rather large caveats. The observed properties of FRBs contain information about themselves, as well as all the intervening matter and the matter's properties. The difficult job, however, is teasing this information apart. An FRB pulse may be diffracted, refracted, reflected, or absorbed. Their polarisation state may be altered. And this may all happen multiple times along the pulse's journey. The typical path for an FRB is: through its local environment (e.g. a surrounding nebula), though the ISM and CGM of its host galaxy, though the intergalactic medium (IGM; and any intervening galaxies or structures), and finally through the CGM and ISM of the MW. The pulse may encounter magnetic fields, areas of turbulence, different matter densities and extreme temperature variations, all of which leave their mark on the FRB we observe.

1.4.1 Dispersion

FRBs follow a frequency-dependent arrival time. For propagation through a dense, magnetised plasma, the leading terms are (e.g. Tanenbaum et al., 1968; Tuntsov, 2014; Suresh & Cordes, 2019; Cordes & Chatterjee, 2019):

$$t(\nu) = 4.15\,\mathrm{ms}\left(\frac{\mathrm{DM}}{\nu^2}\right) + 28.6\,\mathrm{ps}\left(\frac{\mathrm{RM}}{\nu^3}\right) + 0.251\,\mathrm{ps}\left(\frac{\mathrm{EM}}{\nu^4}\right) \quad . \tag{1.4.1}$$

[10] See §2.3.7.2 for further details.

The dispersion measure $\mathrm{DM} = \int n_e \, \mathrm{ds}$ is the integral of the electron column density n_e to the source with standard units $\mathrm{pc\,cm^{-3}}$; the emission measure $\mathrm{EM} = \int n_e^2 \, \mathrm{ds}$ has standard units $\mathrm{pc\,cm^{-6}}$; and the Faraday rotation measure $\mathrm{RM} = \int n_e \mathrm{B}_{||} \, \mathrm{ds}$ includes the parallel magnetic field and has standard units $\mathrm{rad\,m^{-2}}$ (with $\pm$ corresponding to the two hands of circular polarisation—a positive RM has an average component pointing towards the observer, and a negative RM has an average component pointing away). Comparing the arrival times of FRBs to the dispersion law $t(\nu) \propto \nu^{-\beta}$, one obtains $\beta = 2$ within less than a percent (Thornton et al., 2013; Spitler et al., 2014; Scholz et al., 2016; Champion et al., 2016; Lawrence et al., 2017). The amount to which ν^3 and ν^4 contribute to the dispersion is thus heavily restricted, which implies FRBs are not associated with extremely dense plasma (Luan & Goldreich, 2014; Tuntsov, 2014; Dennison, 2014). This negated, for example, stellar origin theories for FRBs (Loeb et al., 2014, see §2.3.8.2), which require very large local plasma densities to account for the observed DMs. FRBs that show deviations from $\beta = 2$ may yet be observed, for example at low frequencies ($\nu \ll 1\,\mathrm{GHz}$) birefringent delays may occur if there is a sufficiently high RM (Cordes & Chatterjee, 2019).

The DM of an FRB can be divided into different components, for example:

$$\mathrm{DM_{FRB}} = \mathrm{DM_{ISM}} + \mathrm{DM_{IGM}} + \frac{\mathrm{DM_{host}}}{1+z} \quad . \tag{1.4.2}$$

The contribution from $\mathrm{DM_{ISM}}$ is $\mathcal{O}(10^0 - 10^3\,\mathrm{pc\,cm^{-3}})$; $\mathrm{DM_{IGM}}$ is $\mathcal{O}(10^2 - 10^3\,\mathrm{pc\,cm^{-3}})$; and $\mathrm{DM_{host}}$ is $\mathcal{O}(10^0 - 10^3\,\mathrm{pc\,cm^{-3}})$, which includes contributions from the host galaxy and local environment.[11] The denominator of the final term accounts for cosmological redshift corrections. The DM contribution from each term can tell us a significant amount about the FRB progenitor. $\mathrm{DM_{ISM}}$ is measured at the MW boundary, and can be modelled using MW electron density models, for example NE2001 (Cordes & Lazio, 2002) or YMW16 (Yao et al., 2017). The DM excess (i.e. $\Delta\mathrm{DM_{FRB}} = \mathrm{DM_{FRB}} - \mathrm{DM_{ISM}}$) can then infer whether a source is extragalactic, e.g. most pulsars sit within the MW and thus have negative DM excess values, whereas FRBs have positive values. To find the IGM contribution, one requires knowledge about the redshift of the source. Assuming all baryons are homogeneously distributed and ionised with ionisation fraction $x(z)$, the average $\mathrm{DM_{IGM}}$ is (e.g. Deng & Zhang, 2014; Yang & Zhang, 2016):

$$\langle \mathrm{DM_{IGM}} \rangle = \mathrm{K_{IGM}} \int_0^z \frac{(1+z)x(z)}{\left[\Omega_m (1+z)^3 + \Omega_\Lambda\right]^{1/2}} \, \mathrm{d}z \quad , \tag{1.4.3}$$

where $\mathrm{K_{IGM}} = 933\,\mathrm{pc\,cm^{-3}}$, and Ω_m and Ω_Λ are the energy densities of matter and dark energy, respectively. $\mathrm{DM_{host}}$ is then implied by $\mathrm{DM_{ISM}}$ and $\mathrm{DM_{IGM}}$. This has significant implications for the host galaxy and the FRB's local environment (e.g. Tendulkar et al., 2017; Bassa et al., 2017).

Dispersion smearing may occur when data is not coherently de-dispersed. A pulsar or FRB signal observed in a finite incoherent channel experiences a dispersion measure smear of

$$\tau_{\mathrm{DM}} = 8.3 \, \frac{B\,DM}{\nu^3} \, \mu\mathrm{s} \quad , \tag{1.4.4}$$

where B is the bandwidth of a channel in MHz and ν is the observing frequency. This can have significant frequency-dependent effects on the time-resolution of data (e.g. see §4.3). There exist various phase-coherent dispersion removal algorithms that attempt to reduce this effect, for example Digital Signal Processing Software for Pulsar Astronomy (DSPSR; van Straten & Bailes, 2011).

1.4.2 Scattering

FRBs may become temporally broadened when scattered by intervening medium (e.g. Thornton et al., 2013). The resultant pulse is a convolution of its original form and a one-sided exponential decay with decay time $\tau \propto \nu^{-4}$. The dominant cause of scatter in FRBs is thought to be from the local environment of the FRB, the host galaxy ISM, or the ISM of intervening galaxies (Simard & Ravi, 2020). Currently, scattering is observed in roughly 30% of FRBs in the `FRB Catalogue`.

[11] The dispersive effects of Earth's ionosphere and interplanetary medium of the Solar System are $\mathcal{O}(10^{-5}\,\mathrm{pc\,cm^{-3}})$ and $\mathcal{O}(10^{-3}\,\mathrm{pc\,cm^{-3}})$, respectively, and are thus often neglected.

1.4.3 Scintillation

As an FRB travels through clumpy, turbulent medium, refractive and diffractive effects may cause the pulse intensity to scintillate. Here, constructive or destructive interference occurs when the signal comes together after different wavelengths have experienced different delays (e.g. Rickett, 1990; Narayan, 1992). Scintillation may be evident in various FRBs, for example: FRB 150807 has apparent scintillation that may be attributed to the IGM or host galaxy (Ravi et al., 2016); FRB 121102 has fine-scale structure consistent with scintillation in the ISM (Gajjar et al., 2018); and the variation in spectral structure between the two pulses of the Galactic FRB 200428 may be accounted for by interstellar scintillation (Simard & Ravi, 2020).

1.4.4 Faraday Rotation and Polarisation

The polarisation of a transverse wave specifies the orientation of its perpendicular oscillations. By convention, the polarization of an EM wave refers to the direction of the electric field. In a linearly polarised wave, the electric and magnetic fields oscillate in a single direction. In a circularly polarised wave, the fields rotate about the plane along which the wave travels, and may be left- or right-handed depending on the direction of rotation. This rotation—Faraday rotation or the Faraday effect—may occur when light travels through a magneto-ionic medium, for example when an FRB travels through ISM. The strength of this rotation is described by the rotation measure (RM)—defined in §1.4.1—and the amount to which a wave is polarised is described as a percentage. FRB polarisation and rotation measures are currently only available for 20 out of the 120 published bursts in the `FRBCAT`. All have significant linear polarisation (8.5−100%), 14 have linear polarisation higher than 70%, and 15 have some level of circular polarisation.

1.4.5 Plasma Lensing

Plasma can act as a powerful lens that refracts the light that propagates through it, causing a wide variety of observable signatures. For example, lensing is a well-known cause of multiple imaging in the Crab pulsar, where dense filamentary columns cause highly chromatic pulse echoes (e.g. Backer et al., 2000; Graham Smith et al., 2011). Lensing can also amplify signals, as demonstrated by the Black Widow Pulsar, whose observed flux is sometimes briefly enhanced by a factor of 70−80 at certain frequencies (Main et al., 2018). In this case, lensing is owed to clumps in the intra-binary material of the pulsar system. Cordes et al. (2017) consider the effects of plasma lensing on FRBs, and show it may consistently account for some of the spectral and luminosity variations observed in some repeating FRBs (also see Main et al., 2018; Hessels et al., 2019). Further discussion on plasma lensing can be found in Chapter 4.

CHAPTER 2

Fast Radio Bursts: Details and Specifics

In this chapter, we review FRB properties and possible origins. §2.1 details FRB characteristics, such as event rates, counterparts and host galaxy populations. A summary of key FRB detections is provided in §2.2. The chapter closes with an overview of FRB progenitor theories (§2.3).

2.1 FRB Characteristics

2.1.1 Event Rates and Sky Distribution

Although there are are currently only ∼120 published FRB sources, the estimated all-sky event rate of FRBs is very high: for a fluence threshold of $\mathcal{F} \gtrsim 1\,\mathrm{Jy\,ms}$, there are an estimated $\sim 10^3 - 10^4$ FRBs detectable over the whole sky per day (Thornton et al., 2013; Spitler et al., 2014; Champion et al., 2016; Keane & Petroff, 2015; Rane et al., 2016; Crawford et al., 2016; Oppermann et al., 2016; Lawrence et al., 2017; Bhandari et al., 2018). Assuming a cosmological distribution out to redshift $z \sim 1$, this corresponds to a volumetric rate of $\sim 2 \times 10^3\,\mathrm{Gpc^{-3}\,yr^{-1}}$ (Petroff et al., 2019). This measure has important implications for FRB progenitor theories, for instance: the volumetric rate of magnetar births is consistent with the high FRB event rate (if magnetars emit repeat bursts, e.g. Nicholl et al., 2017b), but rates of cataclysmic events fall far short (Ravi, 2019).

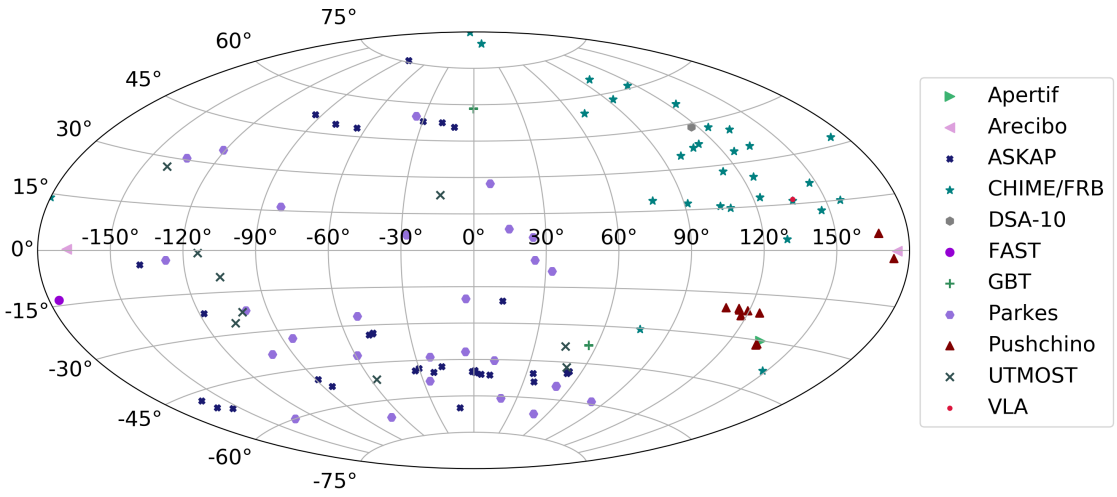

Figure 2.1: An Aitoff projection of the FRB sky distribution showing the locations of all published (verified) FRBs to date. Inspired by Figure 14 in Petroff et al. (2019). Data available at `http://frbcat.org`.

Initial analyses suggested that FRBs have a latitude dependence, evidenced by a deficit of mid-latitude ($|b| < 15°$) detections, possibly due to interstellar scintillation (Petroff et al., 2014; Macquart & Johnston, 2015), which enhances high-latitude observations. If this is the case, propagation effects through the ISM play an important role in the detectability of FRBs and hence in population estimations. Evidence for latitude dependence, however, is debatable (Connor et al., 2016b;

Rane et al., 2016). Some studies support dependence (Lawrence et al., 2017; Macquart & Ekers, 2018), while others argue against it (Bhandari et al., 2018). These estimates are limited by sample size, where fewer than 20 FRBs were available at the time. Estimates are also limited by knowledge of FRB positions within the telescope beam. Take, for example, the low latitude ($|b| < 1°$) FRB 141113 (Patel et al., 2018). If the event occurred in the main lobe of the telescope, the implied FRB event rate would be ∼5 times higher than if it was detected in the side lobe (Patel et al., 2018). As the FRB population has increased, however, the statistical significance of any latitude-dependence appears to have decreased (Petroff et al., 2019). In either case, the answer will be revealed in the near future.

2.1.2 Pulse Width and Structure

The pulse morphology of FRBs has been found to be remarkably varied (e.g. Hessels et al., 2019). Early FRB detections showed simple, Gaussian-like pulses, sometimes with scattering broadening (Lorimer et al., 2007; Thornton et al., 2013; Spitler et al., 2014). The first FRB to show temporal structure was reported by Champion et al. (2016), who presented a two-component FRB. This challenged FRB theories that invoked a single high energy event, such as NS collapse (§2.3.7.1). Since then, a wealth of structure has been reported (e.g. downward drifting sub-pulses, multiple peaks and changes in the time-frequency relationship; Gajjar et al., 2018; Michilli et al., 2018b; Hessels et al., 2019; Caleb et al., 2020; Platts et al., 2021). Today, the apparent lack of structure observed in some bursts is thought to be due to limited time-resolution. A comprehensive discussion on pulse structure is presented in Chapter 4.

The pulse widths of FRBs also show large variation, ranging from as short as a few µs (e.g. Michilli et al., 2018b; Farah et al., 2018; Cho et al., 2020; Nimmo et al., 2021) to several tens of ms (e.g. Cruces et al., 2021). Both have important implications for progenitor models. The minimum burst duration informs the physical scale of the event. For example, a pulse of ∼30 µs for FRB 121102 and ∼15 µs for FRB 181112 implies an emission region of several kilometers[1] (Farah et al., 2018; Cho et al., 2020, respectively). The maximum burst duration, on the other hand, holds information about propagation effects, as well as about the bursting region (e.g. Simard & Ravi, 2020).

As discussed in §2.1.8, pulse width and structure may also serve as a diagnostic if there exist independent repeating and one-off FRB populations.

2.1.3 Brightness Temperature

The radiation brightness temperature T_b inferred from the source is a useful quantity when studying non-thermal emission, and can be used to distinguish between coherent and incoherent emission. It is defined to be the thermodynamic temperature of a black body of equivalent luminosity in the Rayleigh-Jeans limit ($h\nu \ll kT$) of the Planck spectrum. The brightness temperature of an FRB is given by (e.g. Popov et al., 2018):

$$T_b \simeq 10^{35.8}\,[\mathrm{K}] \left(\frac{S_\nu}{\mathrm{Jy}}\right) \left(\frac{\nu}{\mathrm{GHz}}\right)^{-2} \left(\frac{W}{\mathrm{ms}}\right)^{-2} \left(\frac{d_L}{\mathrm{Gpc}}\right)^{2} , \tag{2.1.1}$$

where S_ν is the peak flux density, W is the pulse width and d_L is the luminosity distance. From this, a one millisecond FRB of 1 Jy can be found to have a brightness temperature of $T_b = 3.4 \times 10^{35}$ K. This implies strong coherence: sources with $T_b > 10^{12}$ K should be coherent, as above this value the emission temperature from individual electrons is limited by Compton losses (Kellermann & Pauliny-Toth, 1969).

2.1.4 Energetics

FRBs are enormously powerful. In the case of isotropic emission, the burst energy of an FRB is given by (e.g. Popov et al., 2018):

$$E_\mathrm{b} \simeq 10^{39}\,[\mathrm{erg}] \left(\frac{S_\nu}{\mathrm{Jy}}\right) \left(\frac{\nu}{\mathrm{GHz}}\right) \left(\frac{W}{\mathrm{ms}}\right) \left(\frac{d_L}{\mathrm{Gpc}}\right)^{2} . \tag{2.1.2}$$

[1] Note, however, special relativistic effects can substantially change this inferred size.

Beaming over a solid angle Ω_b introduces to this a factor of $(\Omega_b/4\pi)$. For small beaming angles, the energy requirements can thus be greatly relaxed. As such, many FRB progenitor theories assume some beaming mechanism (e.g. masers).

2.1.5 Localisation

To reliably establish the redshift of an extragalactic FRB signal, one requires an association to a host galaxy. To date, this has been achieved for only 13 FRBs. This is primarily due to telescope limitations: for the first decade of FRB searches, telescope localisation regions were much greater than a square arcminute ($'$) versus the $\sim 1''$ (arcsecond) scale required for $\sim$Gpc distances (Vedantham et al., 2016; Eftekhari & Berger, 2017). This is relaxed to $\sim 10''$ if the FRB is accompanied by a persistent radio source (as is the case for FRB 121102; Eftekhari et al., 2018). For repeating FRBs or those with afterglow/persistent counterparts, follow-up observations can accurately establish an emission region. Multiwavelength follow-ups, however, have been largely unsuccessful (§2.1.6). The association of an FRB with a host galaxy has thus been primarily achieved with statistical comparisons of the FRB position to coincident or nearby galaxies (as is done for GRBs, e.g. Bloom et al., 2002; Blanchard et al., 2016).

2.1.6 Counterparts

Multiwavelength follow-ups of FRBs have yet to reveal afterglows analogous to those of GRBs (Petroff et al., 2017; Bhandari et al., 2018; Chen et al., 2020) or associated SN-like counterparts (Marnoch et al., 2020). Indeed, the isotropic GRB emission is 10 orders of magnitude higher than FRBs, and thus FRB afterglow is expected to be significantly fainter (e.g. Yi et al., 2014) and more difficult to detect. Another challenge is making concrete associations: for signals out to $z \sim 1$, localisation regions are required to be $20''$ or less (Eftekhari & Berger, 2017; Eftekhari et al., 2018).

To date, very few counterparts have been detected. DeLaunay et al. (2016) claimed a γ-ray transient associated with FRB 131104, but the detection is considered to be tenuous (Shannon & Ravi, 2017), follow-up searches have yielded null results (Xi et al., 2017), and a re-analysis of the data found no evidence of a γ-ray counterpart (Sakamoto et al., 2020). A possible sGRB-like afterglow was reported for FRB 150418 (Keane et al., 2016), but this was later found to be associated with an AGN (Williams & Berger, 2016). The only conclusive counterparts are considered to be for FRB 121102 (§2.2.3) and the Galactic FRB 200428 (§2.2.5). The former is associated with persistent radio emission (Chatterjee et al., 2017; Marcote et al., 2017) and the latter with coincident prompt X-ray emission (Mereghetti et al., 2020b; Ridnaia et al., 2020; Zhang et al., 2020b).

2.1.7 Host Galaxy Types

Astronomical transients are likely related to specific stellar populations and galactic environments. For example: CC-SNe and sGRBs are predominantly found in luminous, massive galaxies (Prieto et al., 2008; Berger, 2008; Kelly & Kirshner, 2012; Taggart & Perley, 2019), whereas LGRBs and SLSNe are typically found in faint, low metallicity, lower-mass star-forming galaxies (Savaglio et al., 2009; Vergani et al., 2015; Perley et al., 2016; Gal-Yam, 2019). As such, characterising galaxy properties may inform of the most likely FRB progenitor channel (e.g. Bhandari et al., 2020; Li & Zhang, 2020; Heintz et al., 2020; Bochenek et al., 2020a). One should note, however, that the current sample size of FRB host galaxies is very limited, and thus conclusions and correlations detailed in the following are tenuous.

The first FRB localisation was to a star-forming, low-metallicity dwarf galaxy (Chatterjee et al., 2017; Tendulkar et al., 2017; Marcote et al., 2017). The host is similar to those of LGRBs and SLSNe, which motivated the development of models related to young, hyperactive magnetars (§2.3.1, e.g. Popov & Postnov, 2013; Kulkarni et al., 2014; Lyubarsky, 2014; Murase et al., 2016; Beloborodov, 2017). Since then, an additional 12 FRBs have been localised. It appears that—much like the burst itself—the host galaxy of FRB 121102 is rather anomalous. FRB hosts tend to be massive galaxies with older stellar populations, whose properties are akin to the typical hosts of sGRB, CC-SN and Type Ia SN (Li & Zhang, 2020). Most bursts have large spatial offsets from galaxy centers and occur in regions with low surface brightness (Bochenek et al., 2020a; Safarzadeh

et al., 2020). The host galaxies do not conform to a specific galaxy type; spanning a broad range of colours, stellar masses and star-formation rates (SFRs; Heintz et al., 2020).

In Heintz et al. (2020), my role was to perform 2D Kolmogorov–Smirnov (KS) tests to compare FRB host populations to different galaxy populations. The FRB population was compared to galaxy populations classed according to the colour-magnitude diagram, the BPT diagram and the star-formation rate versus stellar mass (SFR–$M_\star$) diagram. All galaxy data was taken from the PRIMUS survey (Moustakas et al., 2013).

Recall: A KS test quantifies the distance between the empirical distribution functions of two samples. Here, the empirical distribution is the cumulative distribution function of a particular realisation of a sequence of random variables. For two empirical distributions $F_{1,n} = P(X_1 > x_n)$ and $F_{2,m} = P(X_2 > x_m)$, the KS statistic is:

$$D_{n,m} = \sup_x |F_{1,n}(x) - F_{2,m}(x)| \quad , \tag{2.1.3}$$

where sup is the supremum function. The supremum of a subset S of a partially ordered set T is defined to be the least element in T that is greater than or equal to all elements of S, if such an element exists. The null hypothesis that samples are drawn from the same underlying distribution is rejected at a level α for

$$D_{n,m} > \sqrt{-\ln\left(\frac{\alpha}{2}\right) \cdot \frac{1 + \frac{m}{n}}{2m}} \quad . \tag{2.1.4}$$

The p-value—the probability that an observed difference occurred by random chance ($P_{\rm KS}$)—is given by the proportion of samples in the distribution that exceed the observed value $D_{n,m}$.

The colour-magnitude diagram serves as an indicator of the stellar population of a galaxy (Figure 2.2). It compares the absolute r-band magnitudes M_r to the rest frame $(M_u - M_r)$ colour (surface temperature), revealing three distinct regions: the red sequence, the green valley, and the blue cloud. The red sequence is associated with early-type galaxies and the blue cloud with late-type galaxies (Strateva et al., 2001). The green valley is thought the be a transition zone between star-forming (blue cloud) galaxies and quiescent (red sequence) galaxies (Martin et al., 2007). For the FRB host galaxy populations, we consider one-off, repeaters, and the full population (with sample sizes of 3, 8 and 12, respectively). The repeating FRB population was found to be consistent with having the same underlying distribution as those drawn from the late-type population or the full population with $P_{\rm KS} = 0.192$ and $P_{\rm KS} = 0.178$, respectively. The null hypothesis for all other possibilities was rejected with $P_{\rm KS} \leq 0.007$. 2D KS tests on the SFR–$M_\star$distribution yielded similar results. Here, galaxy populations are classed as either star-forming or quiescent (Figure 2.2). FRB populations are found to avoid the main sequence of star-forming galaxies ($P_{\rm KS} < 0.001$).

A BPT diagram classifies galaxies as star-forming, AGN or low-ionization nuclear emission-line region (LINER) based on their [OIII]/Hβ and [NII]/Hα nebular emission-line ratios (Baldwin et al., 1981). In Heintz et al. (2020), data was available for 6 one-off FRBs and 1 repeating FRB. We performed 2D KS tests using the full population of FRBs and the one-off population. Again, we found that both FRB host populations are inconsistent with the distribution of star-forming galaxies ($P_{\rm KS} = 0.015$ and $P_{\rm KS} = 0.004$, respectively). The only statistically significant result was between one-off FRBs and the combined AGN and LINER population ($P_{\rm KS} = 0.122$). In the BPT diagram, however, we expect quite significant overlap in populations near the classification boundaries, shown in the Figure 2.3 by the solid, dashed and dotted lines. As such, we decided to employ additional analysis to verify our results. Using kernel density estimation (KDE), we modelled probability density functions (PDFs) of the star-forming, AGN and LINER populations based on their classification in the BPT diagram. KDE approximates the underlying distribution of a sample by fitting a kernel (density function) at each data point and summing the contribution. The smoothness of the PDF is determined by the bandwidth or widths of the kernels at each point. An in depth description of KDE is given in §3.3.2. By varying the bandwidth of the KDE, one can smooth the boundary between galaxy classifications. This is shown in Figure 2.3, where the contour lines show the simulated galaxy populations modelled with KDE. We applied the 2D KS

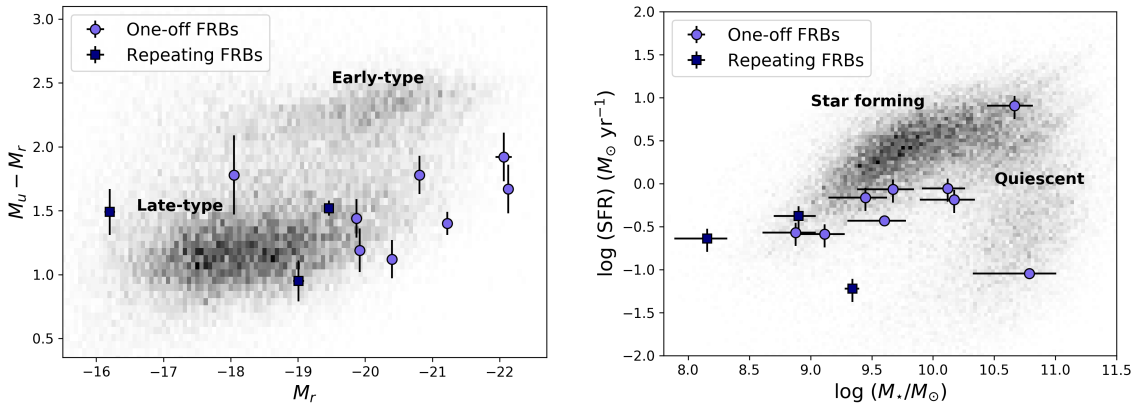

Figure 2.2: Colour-magnitude diagram and SFR–$M_\star$ diagram, based on Figures 5 and 7 of Heintz et al. (2020) generated with code by K. E. Heinz. Galaxy data provided by the PRIMUS survey (Moustakas et al., 2013). FRB populations (one-offs, repeaters and the full set) appear to avoid the main loci in both diagrams, i.e. they do not seem to track star-formation regions.

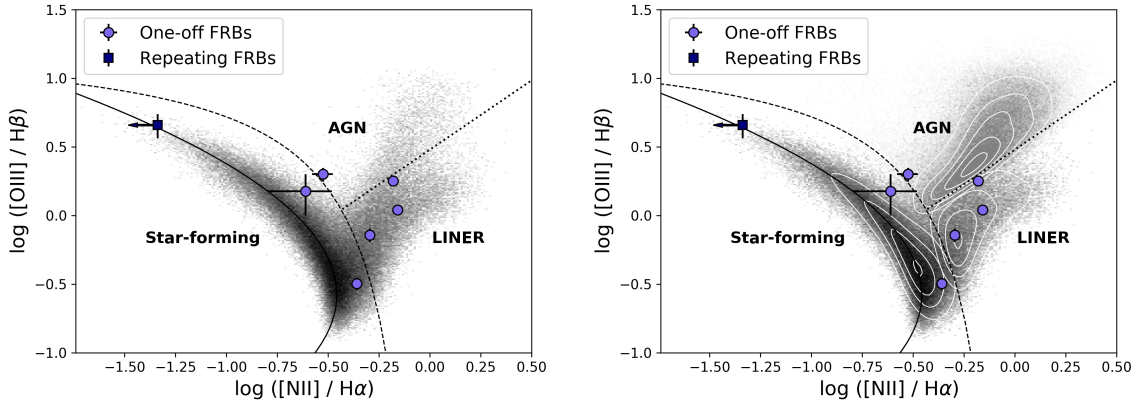

Figure 2.3: BPT diagram without and with KDE contours, based on Figure 6 of Heintz et al. (2020) generated with code primarily by K. E. Heinz. Galaxy data provided by the PRIMUS survey (Moustakas et al., 2013). The contours in the second figure show the PDF of galaxy classes modelled with KDE. Here, the galaxy classes do not strictly conform to the classification lines (solid, dashed and dotted).

tests to simulated galaxy samples, and found that the difference in results was negligible. As such, we concluded the hard BPT classification was sufficient to analyse the underlying distributions.

2.1.8 Repeaters versus One-offs

Observationally, FRBs present as either repeating or one-off. Out of the ∼120 FRBs published, 20 have been observed to repeat.[2] This leads to the possibility of two distinct FRB populations (e.g. Palaniswamy et al., 2018; Caleb et al., 2019; Lu et al., 2020b; Ai et al., 2020). Given an apparently one-off FRB, it is difficult to know whether the source is truly an isolated event: the wait time between bursts may be very high (Palaniswamy et al., 2018; Caleb et al., 2019) or the luminosity may have dropped below detection limits (Palaniswamy et al., 2018; Luo et al., 2018, 2020; Lu & Piro, 2019). While all FRBs might be capable of repeating, numerous follow-up searches have yielded no signs of repetition in some (e.g. Bhandari et al., 2018; Shannon et al., 2018).

The bursts from repeaters and apparently one-off FRBs seem to differ. For example, repeating bursts tend to have larger burst envelopes (Spitler et al., 2016; Fonseca et al., 2020), with pulse

[2]This does not imply that ∼17% of observed FRBs are repeaters—there is a publication bias. In the near future, Canadian Hydrogen Intensity Mapping Experiment (CHIME/FRB) will publish hundreds more FRBs (repeating and non-repeating), which will provide a more representative observed repeater fraction.

widths up to 74 ms in the 120–800 MHz bandwidth[3] (Amiri et al., 2019; Andersen et al., 2019; Fonseca et al., 2020) and up to a few tens of ms in the 1.2–8 GHz bandwidth (Hessels et al., 2019; Kumar et al., 2019; Marcote et al., 2020). There is also an enormous dynamic range of timescales in the bursts of some repeaters, for example FRB 180916.J0158+6 (Nimmo et al., 2021). Another characteristic is the downward drift in sub-bursts observed for some FRBs (e.g. Hessels et al., 2019; Amiri et al., 2019; Andersen et al., 2019; Fonseca et al., 2020). While these differences cannot confirm nor rule out whether there are two FRB populations (i.e. the emission may be influenced by the age, local environment or activity levels of the source), they may help inform whether a source is likely to repeat (e.g. Day et al., 2020) and hence where to focus follow-up efforts.

2.2 Notable FRBs

To better understand FRBs, it is important to be aware of key FRB sources and their characteristics. The following offers a brief summary of the most famous FRBs, demonstrating the diversity of these transients and providing important background for when we consider FRB progenitor models in §2.3.

2.2.1 FRB 010724: The Lorimer Burst

The Lorimer Burst (Lorimer et al., 2007)—the first discovered FRB—remains one of the brightest FRBs to date, with a fluence of 800 ± 400 Jy ms (revised analysis; Ravi, 2019). It is arguably an outlier in the FRB population, discovered through observation bias. As such, it has been proposed that the Lorimer Burst be excluded from statistical analyses of the FRB population (Macquart & Ekers, 2018).

2.2.2 FRB 010621: The Keane Burst

The Keane burst (Keane et al., 2011, 2012) was the second FRB discovered, and remains a fringe case between a Galactic and extragalatic FRB source. It has a measured DM of $745 \pm 10\,\mathrm{pc\,cm^{-3}}$, with a MW contribution of $\mathrm{DM_{ISM}} = 523\,\mathrm{pc\,cm^{-3}}$ or $\mathrm{DM_{ISM}} = 320\,\mathrm{pc\,cm^{-3}}$ based on the NE2001 model (Cordes & Lazio, 2002) or YMW16 (Yao et al., 2017) model, respectively.[4] The small fractional DM excess prompted Bannister & Madsen (2014) to study the Hα and Hβ emission to find a more accurate electron density estimate. They concluded with 90% confidence that the Keane burst is Galactic, but unless a repeat burst occurs—allowing for its exact localisation—its origin will remain uncertain.

2.2.3 FRB 121102: The First Repeater

FRB 121102 was first presented by Spitler et al. (2014), who later reported an additional 10 bursts from the same source (Spitler et al., 2016). This was a landmark discovery: repetitions proved that at least some FRBs cannot be the result of a cataclysmic event. Further, the repetitions facilitated targeted multi-wavelength campaigns, revealing coincidence with both persistent radio and optical emission (Chatterjee et al., 2017; Marcote et al., 2017). Using spectroscopic data from the optical source, Tendulkar et al. (2017) calculated a redshift of $z = 0.19273(8)$, thus localising FRB 121102 to a low-metallicity, low-mass dwarf galaxy. High-resolution optical imaging by Bassa et al. (2017) then pin-pointed FRB 121102 to a star-forming region in the host galaxy. Tendulkar et al. (2017) noted that low-metallicity dwarf galaxies are known to host SLSNe and LGRBs, prompting the development of related FRB theories (§2.3.1; e.g. Metzger et al., 2017). While the host galaxy of FRB 121102 was initially assumed to be representative of FRB hosts, subsequent FRB localisations suggest that FRB 121102 is atypical and that FRBs occupy a broad range of galaxy types (§2.1.7).

The extreme and dynamic magneto-ionic environment of FRB 121102 was evidenced by the first polarisation measurements: emission was found to be nearly 100% linearly polarised with a RM (in the source frame) of $1.46 \times 10^5\,\mathrm{rad\,cm^{-3}}$ that decreased to $1.33 \times 10^5\,\mathrm{rad\,cm^{-3}}$ over a 7 month

[3] While Pleunis et al. (2020) report burst widths of 40−160 ms at 150 MHz, the authors state that the larger burst widths are likely due to scattering.

[4] See Chapter 3 for details on the Galactic electron density estimation models NE2001 and YMW16.

period (Michilli et al., 2018b). RMs this high had only been observed before near the SMBH at the center of the MW, Sgr A* (e.g. Bower et al., 2003; Marrone et al., 2007). Such a large change in RM over this time frame without a comparable change in DM requires extreme variation in the line-of-sight projected magnetic field. Michilli et al. (2018b) note that such large magneto-ionic variation has otherwise only been observed in the Galactic center magnetar J1745–2900 (Desvignes et al., 2018). For a detailed discussion on the RM of FRB 121102, see Hilmarsson et al. (2021).

The source of persistent radio emission is currently unknown, but may be from a weak AGN (e.g. Marcote et al., 2017, discussed in §2.3.6) or from a magnetised electron-ion nebula (e.g. Metzger et al., 2017, discussed in §2.3.1). To date, no prompt optical, X-ray or γ-ray flashes have been associated with FRB 121102 (Scholz et al., 2016; Scholz et al., 2017; Hardy et al., 2017; Acciari et al., 2018). FRB 121102 has, however, been observed over a broad range of radio frequencies; as high as 8 GHz (e.g. Law et al., 2017; Gajjar et al., 2018; Spitler et al., 2018) and as low as 600 MHz (e.g. Josephy et al., 2019; Caleb et al., 2020). This has revealed a wide variety of time-frequency structure (Hessels et al., 2019), including sub-pulse drifting and an apparent broadening at lower frequencies. A detailed discussion on the structure of FRB 121102 pulses can be found in Chapter 4. About 20% of the bursts are narrow band, with emission peak frequencies that can change rapidly in time (e.g. Gourdji et al., 2019; Majid et al., 2020).

FRB 121102 goes through activity phases. For example, the Very Large Array (VLA) telescope reported no bursts between April–May 2016 and 9 bursts between August–September (Chatterjee et al., 2017). In fact, during an active period, the bursts of FRB 121102 are positively prolific: Zhang et al. (2018b), for example, report 45 pulses within a 30 minute period. Despite the large sample of FRB 121102 pulses, no definitive periodicity has been reported, although Rajwade et al. (2020b) tentatively derive an activity period of ∼157 days (also see Cruces et al., 2021).

2.2.4 FRB 180916.J0158+65: The First Periodically Active FRB

In early 2020, periodicity in the activity period of an FRB was reported for the first time (Amiri et al., 2020). FRB 180916.J0158+65—initially presented in Andersen et al. (2019)—resides in the outskirts of a massive spiral galaxy (Marcote et al., 2020). Nearly all pulses exhibit downward drifting substructure and there is no apparent trend in the temporal width or bandwidth of pulses. Bursts are emitted sporadically and in clusters, with a period of 16.35 ± 0.15 days and a phase window of 5 days (Amiri et al., 2020). Further, the periodic activity has been shown to be frequency-dependent (Pleunis et al., 2020; Pastor-Marazuela et al., 2020). Periodicity has huge implications on FRB progenitors: models that are purely sporadic cannot account for FRB 180916.J0158+65. This motivated various modifications to existing theories, described in §2.3. In some cases, periodicity is not expected in all FRBs because it is the result of a specific system configuration (e.g. if a NS progenitor exists in a binary system; Lyutikov et al., 2020, discussed in §2.3.1). Despite follow-up searches, no X- or γ-ray counterparts have been detected (Tavani et al., 2020).

2.2.5 FRB 200428: The First Potential Galactic FRB

Until very recently, a major challenge to FRB magnetar models (§2.3.1) was that the radio luminosity of FRBs exceeded that of any known Galactic magnetar bursts by many orders of magnitude. Then, in April 2020, an extraordinary two-component radio burst from SGR 1935+2154 was reported (Bochenek et al., 2020b; Andersen et al., 2020). This burst—FRB 200428—comprises two pulses separated by ∼37 ms that drift upwards in frequency. The 400−800 MHz burst energy of $\sim 3 \times 10^{34}$ erg is three orders of magnitude higher than any other Galactic magnetar to date. Although ∼40 times less energetic than the weakest extragalactic FRB detection (Marcote et al., 2020), the burst would be indistinguishable from a typical FRB if it resided in a nearby galaxy (Andersen et al., 2020). It thus appears that at least some FRBs are born of magnetars. Interestingly, Kirsten et al. (2020) report two bright bursts from SGR 1935+2154, suggesting the FRB may be a repeater.

The two bursts of FRB 200428 were preceded by up to 6 ms by a 1–250 keV X-ray burst (Mereghetti et al., 2020b; Ridnaia et al., 2020; Zhang et al., 2020b).[5] The X-ray burst has two hard peaks sep-

[5] Although uncertainties in timing measurements could affect this result (Margalit et al., 2020b)—see §2.3.1.1.

arated by ∼37 ms that that approximately align with the FRB pulses (Li et al., 2020a; Mereghetti et al., 2020a). This lends support to FRB theories that invoke magnetar bursts and giant flares (§2.3.1; e.g. Lyubarsky, 2014; Beloborodov, 2017; Kumar et al., 2017; Metzger et al., 2017; Margalit et al., 2020b).

Note that due to its lower energetics, some consider FRB 200428 to be an FRB-like event as opposed to a definite FRB. The situation is further complicated by the report by Kirsten et al. (2020) of two additional radio bursts, which together with the original FRB-like have an observed fluence that spans 7 orders of magnitude. It is unclear whether the bright bursts were formed by the same mechanism as the two bursts of FRB 200428. This raises the question of whether low luminosity radio bursts that can only be detected within the Galaxy can also be called FRBs. If not, at what point does a weak radio flash become an FRB? In this thesis, we will assume that FRB 200428 is an FRB, but this may be liable to change in the future.

2.3 Progenitor Models

A multitude of FRB theories have been proposed since the first FRB was discovered 13 years ago. Some invoke standard astrophysics, while others ascribe FRBs to more exotic physics or even the unknown. Courtesy of the Galactic FRB 200428 discovery (Bochenek et al., 2020b; Andersen et al., 2020), it is now known that at least some FRBs are associated with magnetars. Any FRB theory that does not involve magnetars can therefore only describe a subpopulation of FRBs. Indeed, given the broad array of FRB features and the high implied event rates, it is possible that multiple progenitor channels exist. Preference, however, should be given to theories capable of describing the full FRB population, and to theories that have observational backing or that can be tested. This chapter opens with one of the most likely FRB progenitors and closes with those that have been ruled out. In between is a rough ordering of likelihood, with the most exotic theories described near the end of the chapter.

2.3.1 Supernova Remnants: Magnetars

The flaring activities of magnetars have come to be one of the most promising—and well-studied—FRB candidates (Popov & Postnov, 2010, 2013; Kulkarni et al., 2014; Lyubarsky, 2014; Murase et al., 2016; Beloborodov, 2017; Kumar et al., 2017; Metzger et al., 2017; Margalit et al., 2020b). Arguments in favour are that: the high linear polarisation and large RMs observed for some bursts are indicative of a strongly magnetised central engine and environment (e.g. Masui et al., 2015; Michilli et al., 2018b; Gajjar et al., 2018; Osłowski et al., 2019); burst repetition rates are statistically similar to magnetar flares (Wadiasingh & Timokhin, 2019; Cheng et al., 2020); prolific repeaters (FRB 121102 and FRB 180916.J0158+65) occur near star-forming regions of their host galaxies (Bassa et al., 2017; Marcote et al., 2020; Tendulkar et al., 2021); and magnetar formation rates are suitably high to account for the full population of FRBs if they can emit FRBs for some sufficiently long period in their lifetime (Nicholl et al., 2017b; Beloborodov, 2020). Galactic magnetars, however, appear to be at odds with a number of FRBs, suggesting that at least some FRBs originate from a different type of magnetar to those local to the MW. For example, FRB 121102 has been active almost continuously for over 7 years, which calls for a magnetar that is very young or one interacting in a binary system (Beloborodov, 2017; Metzger et al., 2017) and possibly born in rare kinds of CC-SNe events (Metzger et al., 2017; Margalit et al., 2019; Zhong & Dai, 2020). This apparent discrepancy does not pose too much of a challenge: the wide range of FRBs observed implies a variety of magnetar types and environments (Margalit et al., 2019; Zhong & Dai, 2020; Marcote et al., 2020; Zhang et al., 2020a). That a Galactic FRB had not been observed posed a major challenge to magnetar models, however the recent association of FRB 200428 with SGR 1935+2154 (Bochenek et al., 2020b; Andersen et al., 2020) has alleviated some of this tension. Certainly, it appears that at least some FRBs are—in some way—powered by magnetars.

There are a number of magnetar flare theories for FRBs that can be broadly split in two groups (Simard & Ravi, 2020; Margalit et al., 2020b): those where emission occurs at heights of $r \lesssim 100\, r_{\rm NS}$ ("close in" models: low twist, curvature, and reconnection); and those where it occurs farther out ("far away" models: synchrotron maser blast waves). Here, $r_{\rm NS} \sim 10$ km is the radius of the NS.

2.3.1.1 *Far Away Models*

Magnetar outbursts eject relativistic flares, which create powerful shocks that propagate far beyond the magnetosphere. These magnetised, relativistic shocks naturally generate synchrotron masers whose emission may be consistent with FRBs. The high linear polarisation fraction and constant polarisation angle between bursts observed in some FRBs is in-keeping with shock emission models. Note that while close in models can arguably explain the range of observed temporal timescales (μs–ms) more naturally than far away models (see Tendulkar et al., 2021), the variations may be caused clumpiness in the medium where the shock front propagates or, possibly, propagation effects (Nimmo et al., 2021).

i) Magnetar wind nebula: The dissipation of the spin/magnetic energy of a pulsar/magnetar in a nebula will drive a wind of relativistic charged particles, i.e. a pulsar wind nebula (PWN) or magnetar wind nebula (MWN). Where the influence of the star ceases, the wind becomes sub-relativistic, creating a wind termination shock. Here, the PWN/MWN settles to form a shell (or bubble) within the SNR. Lyubarsky (2014) proposed that an FRB may be emitted when a magnetic pulse from an ultra-relativistic flare impacts a MWN (also see Murase et al., 2016). The pulse pushes plasma outwards to create a strong, magnetised and highly relativistic forward shock. At the shock front, Larmor rotation causes charged particles to gyrate in an unstable ring-like distribution function. This population inversion creates a powerful synchrotron maser (e.g. Gallant et al., 1992; Hoshino et al., 1992; Amato & Arons, 2006), whose emission is consistent with an FRB (Lyubarsky, 2014; Beloborodov, 2017; Plotnikov & Sironi, 2019). e^+e^- pairs are boosted to high Lorentz factors and instantaneously emit a burst of high energy X- or γ-rays through synchrotron emission, observable out to $\sim$100 Mpc (i.e. not detectable at cosmological distances; Lyutikov & Lorimer, 2016). For a SGR 1935+2154-like magnetar, with lower energies, the emission is expected in X-rays (Margalit et al., 2020b). The higher energy emission is expected to arrive before the FRB, which is at odds with timing by Mereghetti et al. (2020a), however this apparent discrepancy may be due to uncertainties in the timing measurements (Margalit et al., 2020b). The nebula may emit persistent radio emission—observable over cosmological distances—whose evolution over time may inform details of the underlying magnetar (Kashiyama & Murase, 2017; Dai et al., 2017; Yang & Dai, 2019; Li et al., 2020b). The termination shock has a relatively long recovery time and prolific repeaters cannot be accounted for in this model. To facilitate the short durations between bursts of FRB 121102, Beloborodov (2017) considers the collision between a giant flare and upstream medium left by a previous flare. Three models are described below, defined by the type of upstream medium considered.

ii) Baryonic shell: Metzger et al. (2019) take the upstream medium to be a sub-relativistic (effectively stationary) baryonic shell made from the ion tail of a previous flare. This was motivated by the observation of radio afterglow from a slow ejecta shell generated by the 2004 giant flare of SGR 1806–20 (Gelfand et al., 2005; Granot et al., 2006). Margalit et al. (2020a) formalise the model and provide a generalised methodology applicable to a broad range of magnetars. Using this, Margalit et al. (2020b) show that the γ-rays are unlikely to be detectable for cosmological FRBs, and that their short ($\sim$ms) duration and hard emission would differentiate them from the softer γ-rays from the giant flares of Galactic magnetars (e.g. Hurley et al., 2005; Palmer et al., 2005). Rescaling for an SGR 1935+2154-like magnetar again yields results consistent with the observed X-ray burst, where the apparent appearance of the X-ray burst after the FRB is assumed to be due to uncertainties in timing measurements. The downward drift in frequency observed in some FRBs (e.g. Hessels et al., 2019; Amiri et al., 2020) may be due to the deceleration of the blast wave and attenuation of the radio emission (due to Compton scattering), which causes the peak frequency and luminosity of the maser to decrease (Metzger et al., 2019; Margalit et al., 2020a). A defining feature of the baryonic shell model is a predicted neutrino counterpart generated by the photo-hadronic process (Metzger et al., 2020). Here—as in gamma-ray burst jets (Waxman & Bahcall, 1997; Mészáros & Waxman, 2001; Guetta & Granot, 2003; Dermer & Atoyan, 2003)—ions that are accelerated at the shock interact with the incoherent synchrotron (afterglow) radiation from the shock to form neutrinos.

iii) Spin-down-powered wind: Beloborodov (2020) considers the effects of the spin-down-powered wind between flares. The wind is expected to sweep the slow ion tail of a flare outwards,

behind which a hot wind bubble forms. The upstream medium with which a flare collides is thus a shell of relativistic e^+e^- pairs. The scenario is much the same as in Metzger et al. (2019), except that the synchrotron counterpart for a cosmological FRB is expected to be optical or X-ray. For an SGR 1935+2154-like magnetar, emission would peak in the optical/UV band (Margalit et al., 2020b).

iv) Plasmoids: Yuan et al. (2020), inspired by the coincident detection of two X-ray short bursts and FRBs from SGR 1935+2154, consider Alfvén waves from a magnetar quake. When crustal shear oscillations of a NS twist the magnetic field lines of the star, a low-frequency magnetohydrodynamic wave of oscillating ions is propelled into the magnetosphere to create X-ray bursts (Blaes et al., 1989; Thompson & Duncan, 1996). The relative amplitude of the wave grows as its distance from the star increases. Eventually, the wave breaks to form an island of closed magnetic field loops, known as a plasmoid (Bostick, 1956). The plasmoid is launched from the magnetosphere, where it quickly becomes a thin, relativistic pancake. The pancake pushes through the magnetospheric field lines, forcing them to snap and reconnect. This generates a strong wind behind the pancake, into which other plasmoids can collide and create a shock. Here, the FRB maser forms. An X-ray burst is emitted via dissipation of the blast wave. This model can effectively describe FRB 200428 and the associated X-ray bursts, but the analysis has yet to be extended to other FRBs.

2.3.1.2 *Close In Models*

i) Low-twist: Magnetar short bursts have been reported with quasiperiodic oscillations that may be associated with crustal magnetoelastic torsional oscillations (Huppenkothen et al., 2014a,b). Noting that the arrival time statistics of FRB 121102 are consistent with the short bursts of SGRs (e.g. Wang et al., 2018; Gourdji et al., 2019; Cheng et al., 2020; Lin & Sang, 2020), Wadiasingh & Timokhin (2019) draws a connection between low-altitude NS crustal quakes and FRBs. The slow dissipation of large-scale twists in a NS magnetosphere with high plasma density accelerates particles along closed field lines (through flux tubes) to emit short soft and hard X-ray bursts (Thompson et al., 2002; Baring & Harding, 2007; Beloborodov & Thompson, 2007; Beloborodov, 2012). In crustal slippage events, magnetic foot points may dislocate and induce electric currents. Given that such events happen over $\sim$1 % of the NS surface, most of the magnetic flux tubes involved are closed (Israel et al., 2008; van der Horst et al., 2012; Lin et al., 2012). If the plasma density in the immediate environment is sufficiently high, the electric field is screened. When the density is below the Goldreich-Julian density (Goldreich & Julian, 1969), however, the region may become charge-starved. This triggers intense pair cascades and pulsar-like emission (e.g. Philippov et al., 2020), observable as an FRB. In this way, all FRBs should be associated with X-ray short bursts, but—owing to the low-charge-density condition—not all X-ray short bursts would be associated with FRBs. The condition is met for objects whose magnetospheres have sufficiently low twist, e.g. for old magnetars whose twist has decayed along with the internal toroidal fields. Prolific repeaters would originate from rare aged magnetars with long spin periods (Beniamini et al., 2020). The age of SGR 1935+2154 is in line with model predictions, however its comparatively low dipole field strength may be a challenge (Margalit et al., 2020b). Since radiation occurs near the pulsar surface, the downward drifting subpulses in some FRBs may be attributed to radius-to-frequency mapping (Lyutikov, 2020; Wadiasingh et al., 2020), where different frequencies are radiated preferentially at different altitudes (Manchester & Taylor, 1977; Cordes, 1978).

ii) Curvature: It has been shown that two-stream plasma instabilities in magnetar magnetospheres can create particle bunches whose curvature radiation is consistent with FRBs (Kumar et al., 2017; Lu & Kumar, 2018; Yang & Zhang, 2018). In particular, Kumar & Bošnjak (2020) consider Alfvén waves launched by a magnetic disturbance near the NS surface (such as crustal motions or crust quakes). To remain stable, an Alfvén wave packet requires a non-zero electric current of electrons and positrons travelling in opposite directions along the magnetic field lines. The two-stream plasma instability creates particle bunches within the wave packet. As the distance from the NS increases, the plasma density decreases until the ambient e^+e^- density is too low to supply enough supporting current to the Alfvén wave packet, i.e. the region becomes charge starved. A strong electric field develops—whose

displacement current attempts to balance the plasma current density—which accelerates electrons and positrons in the clumps to relativistic velocities in opposite directions along the magnetic field lines. An FRB is released via the curvature radiation. X-rays are an expected counterpart: soft thermal X-ray emission near the surface from the initial energy discharge are inverse-Compton scattered by e^+e^- pairs to become hard X-ray spikes, consistent with those observed in Galactic FRB 200428 (Lu et al., 2020a). The wider opening angle for emission explains why numerous X-ray bursts are reported for SGR 1935+2154 without FRB detections. The downward drifting structure observed for some FRBs is naturally explained in this model: as the magnetic field lines of a magnetar cross the line of sight, the bunches that are viewed at later times have travelled farther along field lines, therefore reaching areas with less curvature and emitting at lower frequencies (Wang et al., 2019). In the case of FRB 200428, whose second pulse arrived at higher frequencies, it is possible that emission from the less curved region was seen earlier because the corresponding particle bunch was created sooner than the other (Wang et al., 2020b).

iii) Reconnection: Lyubarsky (2020) shows that—akin to the Crab and Crab-like pulsars (Uzdensky & Spitkovsky, 2014; Lyubarsky, 2019; Philippov et al., 2019)—FRBs can be formed by magnetic reconnection in the outer regions of a magnetar magnetosphere (also see Lyutikov & Popov, 2020). Consider a magnetic pulse from a giant flare (§2.3.1.1; Lyubarsky, 2014; Beloborodov, 2017; Yuan et al., 2020; Metzger et al., 2019; Margalit et al., 2020a), which propagates outwards as a fast magnetosonic wave to eventually meet the magnetar wind. In the magnetar wind, an equatorial current sheet separates the NS into magnetic hemispheres (e.g. Cerutti & Beloborodov, 2017). When the magnetic pulse arrives at the current sheet, violent magnetic reconnection causes the sheet to break (Lyubarsky, 2010; Gill et al., 2017). Small magnetic islands of oppositely charged pieces of current sheet fall into the magnetic pulse. These coalesce, forming radio pulses via reconnection, which are transported through the magnetar wind by the magnetic pulse and escape as FRBs. The FRBs and coincident X-ray bursts of SGR 1935+2154 are consistent with this model (Lyutikov & Popov, 2020). Radius-to-frequency mapping would be responsible for the observed downward frequency drift in some FRBs (Lyutikov, 2020; Wadiasingh et al., 2020).

2.3.1.3 *Ejecta Penetration*

When a magnetar is born in a SN, a large amount of ejecta forms a nebula around the star, which may inhibit FRB signals. In some cases, an FRB-emitting magnetar may not be surrounded by ejecta (e.g. Kashiyama & Murase, 2017; Dai et al., 2017; Yang & Dai, 2019), for instance: if it has been kicked from its birth site (Hobbs et al., 2005; Chatterjee & Cordes, 2004); it is born in a merger and moves away from its birth site (Dai et al., 2006; Giacomazzo & Perna, 2013); or it escapes its high-mass X-ray binary system when its companion star explodes (Bhattacharya & van den Heuvel, 1991). More generally, FRBs are only observable once the SN ejecta has become optically thin, which may take tens to hundreds of years (Piro, 2016; Murase et al., 2016, 2017; Piro & Burke-Spolaor, 2017; Lieu, 2017; Bietenholz & Bartel, 2017). As the SN ejecta expands and becomes more diffuse, the DM of bursts may decrease (Bietenholz & Bartel, 2017), however if it expands into dense ISM, the DM may remain constant or increase (Yang & Zhang, 2017; Piro & Gaensler, 2018). This is consistent with observations of FRB 121102, which has shown a DM increase of $1-2\,\mathrm{pc\,cm^{-3}}$ per year over the past 7 years (Hessels et al., 2019; Josephy et al., 2019; Platts et al., 2021).

2.3.1.4 *Flare Triggers*

A number of authors (e.g. Wadiasingh & Timokhin, 2019; Jiang et al., 2020) assume fracturing crusts of pulsars/magnetars (Thompson & Duncan, 1993) trigger the giant flares that create FRBs.[6] Wang et al. (2018) noted that the burst energetics of FRB 121102 approximately follow the Gutenberg-Richter law for earthquakes (Gutenberg & Richter, 1936), which describes the relationship between the magnitude and total number of earthquakes in a sequence. Indeed, it has already been shown that NS tectonic activity and crustquakes may be responsible for a number of events, such as pulsar glitches (Epstein & Link, 2000), SGR giant flares (Thompson et al., 2002;

[6] But see Lyutikov & Popov (2020), who assume plastic deformations of the crust (Levin & Lyutikov, 2012; Lyutikov, 2015) as opposed to crust quakes for reconnection models.

Colaiuda & Kokkotas, 2011; Zink et al., 2012) and X-ray outbursts (Thompson et al., 2017). In a starquake, the amount of time taken to build up energy for an FRB should correlate with the intensity of the FRB. Li et al. (2019a), however, show that there is no relationship between the wait times and intensities of the 170 pulses of FRB 121102 available at the time. The bursts thus may result from multiple, isolated fractures (Suvorov & Kokkotas, 2019).

2.3.1.5 *Magnetar Formation Channels*

An FRB-emitting magnetar may form in a variety of ways, each of which has implications on the FRB properties. Different FRB "types" (apparently one-off, hyper active, etc.) are thus thought to be created by different magnetar populations (Margalit et al., 2019, 2020b; Bhandari et al., 2020). For example, prolific repeaters may come from from young magnetars born in SLSNe/LGRBs and less active FRBs may come from magnetars born through BNS mergers or the accretion induced collapse (AIC) of WDs.

i) SLSNe/LGRBs: The host galaxy of FRB 121102 is an irregular, star-forming, low-metallicity dwarf (Chatterjee et al., 2017; Tendulkar et al., 2017; Marcote et al., 2017). This galaxy type is typical of LGRB and Type I SLSNe (Fruchter et al., 2006; Perley et al., 2016), which implies a connection between the resultant millisecond magnetars and FRBs (Metzger et al., 2017; Nicholl et al., 2017b). In this scenario, the large, decreasing RM and the persistent radio source of FRB 121102 is due to an expanding and continuously-energised magnetised ion-electron nebula within a young (6–17 years old) SNR (Tendulkar et al., 2017; Metzger et al., 2017; Margalit & Metzger, 2018; Margalit et al., 2018; Omand et al., 2018; Wang & Lai, 2020; Hilmarsson et al., 2021).

ii) BNS Mergers: The host galaxies of (for example) FRB 180924 (Bannister et al., 2019) and FRB 190523 (Ravi et al., 2019) are massive with low rates of star-formation, and are thus incompatible with SLSN/LGRB origins (e.g. Bhandari et al., 2020; Li & Zhang, 2020; Heintz et al., 2020). BNS mergers (and the associated sGRBs), on the other hand, are expected in all galaxy types (Belczynski et al., 2002). The ejecta is more diffuse and expands more quickly than in a CC-SN (e.g. Margalit et al., 2019). Hence, the nebula within the ejecta expands more rapidly, leading to a more rapid decrease in its density and magnetic field. This is consistent with the low RM and lack of persistent radio emission observed for FRB 180924 (Bannister et al., 2019; Margalit et al., 2019). Magnetars born in BNS mergers are expected to have large spatial offsets from their host galaxy centers, which could help distinguish FRBs born via this channel (Wang et al., 2020a). FRB 180924, FRB 180916.J0158+65 (localised to a massive spiral galaxy; Marcote et al., 2020) and FRB 190523, for example, have offsets of 4 kpc, 4.7 kpc and 29 kpc, respectively, which are consistent with BNS mergers from population synthesis models (Wang et al., 2020a). FRB sub-pulses may also evidence a BNS merger: FRB 181112 had four successive sub-bursts, with a ∼0.8 ms separation between the first and third pulse, and between the second and fourth pulse (Cho et al., 2020). This may indicate an underlying NS with a 0.8 ms rotation period, which is consistent with that formed in a BNS merger (Yamasaki et al., 2020).

iii) AIC of WDs: The AIC of WDs is expected to take place in a wide range of galaxy types. In particular, the host galaxy of FRB 180924 (Bannister et al., 2019) is consistent with galaxy types that are known to host AIC and Type Ia SNe (Margalit et al., 2019). Magnetars born via AIC may have spatial offsets due to natal kicks, however these are not expected to be as large as for BNS mergers. As with BNS mergers, the nebula expands more rapidly than the SLSNe case (Margalit et al., 2019). FRBs in this scenario would be accompanied by synchrotron radio emission from a PWN that lasts for a few months (Piro & Kulkarni, 2013).

iv) Binary WD Mergers: While binary WD mergers are currently the preferred formation channel of Type Ia SNe (Hillebrandt & Niemeyer, 2000; Pakmor et al., 2010, 2012; Hillebrandt et al., 2013; Maoz et al., 2014), some may collapse into stable magnetars (King et al., 2001; Shen et al., 2012; Schwab et al., 2016). If the resultant magnetar emits FRBs, these may be distinguished from other FRB sources by their DM and RM properties (Kundu & Ferrario, 2020). The ejecta is expected to be optically thin for ∼GHz radio emission immediately after the merger, and transparent for other radio frequencies tens of days later. When the ejecta interacts with ambient medium, the DM is predicted to increase—this in contrast to

CC-SNe—and the RM is predicted to decrease. The expected evolution of DM and RM are shown to be consistent with FRB 121102 (Kundu & Ferrario, 2020).

v) NS–WD Mergers: A magnetar capable of FRB emission may be formed by the merging of a NS and WD (Liu, 2020; Zhong & Dai, 2020). The FRBs are expected to have low activity levels, with properties akin to those associated with magnetars born via BNS mergers or AIC. The event rate of NS–WD mergers that form a stable NS (Paschalidis et al., 2011a,b; Margalit & Metzger, 2016) cannot account for the full population of FRBs with low activity levels, however magnetars born in NS–WD mergers may account for a subgroup of the FRB population (Zhong & Dai, 2020).

2.3.1.6 *Periodicity*

The detection of a 16.35 day period in FRB 180916.J0158+65 (Amiri et al., 2020)—and a tentative ∼157 day period in FRB 121102 (Rajwade et al., 2020b; Cruces et al., 2021)—motivated the expansion of magnetar flare theories. Proposed mechanisms by which periodicity may occur are described below. In all of these cases, periodicity is expected to be a special case that is owed to specific system configurations.

i) Tight binary system: Lyutikov et al. (2020) consider an FRB-emitting NS that orbits an OB-type star (also see Popov, 2020). The magnetar and the primary OB star's winds create a cone-shaped zone behind the pulsar, which sweeps out in a spiral due to the orbital motion. Depending on the pulsar phase, the propagation of radio emission may be inhibited by the wind, creating apparent activity periods. The authors demonstrate that such a scenario can successfully produce the ∼16 day period and 5 day duty cycle of FRB 180916.J0158+65, as well as the (possible) ∼157 day period of FRB 121102. Mild variations in DM are expected, as well as a high RM from the primary's stellar wind. The model also implies a longer activity period at higher frequencies. Observations of FRB 180916.J0158+65 by Pastor-Marazuela et al. (2020) challenge this theory: bursts are detected at 120 MHz (which is below the expected cut-off frequency; also see Pleunis et al., 2020), there is a smaller phase range at higher frequencies, and the DM is constant.

ii) Orbit-induced spin precession: If the FRB-emitter is a magnetar in a binary system with a compact object (either a stellar-mass BH, a NS or a WD), geodetic precession may occur. Here, if the spin angular momentum vector of the magnetar is misaligned with the orbital angular momentum of the system, the orientation of the magnetar's rotational axis will change/wobble (i.e. the magnetar will precess). A cone shape emanates from the emitting region of the magnetar, which traces a broad circle on the sky as the magnetar precesses. When the cone sweeps the line-of-sight, FRBs are visible. The scenario is shown to be in-keeping with the ∼16 day period of FRB 180916.J0158+65. The rate of precession is predicted to increase (i.e. the period will decrease) as the orbital separation decreases.

iii) Free precession: Initially mentioned in the discovery paper (Amiri et al., 2020), free precession has been considered by a number of authors to be the cause of periodicity in FRB 180916.J0158+65 (Levin et al., 2020; Zanazzi & Lai, 2020; Sob'yanin, 2020). The deformation of a NS by strong internal magnetic fields or electromagnetic forces induced by stellar rotation (considered in Sob'yanin, 2020) may cause a highly magnetic NS to precess (Pines & Shaham, 1974). The precession period may range from hours to weeks—satisfying requirements for both FRB 180916.J0158+65 and FRB 121102—and is predicted to increase over time (Levin et al., 2020).

iv) Forced precession by a fall-back disk: If a magnetar formed in a CC-SN is surrounded by matter with angular momentum—a fallback disk (e.g. Katz et al., 1994; Chatterjee et al., 2000; Alpar, 2001)—it may undergo forced precession (for a detailed discussion, see Qiao et al., 2003). An FRB-emitting magnetar in this situation may have a periodicity consistent with FRB 180916.J0158+65 and FRB 121102 (Tong et al., 2020).

v) Lense-Thirring precession: The Lense-Thirring effect is the relativistic correction to the precession of a massive rotating object (Thirring, 1918), i.e. the distortion of space-time is taken into account. Bardeen & Petterson (1975) showed that the inner region of a misaligned accretion disk around a NS or BH should undergo Lense-Thirring precession. If the disk

possesses more angular momentum than the compact object though, the disk will force the object to precess (Sarazin et al., 1980). In this way, a young magnetar may be seen to emit FRBs periodically (Chen, 2020).

vi) Ultra long rotation period: Beniamini et al. (2020) consider mature but relatively young magnetars ($\lesssim 10^4$ yr) with ultra long rotation periods. Most Galactic magnetars have spin periods of 1−10 s, depending on their age. Once the NS is $\sim 10^4$ years old, its magnetic field has decayed to the point that the spin-evolution of the magnetar essentially ceases, reaching a maximum period of ∼13 s (Viganò et al., 2013; Beniamini et al., 2019). If angular momentum is removed from a magnetar via external mechanisms, however, the spin period may become significantly longer. Beniamini et al. (2020) show there are at least three ways in which a magnetar can attain a 16 day spin period: i) mass-loaded charged particle winds (e.g. from giant flares), which expand the open magnetic flux of the star and enhance spin-down, ii) kicks from bursts, or iii) interactions with a SN fallback disk.

2.3.2 Supernova Remnants: Pulsars

2.3.2.1 *Giant Pulses*

A subpopulation of non-cosmological ($\leq$ 300 Mpc) FRBs may be generated by giant pulses of young millisecond pulsars (Keane et al., 2012; Cordes & Wasserman, 2016; Connor et al., 2016a; Lyutikov et al., 2016). The DM, RM and polarisation of an FRB is owed to the nebula surrounding the pulsar. A SN may be observable a few years prior to the onset of the FRB, but any other electromagnetic counterparts associated with giant pulses would not be observable (Lyutikov et al., 2016; Lyutikov & Lorimer, 2016). As the pulsar spins down, the radio flux of FRBs is expected to decrease (by $\lesssim 1$ Jy) on a timescale of several years (Kisaka et al., 2017). If the pulsar is an X-ray pulsar, FRBs may be accompanied by a bright X-ray source (Popov & Pshirkov, 2016).

2.3.2.2 *PWN Wind Bubble*

Analogous to the magnetar wind bubble model (Lyubarsky, 2014), an FRB may be produced in a pulsar wind bubble (Murase et al., 2016). Both NSs and magnetic WDs are considered. Afterglow from the reverse shock (e.g. Yang et al., 2016) would not be observable in either case, but emission from the expanding PWN may be observable for the NS. Should the NS be an X-ray pulsar, bright persistent X-rays may be observable (Popov & Pshirkov, 2016). As before, due to the inefficiency of rotationally-powered bursts, FRBs would be non-cosmological (e.g. Lyutikov, 2017).

2.3.2.3 *Newborn Highly Magnetic Pulsar*

Lieu (2017) presents a one-off FRB model based on the Schwinger mechanism; a prediction of quantum electrodynamics (QED) that e^+e^- pairs are spontaneously created in the presence of an electric field (Schwinger, 1951). When a highly magnetic pulsar is born with a high spin rate, the induced electric field may violently decay into e^+e^- pairs, which stream in opposite directions along open magnetic field lines near the polar cap region. The resultant burst of curvature radiation may be observable as an FRB. Unless the pulsar is rapidly spun-up later in life—perhaps by a companion—no repeat bursts are expected.

2.3.3 Binary Neutron Stars

The FRB–BNS models can be broadly divided into three classes: those emitted upon coalescence (§2.3.3.1), those emitted during the final inspiral (§2.3.3.2) and those emitted through the BNS interactions (§2.3.3.3 and §2.3.3.4).

2.3.3.1 *Mergers*

During the late stages of inspiral, after tidal disruption, the NS rotations in a binary system are predicted to become tidally locked (Bildsten & Cutler, 1992). As the BNS magnetic fields become synchronised, magnetic braking creates a powerful pulse of curvature emission consistent with one-off FRBs (Totani, 2013). While mass ejections will inhibit signal propagation (Hotokezaka et al., 2013), this should only appear ∼1 ms after the maximum rotation speed of the merged star

is reached (Yamasaki et al., 2018). This screening could be partially responsible for the short FRB timescales. Counterparts include: GWs (Abbott et al., 2017a; Abbott et al., 2020); a sGRB (Abbott et al., 2017b; Goldstein et al., 2017; Savchenko et al., 2017); radio afterglow (Hallinan et al., 2017; Duque et al., 2019); optical afterglow (Lyman et al., 2018; Paterson et al., 2020); X-ray afterglow (Haggard et al., 2017; Margutti et al., 2017; Troja et al., 2017); and a UV/optical-infrared (IR) transient from a kilonova (Evans et al., 2017; Valenti et al., 2017; Tanvir et al., 2017; Cowperthwaite et al., 2017). To date no FRB has been detected with the appropriate counterparts (e.g. Andreoni et al., 2017). Further, the event rate of FRBs is significantly higher than that of binary NSs (if each binary only produces one FRB; Luo et al., 2020).

If the binary merger leaves behind a stable, rapidly rotating NS, a repeating FRB may appear[7] once the ejecta has sufficiently dissipated (1–10 years after the initial burst; Yamasaki et al., 2018). The first burst is expected to be significantly brighter than those that follow—a feature evident in FRB 171019 (Jiang et al., 2020). The expected rate of repeating FRBs from BNS mergers as opposed to from CC-SNe, however, has since been shown to be only ∼6 % (Zhang et al., 2020a). The number of stable NSs that result should also be high (Gao et al., 2016), but observations of the GW 170817 BNS merger event imply long-term stability occurs in fewer than 3 % of NS binaries (Margalit & Metzger, 2019).

2.3.3.2 *Final Inspiral*

The interaction of BNS magnetospheres during their final approach may produce FRBs if: i) unipolar induction occurs; or ii) the BNS has a highly elongated orbit. The counterparts and model challenges are as in §2.3.3.1 above.

i) Unipolar induction: A toroidal magnetic field may be induced on the magnetic field lines of one NS by the other. Eventually the torodial field overwhelms the poloidal field and the circuit breaks down, releasing magnetic energy through reconnection (Lai, 2012). A single FRB is released (Wang et al., 2016), possibly with a double peak if the emission takes place over two orbital periods.

ii) Elongated orbit: In a dense region, a high number of NSs may capture each other and form close-pairs with highly elongated orbits. In such systems, the magnetic field flux changes rapidly upon approach, causing particle bunching and coherent curvature emission. Multiple FRBs may be produced during inspiral, but on a timescale of minutes (Dokuchaev & Eroshenko, 2017). The prolific repetitions of some FRBs (e.g. FRB 121102 and FRB 180301) are hence owed to numerous events in the same region.

2.3.3.3 *Neutron Star Combing*

Cosmic combing is the process by which a strong plasma stream sweeps a NS magnetosphere in an anti-stream direction (Zhang, 2017). This effect, where the magnetosphere is combed in an opposite direction to the stream, is caused by ram pressure—the resistance of a fluid to a body moving through it—and occurs when the ram pressure exceeds the magnetic pressure of the pulsar magnetosphere. This triggers magnetic reconnection, which creates a bright FRB (also see Zhang, 2018). In a system with a young, highly magnetised pulsar and a (companion) millisecond pulsar (or massive star), strong winds from the companion may comb the main pulsar magnetosphere and produce FRBs (Ioka & Zhang, 2020). The wind from the main pulsar clears a funnel-shaped path through the wind of the companion, allowing the FRB emission to escape. In particular, Ioka & Zhang (2020) consider FRB 180916.J0158+65. The observed periodicity can be attributed to the binary rotation period and the ∼5 day active window corresponds to the duration when the funnel points toward Earth. The RM would be low in this scenario, but the authors note that it would be significantly higher for an FRB nearby a SMBH. No direct counterparts are expected, however a massive star companion may be detectable if the FRB is close enough (e.g. FRB 190608 at ∼150 Mpc; Tendulkar et al., 2021).

[7] See §2.3.1.

2.3.3.4 *Binary System*

The magnetospheres of two NSs in a binary will interact repeatedly for decades to centuries prior to coalescence. During this time, numerous FRB bursting episodes may occur when magnetic field lines of different polarities collide and reconnect (Zhang, 2020). As the NSs approach each other, the burst rate is expected to increase; a feature that will be testable in the coming years. Quasiperiodicity may be evident from the rotation periods of the NSs (tens of milliseconds and seconds) and from the orbital period (hundreds of seconds). The DM contribution from the local environment is low, and hence should appear roughly constant over time. This is in contrast to FRB 121102, which has shown a DM increase (Hessels et al., 2019; Josephy et al., 2019; Platts et al., 2021). The RM contribution from the local environment is also expected to be low, unless nearby a SMBH. The polarisation angle and absolute value should remain roughly consistent between bursts.

2.3.4 Neutron Star and Companion(s)

2.3.4.1 *Neutron Star and Asteroids*

i) NS and asteroid: When a small body falls into a NS, tidal effects cause the body to radially elongated until eventually it reaches its Roche limit and fragments (Colgate & Petschek, 1981). Geng & Huang (2015) show that an asteroid captured by a NS may trigger emission consistent with an FRB (also see Huang & Geng, 2016). The model is versatile in that FRBs may arise in a number of situations; for example, Dai et al. (2016) extends this concept to a NS that travels through an asteroid belt and Bagchi (2017) to a variety of other NS–asteroid systems. Dai et al. (2016) also provides a detailed emission mechanism. When a radially elongated asteroid passes through the magnetosphere of a pulsar, an electric field is induced on the surface of the asteroid. Lorentz forces cause the electrons and ions in the interior of the asteroid to separate, causing a net charge near the surface. These electrons are stripped from the asteroid by the NS magnetosphere and accelerated to ultra-relativistic speeds to create a burst of curvature radiation. Depending on the system configuration, repetitions and periodicity are possible; for example, the ∼16 day period of FRB 180916.J0158+65 (and the possible ∼157 day period of FRB 121102) can be described by the passage of an old, slowly-spinning pulsar through the asteroid belt of a stellar-mass companion (Dai & Zhong, 2020). These prolific repeaters do, however, require very large asteroid belts (Smallwood et al., 2019; Du et al., 2020). Galactic FRB 200428 and the X-ray burst from SGR 1935+2154 can also be accounted for by the NS–asteroid model. Dai (2020) considers an iron-nickle (FeNi) asteroid of mass $\sim 10^{20}$ g that falls towards a magnetar with high proper velocity. Gravity tidally disrupts the asteroid, splitting it into two masses, which each trigger an FRB. The strength of the magnetic field tears the fragments apart, which are then accreted along the field lines and onto the NS poles. Upon impact, an e^+e^- fireball is launched from the NS surface to create an X-ray burst. For an in depth description of the X-ray burst formation, see Geng et al. (2020). One should note that X-rays formed this way are not expected to be observable from cosmological distances.

ii) Asteroid and pulsar wind: Mottez et al. (2020) presents an updated version of the FRB model presented in Mottez & Zarka (2014). The model was originally based on calculations in Mottez & Heyvaerts (2011), which studies the interaction of a relativistic pulsar wind and a small body that orbits the pulsar. A number of corrections to this work, however, were presented in Mottez & Heyvaerts (2020). One consequence is that the emission mechanism originally invoked to explain FRBs—a cyclotron maser activated in the Alfvén wings of the small body—is now inconsistent with observed FRB frequencies (Mottez et al., 2020). Authors leave the specifics of the emission mechanism to future work. To account for repeating FRBs, the model is updated to specifically consider a cloud or belt of 1–10 km sized asteroids orbiting a young millisecond pulsar. As asteroids pass through the pulsar wind, "multitudes of small erratic cosmic lighthouses" are created, observable as FRBs. Periodicity is given by the orbital period of the asteroids, and the 5-day phase window of FRB 180916.J0158+65 can be explained if the asteroids are clustered. The model favours young ($10-10^3$ year old) pulsars, which would likely be embedded in a nebula, but the influence of the nebula on the FRB signal is left for future work. Emission would be linearly polarised, and the high RMs observed in some FRBs would need to be attributed to a nearby magnetar or BH.

2.3.4.2 *Neutron Star and White Dwarf*

There are two models with NS–WD systems; one involves a collision and one involves interactions between the stars.

i) Collision: A one-off FRB may be emitted via magnetic reconnection when a NS collides with a WD (Liu, 2018). Upon coalescence, electrons from the WD surface are injected into the reconfigured field lines of the NS magnetosphere and emit a pulse of coherent curvature radiation. A Type Ia SN may be observable, followed by afterglow if the remnant is a BH with an accretion disk. As with NS–NS mergers (§2.3.3.1), the event rate of NS–WD mergers is too low to account for one-off FRBs (Luo et al., 2020).

ii) Interaction: Here a NS and magnetic WD with strong bipolar magnetic fields exist in a close binary system. When the WD reaches its Roche limit—where the NS tidal forces exceed the WD's gravitational self-attraction—some of its mass is violently transferred into the NS magnetosphere. This may trigger magnetic reconnection, accelerating the electrons to ultrarelativistic velocities to emit an FRB (Gu et al., 2016). If the WD is kicked away as a result of mass-loss and the conservation of angular momentum, the process may repeat. For an elliptical binary, there are times when the WD cannot connect with the Roche lobe, and the mass transfer is interrupted (Gu et al., 2020). This creates a natural duty cycle of ∼10 minutes to 2 days. To attain the ∼5 day duty cycle of FRB 180916.J0158+65, the system must have an unlikely eccentricity of $e > 0.95$. Accreted matter may also fragment, causing multiple bursts and lengthening the duration over which bursts are emitted, i.e. the bursts may continue for some time after the WD passes through periastron. The characteristic downward drift in frequency observed in repeating FRBs (e.g. Gajjar et al., 2018; Hessels et al., 2019) is owed to the relationship between the frequency of the curvature radiation and the Lorentz factor of the ultrarelativistic electrons: $\upsilon_c \sim \gamma^3$. Radiative effects near the NS surface may cause the Lorentz factors of electrons to decrease, resulting in lower frequencies being emitted at later times. Any counterparts are likely to be undetectable.

2.3.4.3 *Neutron Star and Black Hole*

Three models are presented here: the first considers the final inspiral of a BH and pulsar, the second considers a rapidly spun-up NS, and the third considers a primordial black hole (PBH) swallowed by a NS.

i) Inspiral: The relative motion a BH and a pulsar upon final inspiral may generate a Poynting flux (McWilliams & Levin, 2011). As the BH moves through the magnetosphere of the pulsar, charged particles in the pulsar magnetosphere are accelerated along the magnetic field lines to generate a one-off FRB (Mingarelli et al., 2015). When binned at 0.5 s, the sharp increase in luminosity may cause an apparent precursor 20–80% as bright as the main burst. A second FRB is triggered when the magnetosphere detaches from the pulsar (Falcke & Rezzolla, 2014, described in §2.3.7.1). These distinctive bursts would create a subpopulation of FRBs, and may appear with X- and/or γ-ray emission and GWs.

ii) Spin-up: A giant pulse may be triggered when a NS is rapidly spun-up by a nearby Kerr black hole (KBH), which could generate a one-off FRB (Bhattacharyya, 2017). The rotation of a massive object will distort the spacetime metric, causing the orbit of a nearby test particle to undergo Lense–Thirring precession (Thirring, 1918). For instance, as a BH spins, it will pull space and time around with it (i.e. frame-dragging). A nearby NS, which can be modelled as a gyroscope (e.g. Singh et al., 2014), will begin to wobble as it approaches the BH (Bardeen et al., 1972). Thus, as a slowly-spinning neutron star approaches a spinning BH, its spin-precession frequency should greatly increase (Kocherlakota et al., 2019). The newly rejuvenated pulsar is then expected to emit a giant pulse before it is swallowed by the KBH (Bhattacharyya, 2017). Such FRBs would form a subpopulation, and apart from GWs, no counterparts are expected.

iii) PBH collision: If a PBH collides with a NS (e.g. Abramowicz et al., 2009), the gravitational drag of the NS will cause the PBH to decelerate, allowing the NS to capture it. Once at the center of the star, the PBH will begin to accrete matter. Eventually, the NS will collapse into a BH, triggering an FRB (Abramowicz et al., 2018) in the manner described by Falcke

& Rezzolla (2014). Multiple non-periodic FRBs may occur if the magnetic field reconnects multiple times during the accretion process. The only expected counterparts are GWs.

2.3.4.4 *Neutron Star and Supernova*

If one of the NSs in a binary system becomes a SN, the shock will impact the magnetosphere of the companion NS, sweeping out a magnetsopheric tail (Istomin & Komberg, 2002). The resultant magnetic reconnection may power a burst of synchrotron emission consistent with a one-off FRB (Egorov & Postnov, 2009). The event rate of such a system, however, is far lower than that of FRBs.

2.3.5 Other Compact Bodies

2.3.5.1 *White Dwarf Mergers*

The coalescence of two WDs into a rapidly rotating, magnetised massive WD could induce FRB emission (Kashiyama et al., 2013). As the WD begins to merge, the rapid rotation drives inner magnetic fields to the surface of the stars via convection. The magnetic fields at the poles are twisted by differential rotation and magnetic instabilities, which triggers magnetic reconnection and a bright burst of curvature emission. X-ray emission may occur after if a debris disk forms around the newly born WD and/or a Type Ia SN if the merged WD exceeds the Chandrasekhar mass. The event rate dictates that FRBs born in this way would form a subpopulation.

2.3.5.2 *White Dwarf–Black Hole Merger*

As a WD approaches a BH, the WD will reach its Roche limit and its matter will be transferred to the BH. For a sufficiently large WD, the rate of transfer will be super-Eddington (brief and very intensive), leading to the formation of an accretion disk around the BH (Dong et al., 2018). High powered winds from the accretion disk can then create a corona. The process that follows is analogous to the coronal mass ejections observed in the Sun (e.g. Zhang & Low, 2005). Closed magnetic field lines run between the accretion disk and corona, which become twisted into rope-like flux structures by the turbulence in the accretion flow. When the mass-equilibrium threshold is reached, the rope snaps and is thrown outward as a blob of relativistic magnetised plasma (Yuan et al., 2009). When two blobs collide, magnetic reconnection powers sychrotron maser emission consistent with an FRB (Li et al., 2018). Only a handful of blobs may be released, and a maximum of 2–3 collisions are expected. X-ray emission from the accretion disk may be observable until the disk has been consumed by the BH.

2.3.5.3 *Black Hole Mergers*

Two one-off FRB models have been suggested using binary BHs, and both of them require that at least of one the BHs is a Kerr-Newman black hole (KNBH), i.e. is spinning and has a charge. GWs are expected from the merger in both models. The event rate of BH mergers is too low to account for one-off FRBs, and thus both models would only account for a subpopulation of FRBs (Zhang, 2016; Liu et al., 2016).

i) Inspiral: The charge of a spinning BH induces a global magnetic dipole normal to the orbital plane. As the BHs approach each other, the magnetic flux changes rapidly, driving a Poynting flux wind with increasing power. The resultant particle bunching leads to an FRB and possibly a sGRB (Zhang, 2016).

ii) KNBH discharge: Liu et al. (2016) propose that an FRB may be emitted when a KNBH discharges. In a binary system, the tidal forces of a companion BH may perturb the KNBH magnetosphere, causing part of the magnetosphere to detach. The reconnecting field lines sweep up surrounding plasma and accelerate it to relativistic speeds, resulting in curvature emission akin to an FRB. A shock is formed when the plasma collides with the surrounding medium, which drives relativistic particles. These cool through synchrotron radiation and inverse Compton scattering, producing radio and γ-ray afterglow (e.g. Gao et al., 2014).

2.3.6 Active Galactic Nuclei

The dynamics and energy scales of AGNs have inspired a number of FRB theories. These FRBs should be accompanied by persistent scintillating radio emission from the AGN accretion disk (as is possibly observed in FRB 121102; Marcote et al., 2017). In their current forms, the models detailed here do not allow for periodicity.

2.3.6.1 *Cosmic Combing*

Sporadic accretion by a low-luminosity SMBH may trigger isotropic disk wind outflows with varying ram pressure (Yuan et al., 2012). When this plasma stream interacts with a nearby NS (Zhang, 2018), cosmic combing (Zhang, 2017, described in §2.3.3.3) may produce FRBs. The RM of the bursts will vary periodically (on a timescale of weeks to months) depending on the orbital phase of the NS around the SMBH (consistent with FRB 121102; Michilli et al., 2018b).[8] Similarly, the polarisation angle may vary burst to burst, but should remain constant within a pulse envelope. The DM should remain roughly constant over time (in contrast to observations of FRB 121102; Hessels et al., 2019; Josephy et al., 2019; Platts et al., 2021).

2.3.6.2 *AGN Jet and Cavitons*

Through the Blandford–Znajek process, the magnetic field of a SMBH accretion disk can extract the BH spin energy (Blandford & Znajek, 1977), which can trigger two highly collimated relativistic jets (for a recent review, see Blandford et al., 2019). Through plasma instabilities, these relativistic e^+e^- beams create turbulence in coincident plasma. The resultant Langmuir waves (rapid plasma oscillations) induce a ponderomotive force on the plasma. When this force reaches equilibrium with the total pressure, electrons and ions separate into soliton-like[9] wave packets called cavitons (as in "cavity"; Zakharov, 1972; Wong, 1977). Strong electrostatic fields fill the cavitons, which accelerate jet particles to emit a pulse of bremsstrahlung radiation akin to FRBs (Romero et al., 2016). Repeating FRBs may be formed by episodic jets (Vieyro et al., 2017).

2.3.6.3 *AGN and Kerr Black Hole*

AGN accretion disk winds may provoke a nearby KBH into accreting the surrounding matter. The Blandford–Znajek mechanism could trigger jets from the KBH, which collide with the ambient plasma. The resulting shock waves would create a powerful maser via the process described by Waxman (2017). FRBs created in this manner are expected to repeat with sporadic disk winds (Gupta & Saini, 2018). If aligned appropriately, a GRB from the KBH may be observed with the FRB. Other counterparts are associated with the formation of the KBH: a Type Ib/c SN explosion (with neutrinos and GWs) when a supermassive magnetar is born, followed by gravitational waves and possibly γ-rays when the magnetar implodes into the KBH.

2.3.6.4 *AGN and Strange Star*

Strange stars (described in §2.3.7.6) may emit FRBs when AGN disk winds cause electrons close to the star's surface to oscillate (Gupta & Saini, 2018).

2.3.7 Other

2.3.7.1 *Neutron Star Collapse*

A one-off FRB may be emitted when magnetic braking causes a supramassive NS (a NS with a higher mass than the maximum limit for a non-rotating NS) to collapse into a KBH (Falcke & Rezzolla, 2014; also see Most et al. 2018). But for the FRB, the collapse is silent: the event horizon forms on the free-fall timescale (<1 ms), preventing most of the NS matter and radiation from escaping the BH. The no-hair theorem forbids magnetic fields from penetrating the event horizon. As such, the entire NS magnetosphere is shed, causing violent magnetic reconnection (e.g. Dionysopoulou et al., 2013) that powers an FRB. Since the validity of the no-hair theorem in NS collapse is a topic of debate (Lyutikov & McKinney, 2011), Punsly & Bini (2016) propose

[8] The RM of FRB 121102 varies but there is no obvious periodicity (Hilmarsson et al., 2021).
[9] A soliton is a solitary non-dissipative wave.

an alternative ejection mechanism: if the NS collapses into a KNBH, the BH may reach a lower energy state by the electric discharge of its EM field, forcing the magnetosphere to be shed. The only observable counterpart would be gravitational waves, perhaps preceded by X-ray afterglow and a GRB if the birth of the NS occured shortly before its collapse (Zhang, 2014).

A similar scenario is outlined by Fuller & Ott (2015), which involves regular NSs. Here, the lifetime of a NS may be significantly reduced if it lives in a high density region of dark matter (e.g. central regions of high density galaxies). The NS may capture ambient dark matter particles that scatter off its nucleons, greatly increasing its core density and leading to a collapse that may be observable today. However, such a process is speculative and—according to the authors—is intrinsically unlikely.

2.3.7.2 *Dicke's Superradiance*

Soon after demonstrating that the ISM is a suitable host for DSR (Rajabi & Houde, 2016a,b; Rajabi & Houde, 2017), the researchers noted the mechanism's applicability to FRBs (Houde et al., 2018a; Houde et al., 2018b). DSR was first verified experimentally in the 70s (Skribanowitz et al., 1973) and has since become an important part of quantum optics research. Following on from the brief description of DSR in §1.3.2.3, we now formalise the timescale of DSR. For a group of N molecules, the spontaneous emission of a photon with wavelength λ would occur independently for each molecule over a characteristic timescale $\tau_{\rm sp}$. Should the molecules be entangled and emit cooperatively, this timescale becomes:

$$T_{\rm R} = \tau_{\rm sp} \frac{8\pi}{3nL\lambda^2} \quad , \tag{2.3.1}$$

where the DSR molecule sample is a thin cylinder of length $L \gg \lambda$ and $n = \frac{N}{AL}$ is the inverted molecular density with A the cross-section of the cylinder. The timescale of cooperative spontaneous emission therefore decreases as N^{-1}. At the same time, the intensity of radiation increases as N^2 (Houde et al., 2018a), as opposed to linearly for N independent emitters. The quantum description of DSR dynamics leads to a characteristic time delay before the emission,

$$\tau_D \approx \frac{T_{\rm R}}{4} \left| \ln\left(\pi\sqrt{N}\right) \right|^2 \quad . \tag{2.3.2}$$

DSR requires a that a number of conditions be met: collisions must occur on a timescale $T' > \tau_D$, the entangled sample must be inverted and there must be strong velocity coherence (to enable interaction). DSR also has a minumum critical threshold for the inverted column density (Gross & Haroche, 1982),

$$(nL)_{\rm crit} \approx \frac{2\pi}{3\lambda^2} \frac{\tau_{\rm sp}}{T'} \left| \ln\left(\pi\sqrt{N}\right) \right|^2 ; \tag{2.3.3}$$

i.e. one requires that $nL > (nL)_{\rm crit}$ for emission.

The intensity and timescales in DSR naturally coincides with those of FRBs. The polarisation observed in some FRBs (e.g. Petroff et al., 2015a; Masui et al., 2015; Ravi et al., 2016; Caleb et al., 2018; Day et al., 2020) and the lack of polarisation in others may also be explained. Consider quantum state degeneracy. If a transition is degenerate, it has two or more quantum states with the same energy. On the contrary, a non-degenerate transition has only one quantum state. If DSR occurs in one non-degenerate transition, the signal is expected to be highly polarised. If degenerate transitions occur, the polarisation levels from the different states will combine and may reduce or cancel out the net polarisation. FRB repetition may be accounted for by the critical threshold $(nL)_{\rm crit}$: population inversion may increase until the threshold is reached, triggering DSR, after which the now quenched inversion may begin to build up again (assuming that some pumping mechanism is still active). However, it would be difficult for this mechanism to account for the periodicity observed in FRB 180916.J0158+65 (Amiri et al., 2020). In Houde et al. (2018b), the authors show that the critical threshold may be bypassed if the DSR is triggered by an external event; for example, if a young pulsar injects intense radiation into the DSR region. In this case, repetition would be induced by the pulsar and a (potentially convoluted) pattern of periodicity would occur. The only expected counterparts to DSR are those associated with the triggering event.

Should the FRB source be moving at an apparent relativistic velocity, DSR may account for spectro-temporal structures observed in some repeating FRBs (Rajabi et al., 2020), for example the sad-trombone effect and the predominance of downward frequency drifts. Under these circumstances, the model predicts an increase in bandwidth as frequency decreases; an effect that should be evident in sub-pulse drifting, as well as between pulses in different frequency bands. The former is visually patent in some repeaters (e.g. Gajjar et al., 2018; Hessels et al., 2019; Andersen et al., 2019; Fonseca et al., 2020), however the latter is less apparent.

2.3.7.3 *Pulsar Lightning*

Should pulsars have magnetospheric regions with distinct electrostatic energies that are separated by a vacuum, a lightning-type event may occur in a sudden transition from a high to low charge distribution. This release of stored electrostatic energy may lead to a burst of curvature radiation consistent with an FRB (Katz, 2017b). The number of FRB repetitions will depend on the pulsar spin-down time, and the variation in burst widths is attributed to scintillation in the magnetosphere. Signals are non-periodic and no counterparts are expected.

2.3.7.4 *AGN-like Wandering Beam*

Katz (2017c) proposes FRBs are formed in a scaled-down version of AGN, where the BH in question is moderately sized ($\sim 10^2$–$10^6\,\mathrm{M}_\odot$) as opposed to supermassive. The jets—which are aligned with the angular momentum of the BH—may wander if the BH accretes a chaotic medium (for example a giant molecular cloud in a starburst galaxy) that affects the BH angular momentum. If the beam wanders in a random walk, sudden changes in direction could cause the pulse pairs[10] observed in some FRBs (Katz, 2018). A burst of radiation may be observed as an FRB when a jet passes along an observer's line of sight. The mass of the BH constrains the intrinsic burst duration to less than a millisecond. The FRB will also be accompanied by persistent, variable radio emission from the off-axis jet and very soft X-ray/extreme UV emission from the accretion disk.

2.3.7.5 *Wandering Pulsar Beam*

Similar to the model proposed above in §2.3.7.4, FRBs may be pulsar beams that sweep across the sky (Katz, 2017a). Signals would have an underlying periodicity and, as with AGN-like wandering beams, pulse pairs are expected (Katz, 2018). No counterparts are suggested.

2.3.7.6 *Strange Star Crust*

Strange quark matter (SQM) comprises three types of quarks—up, down and strange—in approximately equal parts. The "strange matter hypothesis" or Bodmer–Witten assumption of stability states that quark matter is the true ground state of hadronic matter (Bodmer, 1971; Witten, 1984), i.e. nuclear matter is metastable and will decay into strangelets (bound particles consisting of one up, down and strange quark) under the right conditions. This signals the possible existence of strange stars (SSs): a type of quark star made of SQM. These stars are expected to be encased in a layer of hadronic matter. As the star accretes matter, this crust becomes heavier and may eventually collapse, leading to an enormous energy release. Zhang et al. (2018a) propose this as an origin of some FRBs.

A SS has an extremely thin ($\sim$1 fm) SQM surface from which extends a layer of electrons out to several hundred fm. The charge separation near the SQM surface induces an extremely strong electric field (Alcock et al., 1986), which can polarise normal matter in the vicinity and create a hadronic crust (Huang & Lu, 1997; Stejner & Madsen, 2005). Citing typical values given by Zhang et al. (2018a), for a SS with radius $r \sim 10^6$ cm, mass $M \sim 1.4\,\mathrm{M}_\odot$ and surface temperature $T_s \sim 3 \times 10^7$ K, its crust is expected to have a mass of $M_c \sim 10^{-7}\,\mathrm{M}_\odot$–$10^{-5}\,\mathrm{M}_\odot$ and a thickness of $l \sim 2 \times 10^4$ cm. For the crust to remain stable, it must sit sufficiently far (~ 200 fm) from the SQM surface. This ensures only a limited number of ions can tunnel through the Coulomb barrier to the SQM core (Alcock et al., 1986). As the SS accretes more matter, however, the crust becomes more massive and the gap between the crust and the SQM surface decreases. As more ions reach the surface, they are converted into SQM and heat the SS surface. Consequently, the electric field

[10] See Chapter 4 for a detailed discussion on pulse pairs.

and the width of the gap are further reduced (Kettner et al., 1995) and more ions may tunnel until finally the crust collapses. The crust falls into the SQM core, taking its magnetic field lines with it. Magnetic reconnection accelerates electron and positron pairs to ultra-relativistic speeds along the magnetic field lines, emitting a burst of curvature radiation.

While X- and γ-ray emission may accompany these signals, it is unlikely that they would be detectable.[11] The model struggles to account for repeaters, as one would require that the hadronic crust be rebuilt, and this would take some time ($\sim 10^9$ yr).[12] The low event rate for SS crust collapse dictates that FRBs formed in this manner would represent a subclass of the full FRB population.

2.3.7.7 *Quark-Nova*

The explosive collapse of a NS to a quark star is known as a quark-nova (QN). As an old, isolated NS spins down, the core density increases. At a critical density, $\rho_{\rm NS,cr}$, quark deconfinement is triggered, whereby neutrons are split into quarks (e.g. Itoh, 1970; Olinto, 1987). The outer layers of the NS crust are expelled at relativistic velocities, leaving behind a quark star. Three QN–FRB theories have been proposed: i) the decay of the ejected nuclei (Shand et al., 2016); ii) the creation of a plasma beam by the collisionless plasma formed by the ejecta (Ouyed et al., 2020a); and iii) the collision of the ejecta with ambient medium from the parent NS's birth in a CC-SN (Ouyed et al., 2020b). In all of this cases GWs from the QN may be observed, and EM counterparts would depend on the local environment of the quark star (Ouyed et al., 2011).

i) β-decay of ejecta: The ejected nuclei undergo a rapid neutron-capture process (r-process), where a succession of neutrons merge (i.e. are captured). The nuclei then go through a rapid series of β-decays (e.g. Jaikumar et al., 2007), emitting electrons in the strong, ambient magnetic field. This creates a powerful burst of radio synchrotron emission, observable as an FRB (Shand et al., 2016). This model, however, implies a burst duration of seconds as opposed to milliseconds. To account for this, authors argue that the de-dispersion process incorrectly aligns the FRB emission frequencies and that the signal is made up of a series of extremely short bursts that cannot be resolved. The fine structure observed in FRBs (e.g. Hessels et al., 2019) suggests this is not the case.

ii) Plasma beam: The following scenario is predicted to create repeating FRBs (Ouyed et al., 2020a). After $\sim 10^8$ years, an old, isolated NS may find itself embedded in the ICM of galaxy groups and clusters. When the NS collapses, chunks of the ejected crust expand as they become heated by collisions with ambient protons, until eventually they become collisionless. The interaction of these chunks with the magnetised ICM generates plasma instabilities, which trigger synchrotron emission. The time delay between pulses is determined by the angular separation between the chunks, and is found to be roughly constant with a typical value of $12 < \Delta t_{\rm repeat} < 24$ days. Apparent periodicity may be evident if chunks have roughly equal spatial separation and if the viewing angle allows. The polarisation degrees and high RMs observed in some FRBs cannot be accounted for in this model, unless the QN occurs within a galaxy.

iii) Ejecta collision with PWN: This model considers the collapse of a massive NS into a quark star a few years after the birth of the NS in a CC-SN. When chunks of the ejected NS crust collide with the expanding PWN shell, plasma instabilities cause particle bunching, which triggers a burst of sychrotron emission consistent with one-off FRBs (Ouyed et al., 2020b).

2.3.7.8 *Axion-Based Models*

Axions are hypothetical bosons originally proposed as a resolution to the strong CP (Charge+Parity) problem in QCD (Peccei & Quinn, 1977a,b) and today are well-motivated dark matter candidates (see Pargner, 2019, for a recent review). It has long been known that a self-gravitating Bose gas can form stable clumps (Kaup, 1968; Ruffini & Bonazzola, 1969). For axions, clumping is induced by the violent homogeneous evolution of their fields post-inflation (Hogan & Rees, 1988). The

[11] Quark stars may emit gravitational waves via their oscillation modes (Gondek-Rosińska et al., 2003), but I do not include them as a counterpart for any of the FRB–quark star models, as they are unlikely to be detectable.

[12] Though perhaps if only a portion of the crust collapses, it could rebuilt more quickly.

resultant "miniclusters" would have masses and radii of $M_{\rm mc} \sim 10^{-12}\,{\rm M}_\odot$ and $R_{\rm mc} \sim 10^{12}\,{\rm cm}$ (Hogan & Rees, 1988; Kolb & Tkachev, 1993, 1994) and, should they exist, would be the dominant form of dark matter in the Universe. In the center of miniclusters, axion (Bose) stars may form (Tkachev, 1986; Kolb & Tkachev, 1993, 1996) as the miniclusters lose kinetic energy. Axions may also form clouds around spinning KBHs (Arvanitaki et al., 2010; Arvanitaki & Dubovsky, 2011). A bosonic wave field can extract rotational energy from a spinning BH via superradiance if its frequency is within a certain range with respect to the angular velocity of the BH (Zel'Dovich, 1971; Misner, 1972; Press & Teukolsky, 1972; Vilenkin, 1978). The bosonic wave is amplified and the field may grow exponentially until the system becomes unstable (Damour et al., 1976; Zouros & Eardley, 1979; Detweiler, 1980). Stimulated decay may occur, where a QCD axion decays into two photons (Srednicki, 1985).

Numerous FRB models involving axions have been put forward, all of which assume dark matter is predominantly composed of axions.

i) Axion star and NS: One of the first axion-based FRB models considers the collision of an axion star with a neutron star (Iwazaki, 2014, 2015). Under strong magnetic fields, axion stars produce oscillating electric fields (Iwazaki, 1999), which could cause electrons on the NS surface to radiate coherently. A similar model has been proposed by Raby (2016), where emission is from neutrons in the upper NS core. The tidal effects, however, would break an axion star apart long before it could reach the NS surface (Pshirkov, 2017). Further, the plasma would be too dense for radio emission to penetrate (Pshirkov, 2017) and the electric susceptibility of the plasma in this region would not allow for a powerful enough radiation mechanism (Bai & Hamada, 2018). To resolve this, Buckley et al. (2020) propose that emission occurs when an axion star passes through a resonant region of a NS. Here, the photon mass—given as a position-dependent effective plasma mass—equals the axion mass. Via the Primakoff effect (the resonant production of neutral mesons by photons interacting with an atomic nucleus), resonance causes axions to produce a powerful burst of radio emission. Repeating FRBs may occur should parts of the axion star break off and fall through the resonant region of the magnetosphere at different times.

ii) Axion quark nugget and NS: An axion quark nugget (AQN) is a composite object of axions and standard quarks (Zhitnitsky, 2003), an idea stemming from quark nuggets (Witten, 1984). An AQN falling through the magnetosphere of a NS will cause magnetic reconnection, triggering a giant flare whose emission may be consistent with FRBs (Van Waerbeke & Zhitnitsky, 2019). All FRBs are expected to repeat (without periodicity), where the frequency of repetition is given by the local dark matter density. Since a curvature radiation mechanism is invoked, direct emission counterparts are not expected to exceed mm/infrared frequencies.

iii) Axion miniclusters: Radiation passing through an axionic medium will be amplified, leading to parametric instabilities that could form a powerful maser (Tkachev, 1986). Since the mass of an axion is $\mu{\rm eV} \lesssim m_a \lesssim {\rm meV}$, its decay may have an emission frequency in-keeping with that of FRBs: $\nu = m_a/2\pi \approx 2.4(m_a/10\,\mu{\rm eV})\,{\rm GHz}$. With an energy budget of $M_{\rm mc} \sim 10^{-12}\,{\rm M}_\odot = 2\times10^{42}\,{\rm ergs}$, the explosive decay of a small fraction of a minicluster could result in an FRB-like signal (Tkachev, 2015; also see Levkov et al., 2020). If the axions are coupled to gravitons, a short burst of gravitational waves may accompany the FRB (Sun & Zhang, 2020).

iv) Axion star and BH: If an axion star orbits a BH with a highly magnetised accretion disk, it may collide with the matter to produce multiple FRBs (Iwazaki, 2017). The mechanism is similar to the axion star and NS model proposed by Iwazaki (2014, 2015): the strong magnetic field induces oscillating electric fields on the axion star, which causes electrons in the accretion disk to oscillate and radiate coherently. The central frequencies of the bursts depend on the rotation speed of the accretion disk at the point of impact, where the intrinsic frequencies are Doppler shifted (Iwazaki, 2020). Periodicity is not accounted for in this model. Should one-off FRBs originate from axion stars and NSs, the stronger magnetic fields implies the peak flux densities of the bursts should be greater than those of repeaters (Iwazaki, 2020).

v. Axion cloud and PBH: Rosa & Kephart (2018) propose superradiant instabilities around spinning BH as a source of FRBs. Here, the energetics of FRBs dictate that the BHs be primordial

($M_{\rm PBH} \lesssim 0.01\,{\rm M}_\odot$). The axions in clouds surrounding the PBHs may undergo stimulated emission, which forms a powerful laser. Since PBHs are formed when gas overdensities collapse (García-Bellido et al., 1996) and are unlikely to spin-up via accretion (Ali-Haïmoud & Kamionkowski, 2017), the spinning PBHs considered are assumed to have formed in PBH mergers. Multiple bursts are possible in this model. The electric field created by the laser in the axion cloud would induce significant pair production, creating a dense e^+e^- plasma. At some critical density, the plasma would inhibit the laser. e^+e^- annihilation then reduces the plasma density, after which lasing may restart. Bursts generated in this way are known as "black hole bombs" (Press & Teukolsky, 1972). Possible counterparts may be associated with the e^+e^- annihilation. If positronium (an unstable, bound e^+e^- pair) is created during e^+e^- annihilation, an afterglow of γ-rays may occur. GWs may also occur if the axion cloud partially collapses between bursts.

2.3.7.9 *Cosmic Strings*

Cosmic strings are hypothetical, one-dimensional concentrations of energy that represent remnants of symmetry breaking in the early Universe (Kibble, 1976). These topological defects have yet to be detected directly, but should they exist their gravitational effects are expected to leave signatures on cosmological observations. It was originally believed that cosmic string loops may contribute to large scale structure formation (Vilenkin, 1981), but it has since been shown that the contribution of cosmic strings to the CMB is at most 10% (e.g. Albrecht et al., 1997; Contaldi et al., 1999). Since a cosmic string is one-dimensional, its rest energy can be quantified by a string tension $G\mu \leq 10^{-7}$ (current constraint; Planck Collaboration et al., 2014; Charnock et al., 2016), where G is Newton's constant. While cosmic strings do not drive galaxy formation, they may be seeds of high redshift SMBHs (Bramberger et al., 2015) or globular clusters (Barton et al., 2015), and may play an important role in other high-energy physical processes. One such example is FRBs. In this context both neutral and superconducting cosmic strings (SCSs) have been considered. The former radiate via cusp decay and the latter through a coupling to electromagnetism.

i) Neutral: The rapid (relativistic) vibration of cosmic strings can lead to the formation of cusps and kinks, which in turn may separate into isolated loops. A cusp is a singularity at the point where a string doubles back on itself and a kink is a point at which a string violently (discontinuously) changes direction. Both structures decay in a burst of radiation (Brandenberger, 1987). In particular, Brandenberger et al. (2017) considers the decay of cusps as potential source of FRBs. Cusp decay (or annihilation) is capable of producing photons in all frequency ranges, and has been considered as a source of various types of astrophysical radiation, e.g. γ-rays (MacGibbon & Brandenberger, 1993), neutrinos (MacGibbon & Brandenberger, 1990) and GRBs (Brandenberger et al., 1993). Radio emission from cusp annihilation may have sufficiently high energy flux to allow for detection and may have an occurrence rate comparable to FRBs (Brandenberger et al., 2017). Note, however, that the event rate may in fact be too high when relativistic effects are taken into account (Costa et al., 2018). The timescale of cusp decay is significantly smaller than that of FRBs, and hence the observed duration is owed to propagation effects. While repetition may be possible, for example if one loop has many cusps, single FRBs would be dominant, which is contrary to findings by Ravi et al. (2019) based on FRB event rates. Even if there are multiple cusps on a string, repetition may be difficult to attain, as the beaming direction would have to remain roughly consistent for each decay. It follows that periodicity would not be possible. The radio emission from cusp decay should be accompanied by other frequency counterparts. In particular, Brandenberger et al. (2017) predict a significant optical counterpart, however this has yet to be observed.

ii) Superconducting: When a cosmic string carries charge, the oscillations under the string tension will induce electromagnetic radiation. SCSs were first considered in an FRB context by Vachaspati (2008), who proposed beamed emission from cusps as a source of the Lorimer Burst. The type of SCSs considered are not expected to reside in galaxies (also see Zadorozhna, 2015), however in rare cases a cluster of loops may form a halo around a galaxy (Yu et al., 2014). This, of course, is contrary to the numerous localisations of FRBs to host galaxies. Emission from kinks and kink-kink collisions have also been considered (Cai et al., 2012b; Ye et al., 2017), the latter of which is too weak to be detected. Radiation from cusps and kinks is expected to be linearly polarised (Cai et al., 2012a,b), which—given the wide range of observed FRB polarisation fractions—presents another challenge. Further, FRBs

generated by SCSs are one-off signals. SCSs could thus only account for a small subpopulation of FRBs. Possible counterparts are GWs and neutrinos, although it is not clear whether either would be detectable.

2.3.7.10 *Cosmic Superstrings*

Superstring theory—shorthand for supersymmetric string theory—attempts to model all fundamental particles and forces as the vibration of supersymmetric strings (for a recent review, see Chernoff & Tye, 2015). This is in contrast to bosonic string theory, which does not consider fermions, i.e. it does not incorporate supersymmetry: the relationship between bosons and fermions. Similar to the emission of photons by cosmic strings, cosmic superstring loops emit axions and gravitons. The former may generate FRBs when they decay to photons in the presence of a strong magnetic field[13] (Chernoff et al., 2020). A superstring may emit multiple FRBs; and if the string is rotating, there would be an underlying periodicity. Gravitational waves are expected to accompany the bursts.

2.3.7.11 *Dipole Collisions*

Thompson (2017a,b) consider the collision of two macroscopic (>10 cm) dipoles as a possible origin for FRBs. These relativistic field structures are thought to form during cosmic electroweak symmetry breaking and are a close cousin of cosmic strings. The dipoles presented are dubbed large superconducting dipoles (LSDs): large because they are macroscopic and superconducting because they have maintained an electric charge on a cosmological timescale. Upon impact, the energy is released in a thin, ultra-relativistic, magnetised shell, which sweeps up nearby electrons, triggering a burst akin to an FRB. Higher energy emission may also occur, of which only high frequency radio would be detectable. LSDs may collide either within dark matter galactic halos or near the centers of SMBHs. In the former environment, collisions would be rare, leading to one-off FRBs. Near SMBHs, LSDs may form gravitationally bound cusps, within which frequent collisions may occur. This hypothesis implies FRBs with high RMs must eventually repeat. Emission from LSDs is also expected to be highly linearly polarised.

2.3.7.12 *White Holes*

Originally proposed to help alleviate the BH information paradox (Rovelli & Vidotto, 2014), Planck stars have been suggested as the origin of one-off FRBs (Barrau et al., 2014). As a star collapses, it may reach a critical density at which point quantum gravity comes into effect. Heisenberg's uncertainty principle—which limits the extent to which the position and momentum of a particle can be measured simultaneously—creates a quantum gravitational repulsion that forces the star to bounce and violently explode (e.g. Frolov & Vilkovsky, 1982; Stephens et al., 1994; Barceló et al., 2014; Haggard & Rovelli, 2015; Ben Achour et al., 2020; for a review see Malafarina, 2017). The existence of white holes (WHs) was first postulated by Igor Dmitriyevich Novikov in 1964, and the possibility of observing them was evidenced a decade later (Narlikar et al., 1974). Owing to their long lifetimes, the deaths (or bounces) of stellar black holes are unlikely to be observed. PBHs formed in the early Universe (Carr, 1975), however, may be exploding today. The wavelength of such a signal is roughly consistent with that of FRBs (Barrau et al., 2014, 2018), however no further similarities between the events are drawn. γ-rays in the TeV range may accompany FRBs, however such high energy bursts are yet to be detected.

2.3.7.13 *Radial Dark Matter Flow Stars*

A radial dark matter flow (RDM) star is a type of Planck star that, instead of bouncing, finds itself in equilibrium. Klimenko et al. (2017) show that if the radial flow of dark matter in spherical regions surrounding a Planck star is balanced, the mass bounded by the regions is conserved in a time-independent solution. Nikitin (2018) propose these hypothetical RDM stars as a possible source of FRBs. Should an object of asteroid mass fall onto an RDM star, tidal forces will tear the matter into its constituent nucleons (or even quarks), which will be boosted to ultra-relativistic velocities by the gravitational field of the RDM star. These particles are scattered by the core of the star, pumping the Planck particles into an excited state. A laser is triggered as the excited

[13] See §2.3.7.8.

states decay into photons. The resultant emission is within the observed frequency range for FRBs. MW-like galaxies are shown to be suitable hosts (Nikitin, 2019) and repetition can be expected if multiple bodies collide with an RDM star. No counterparts are specified in this model.

2.3.7.14 *Alien Civilisations*

Two models consider intelligent extraterrestrial beings as a source of FRBs. While these proposals ask important questions about life outside of our tangible world, they do belong at the lower end of the likelihood scale.

i) Communication: Luan & Goldreich (2014) were the first to consider extraterrestrial beings as a source of FRBs. Advanced civilisations would have identified neighbouring planets with a propensity for life and would be aware of the power of radio bursts as a communication mechanism. As such, they may reach out to other civilisations by transmitting narrow beams of pulsed radiation. The authors show that a modest amount of power would be needed for an array of small telescopes to transmit an FRB. In this scenario, all FRBs would eventually be observed to repeat. No counterparts directly related to the FRB would be expected.

ii) Light sails: Lingam & Loeb (2017) consider a scenario in which FRBs are a result of beams that accelerate extragalactic light sails.[14] The diameter of the beam emitter D is derived in two ways: via energy requirements and by considering engineering constraints. Both (rather serendipitously) give a characteristic value of $D \sim 3 \times 10^9$ cm, which is approximately twice that of Earth. This is somewhere between the size of a super-Earth and mini-Neptune (Rogers, 2015). The emitter size could be consistent with some kind of Stapledon-Dyson sphere (Stapledon, 1937; Dyson, 1960).[15] The frequencies required to power the light sail are shown to be akin to those of FRBs. There would be no accompanying counterparts and all events would be repeaters. The authors estimate that light sails within the MW would be observed once every 30−1500 years (also see Maoz & Loeb, 2017). Should a light sail be accelerated from within our own Galaxy, the expected flux-density would be $S_\nu \sim 10^{10}$−10^{11} Jy. This far exceeds that of FRB 200428 ($S_\nu \sim 10^5$ Jy). To account for this, the Galactic FRB must either be part of a separate FRB population or it must emanate from a significantly less powerful emitter (e.g. one for inter-planetary travel). In the latter case, however, the authors state that such an event would have flux densities too low to be detectable.

2.3.8 Void

Here we recount models that have successfully been ruled out. Note, however, that some of the models detailed above are highly speculative and may be difficult to definitively falsify.

2.3.8.1 *Annihilating Mini Black Holes*

Shortly after the second FRB observation (Keane et al., 2011), Keane et al. (2012) considered—and swiftly ruled out—evaporating black holes as possible sources of single FRBs. In this scenario, a BH of mass $M_{\rm BH} < 10^{13}$ kg may evaporate to some critical mass $M_{\rm crit}$ before violently releasing the remaining energy $E = 10^{30}\, M_{\rm crit}^{-1} c^2$ as a "fireball" of relativistic particle pairs. These would expand into the magnetic field of the ISM to create a burst of radio emission (Rees, 1977; also see Blandford et al., 1977). Such emission, however, would only be observable out to ∼200 kpc—far shorter than the DM-implied distance of the Lorimer Burst (Keane et al., 2012). Further, Rees is quoted as saying that the physics proposed at the time is no longer thought to be applicable (Cordes & Chatterjee, 2019).

2.3.8.2 *Stellar Coronae*

The proposal of Galactic flare stars as FRB progenitors (Loeb et al., 2014) caused a fair amount of debate from the outset. Flaring dwarf stars ($M \sim 0.5\,{\rm M}_\odot$) have been observed to emit radio

[14] A light sail is a spacecraft that is propelled by radiation pressure.

[15] "Stapledon-Dyson sphere" is a different naming convention to the more commonly used "Dyson sphere." It gives credit to Olaf Stapledon, who first came up with the concept in his 1937 science fiction novel "*Star Maker*," as well as to Freeman Dyson, who formalised the idea in his 1960 paper "*Search for Artificial Stellar Sources of Infra-Red Radiation*." Reportedly, Dyson himself would rather the concept was not his namesake.

bursts over timescales $< 5\,\mathrm{ms}$ (e.g. Lang et al., 1983; Lang, 1986; Gudel et al., 1989; Bastian et al., 1990) and had been observed within the field of view of the 10 FRBs detected at the time (Maoz et al., 2015). A cyclotron maser may form by the bunching of electrons on the magnetic field of the star (Güdel, 2002). Should the resultant burst occur near the base of the coronae—or induce coronal mass ejections (Drake et al., 2013)—the radiation would pass through a sheet of plasma and increase the observed DM. The free-free absorption absorption in a medium with the required DM, however, may render the signal unobservable (Luan & Goldreich, 2014). The authors claimed that even a very hot corona would be incapable of explaining the lowest DM of the FRBs reported at the time ($\sim 553\,\mathrm{pc\,cm^{-3}}$). Coronae that are hotter still may also cause a deviation from the observed time-frequency relationship (Tuntsov, 2014; Luan & Goldreich, 2014; Dennison, 2014, see §1.4.1). Maoz et al. (2015) contest both of these claims by citing observations by Getman et al. (2008a,b). Here, pre-main-sequence stars show X-ray flares with temperatures high enough to avoid significant free–free absorption. These flares, as well as observations of a radio flare star by Osten & Bastian (2008), are used as a proof of principle to show that the ν^{-2} frequency sweep could exist for radio flares (however the radio star in question did not conform to such a relationship). It was not long before the theory was finally laid to rest, when Masui et al. (2015) showed that the DM of the newly observed FRB 110523 would require an unphysically dense and extended stellar corona. Since then, the extragalactic nature of FRBs has become definitive.

2.3.9 Summary

While dozens of theories attempt to explain FRB origins, it is gradually becoming clear which models are more or less likely. Magnetars (§2.3.1) are—unsurprisingly—perhaps the most highly regarded theory. Asteroid models (§2.3.4.1) are also considered quite widely, given their flexibility and applicability to a wide range of observations. On the other hand, Occam's razor negates more abstract or untestable theories (e.g. aliens). Over the next few years, thousands of FRBs are expected to be detected, which should greatly aid in further narrowing down likely progenitor channels. Observables that will be particularly illuminating are: periodicity (rotational or activity periods), galaxy hosts and local environments, and counterparts. A large number of theories may be ruled out by counterparts (particularly more exotic theories). The identification host galaxies and local environments—as well as the prevalence of periodicity—will help map FRBs into potential population groups and ultimately reveal probable origins.

	Progenitor	Mechanism	Counterparts	Constraints/Notes	Type	References
SNR	MWN	Magnetar flare	– X-/γ-ray burst ($\sim$100 Mpc)	– Cannot account for prolific repeaters.	Repeat	Lyubarsky 2014
	Baryonic Shell	Magnetar flare	– X-/γ-ray burst ($\sim$100 Mpc) – Neutrinos	– Periodicity possible.	Repeat	Metzger et al. 2019
	Magnetar Wind	Magnetar flare	– Optical/X-ray burst ($\sim$100 Mpc)	– Periodicity possible. – Optical burst if Galactic.	Repeat	Beloborodov 2020
	Plasmoid	Magnetar flare	– X-ray burst	– Applied to FRB 200428.	Repeat	Yuan et al. 2020
	Low-twist	Magnetar flare	– X-ray burst	– Periodicity possible.	Repeat	Wadiasingh & Timokhin 2019
	Curvature	Magnetar flare	– X-ray burst	– Periodicity possible.	Repeat	Kumar et al. 2017 Kumar & Bošnjak 2020
	Reconnection	Magnetar flare	– X-ray burst	– Periodicity possible.	Repeat	Lyubarsky 2020
	Giant Pulse	Pulsar pulse	None	– Non-cosmological.	Repeat	Keane et al. 2012 Cordes & Wasserman 2016 Connor et al. 2016a
	PWN	Pulsar flare	– Possible afterglow	– Non-cosmological.	Repeat	Murase et al. 2016
	Newborn Pulsar	Schwinger mech.	None	– Unlikely to repeat.	One-off	Lieu 2017
Neutron Stars and Other Compact Objects	BNS Merger	Mag. braking	– GWs – sGRB – Multi-freq. afterglow – kilonova	– Subpopulation.	One-off	Totani 2013
	BNS Inspiral	Mag. reconnect./ Mag. fluct.	Same as above	– Subpopulation. – A few bursts possible.	One-off/ Repeat	Wang et al. 2016 Dokuchaev & Eroshenko 2017
	BNS Combing	Mag. reconnect.	None	– Activity windows.	Repeat	Ioka & Zhang 2020
	BNS System	Mag. reconnect.	None	– Periodic. – Burst rate to increase. – DM roughly constant. – RM and angle constant.	Repeat	Zhang 2020
	NS & Asteroids	e^- stripping	– X-rays (Galactic)	– Periodic.	Repeat/ One-off	Geng & Huang 2015 Dai et al. 2016; Dai 2020
	Pulsar Wind & Asteroids	Not specified	None	– Periodic. – Work in progress.	Repeat/ One-off	Mottez et al. 2020
	NS–WD	Mag. reconnect.	– Type Ia NS – Possibly afterglow	– Subpopulation.	One-off	Liu 2018
	NS–WD System	Mag. reconnect.	None	– Duty cycle 10 min–2 days.	Repeat	Gu et al. 2016, 2020
	NS–BH Inspiral	Poynting flux	– GWs – X- and/or γ-rays	– subpopulation. – Precursor and postcursor.	One-off	Mingarelli et al. 2015
	NS Spun-up	Magnetar flare	– GWs	– subpopulation.	One-off	Bhattacharyya 2017
	NS–PBH	Mag. reconnect.	– GWs	– Non-periodic.	Repeat/ One-off	Abramowicz et al. 2018
	NS & SN	Mag. reconnect.	– Type II SN	– Subpopulation.	One-off	Egorov & Postnov 2009
	WD–WD	Mag. reconnect.	– Type Ia SN – Possibly X-rays	– Subpopulation.	One-off	Kashiyama et al. 2013
	WD–BH	Mag. reconnect.	– X-rays	– 2–3 FRBs possible.	One-off	Li et al. 2018
	BH–BH Inspiral	Mag. reconnect.	– sGRB	– Subpopulation.	One-off	Zhang 2016
	BH–BH Discharge	Mag. reconnect.	– Radio afterglow – γ-ray afterglow	– Subpopulation.	One-off	Liu et al. 2016
AGN	AGN Combing	Mag. reconnect.	– Persistent radio	– No periodicity. – Constant DM. – RM & angle vary.	Repeat	Zhang 2018
	AGN & Cavitons	Bremsstr.	– Persistent radio	– No periodicity.	Repeat	Romero et al. 2016
	AGN & KBH	Maser	– Persistent radio – Possible GRB	– No periodicity.	Repeat	Gupta & Saini 2018
	AGN & SS	e^- oscillation	– Persistent radio	– No periodicity.	Repeat	Gupta & Saini 2018

Table 2.1: Progenitor Theories: SNR, Neutron Stars, Other Compact Bodies and AGN.

	Progenitor	Mechanism	Counterparts	Constraints/Notes	Type	References
Other	NS Collapse	Mag. reconnect.	– GWs	– SN may precede FRB.	One-off	Falcke & Rezzolla 2014
	Dicke's Superradiance	Spontaneous emission	– From triggering event	– Periodic if associated with pulsar.	Repeat/ One-off	Houde et al. 2018a Houde et al. 2018b
	Pulsar Lightning	Electrostatic	None	– No periodicity.	Repeat	Katz 2017b
	AGN-like Beam	AGN-like jet	– Persistent radio – X-ray/UV	– No periodicity. – Intrinsic duration <1 ms.	Repeat	Katz 2017c
	Pulsar Beam	Pulsar jet	None	– Periodicity.	Repeat	Katz 2017a
	SS Crust	Mag. reconnect.	None	– Subpopulation.	One-off	Zhang et al. 2018a
	QN β-decay	β-decay	– GWs	– Intrinsic burst width is seconds.	One-off	Shand et al. 2016
	QN Beam	Instabilities	– GWs	– Possible apparent periodicity. – Time delay of 12–24 days.	Repeat	Ouyed et al. 2020a
	QN & PWN	Instabilities	– GWs	– Parent NS years to decades old.	One-off	Ouyed et al. 2020b
	Axion Star & NS	Primakoff effect	None	– No periodicity.	Repeat/ One-off	Iwazaki 2014, 2015 Buckley et al. 2020
	AQN & NS	Mag. reconnect.	– Possibly mm/IR	– No periodicity.	Repeat	Van Waerbeke & Zhitnitsky 2019
	Axion Minicluster	Maser	– GW burst	– Subpopulation.	One-off	Tkachev 2015
	Axion Star & BH	e^- oscillation	None	– No periodicity.	Repeat	Tkachev 2015
	Neutral Cosmic Strings	Cusp decay	– Optical flash	– Repetition unlikely. – No periodicity.	Repeat/ One-off	Brandenberger et al. 2017
	Superconducting Cosmic Strings	Electromagnetic induction	– GWs – Possibly neutrinos	– Linear polarisation. – Emission from cusps not expected in galaxies.	One-off	Vachaspati 2008 Cai et al. 2012a,b Ye et al. 2017
	Superstrings	Axion decay	– Coincident GW	– Small number of periodic FRBs.	Repeat	Chernoff et al. 2020
	Dipole Collisions	Shock related	– High freq. radio	– Repeat from AGNs, high RMs. – One-off from dark matter halos.	Repeat/ One-off	Thompson 2017a,b
	White Holes	BH bounce	– TeV γ-rays	– Highly speculative.	One-off	Barrau et al. 2014
	RDM Stars	Laser	None	– Highly speculative. – No periodicity.	Repeat/ One-off	Nikitin 2018
	Communication	Transmitter	None	– Highly speculative.	Repeat	Luan & Goldreich 2014
	Alien Light Sails	Transmitter	None	– Highly speculative. – Occur within MW every ∼300 yrs.	Repeat	Lingam & Loeb 2017

Table 2.2: Progenitor Theories: Other

CHAPTER 3

The Milky Way Halo: FRBs and Density Estimation

3.1 Introduction

Rapid advancements in technology and a multitude of multi-wavelength surveys have provided the potential to map the baryonic mass density of the Universe (Fukugita et al., 1998; Prochaska & Tumlinson, 2009; Prochaska & Zheng, 2019). Measurements of light element ratios (Burles & Tytler, 1996; O'Meara et al., 2001; Cooke et al., 2018) and observations of the cosmic microwave background (CMB; Spergel et al., 2007; Planck Collaboration et al., 2016) provide a snapshot of the Universe at very early times. These observations provide tight constraints on the baryon mass fraction of the Universe, $f_b = \Omega_b/\Omega_m = 0.175 \pm 0.012$. Since this ratio is independent of the Hubble constant, it aids in probing the baryonic distribution of the Universe through time and space. Until recently, there has been a discrepancy between measurements of the baryonic content of the Universe at early times and observations today. The apparent deficit, known as the "missing baryon problem," was undeniably resolved when the DMs of FRBs were harnessed to directly measure the current baryonic content of the Universe (Macquart et al., 2020). The ability of FRBs to reveal otherwise dark baryons has valuable applications in galaxy studies (also see Prochaska et al., 2019), and forms the crux of this chapter.

In the early Universe ($z \sim 3$), the majority of baryons resided in a cool ($T \sim 10^4$ K), diffuse ($n \sim 10^{-5}\,\mathrm{cm}^{-3}$) plasma. These baryons are predicted to have collapsed into sheet-like and filamentary structures that make up the IGM. These give rise to the HI Lyman-α forest—a collection of absorption lines that are observed in the spectra of quasi-stellar objects (QSOs; Miralda-Escudé et al., 1996; Rauch, 1998). Around the time of structure formation, baryons are pulled by gravitationally-dominant dark matter as the dark matter collapses into halos. As the gas falls inwards, it is shock-heated to form a hot, diffuse gas, known as circumgalactic medium (CGM; e.g. White & Rees, 1978). $\sim$10% of the gas cools and falls into the center of the halo to form stars and the ISM. Comparing the baryonic mass fraction of galactic halos (M_b/M_{halo}) to the cosmic mean (Ω_b/Ω_m), however, reveals a baryonic deficit (Dai et al., 2010). The missing baryons may have been ejected back into the IGM before forming stars (Prochaska et al., 2011; Booth et al., 2012), or perhaps they simply have yet to be detected. In the latter case, the CGM presents itself as a possible refuge for illusive baryons.

The CGM is a massive, extended reservoir (Chen et al., 2001; Werk et al., 2014; Lehner et al., 2015) of metal-enriched and multiphase gas (Werk et al., 2013; Lehner et al., 2014; Liang & Chen, 2014; Prochaska et al., 2017) that pervades the dark matter halo. It comprises cool ($T \sim 10^4$ K) and dense gas clumps embedded in a hot ($T \sim 10^6$ K), diffuse plasma (Heitsch & Putman, 2009; Stocke et al., 2013; Prochaska et al., 2017; Armillotta et al., 2017; Hani et al., 2019). It plays a key role in galaxy evolution: it provides a source of star-forming fuel, facilitates galactic feedback and recycling, and is the fundamental liaison between galactic baryons and the IGM (Putman et al., 2012; Tumlinson et al., 2017). As with the IGM, CGM can be observed in QSO spectra: when a galaxy falls along the line of sight of a QSO, it creates a set of characteristic absorption lines (e.g. Bergeron, 1986; Tripp et al., 2000; Chen et al., 2001; Prochaska et al., 2011; Tumlinson et al., 2013). The cool CGM ($< 10^5$ K) can be measured with UV absorption lines (Savage et al., 2011; Burchett et al., 2019), and the hot CGM ($> 10^6$ K) with X-ray emission (Fang et al., 2015; Nicastro et al., 2018) or Sunyaev-Zeldovich signals (Lim et al., 2018; Hill et al., 2018). Different observations and analyses, however, produce significantly different results (Anderson et al., 2013;

Planck Collaboration et al., 2013; Werk et al., 2014; Keeney et al., 2017; Lim et al., 2018), and current telescope sensitivities are insufficient to probe lower mass galaxies.

Despite its close proximity, we face the same difficulties in measuring the CGM of the MW. While it is evident stars and ISM account for $\lesssim 25\%$ of the baryonic mass available to a halo of mass $M_{\rm halo} = 10^{12.2}\,{\rm M}_\odot$ (current estimate; Boylan-Kolchin et al., 2013), the mass and distribution of the Galactic halo have yet to be well determined. Constraining the Galactic CGM is primarily done using: soft X-ray emission from plasma (Henley et al., 2010); X-ray and UV absorption of lines of oxygen ions (Faerman et al., 2017); density constraints from ram-pressure stripping of the Large Magellanic Cloud (LMC; Salem et al., 2015); and the DM of pulsars in the line-of-sight of the LMC (Manchester et al., 2006). While these techniques have provided valuable information on Galatic halo models, constraints on the mass and spatial extent of the gas have large variations (Fang et al., 2013; Bregman et al., 2018; Faerman et al., 2017; Prochaska & Zheng, 2019).

While the diffusivity of the Galactic CGM disallows direct imaging, the DM of pulsars and FRBs can be used to directly probe its density. Further, the apparent isotropy of FRBs in the sky provides the potential to search for asymmetries in the halo. A current challenge, however, lies in the lack of FRB data (∼100 FRBs at the time of writing Platts et al., 2020). While this is expected to substantially increase in the coming years, we must in the meanwhile rely on techniques well-suited to the small data regime. Further, the complexity of modelling the (largely unknown) FRB dynamics (i.e. behaviour and nature) bodes a non-parametric approach. As such, we consider two probability density techniques, namely: Density Estimation using Field Theory (DEFT; Kinney, 2014; Chen et al., 2018) and kernel density estimation (KDE).[1] DEFT proves to be insufficient, and is presented for completeness. Both standard and asymmetric, variable-bandwidth KDE are considered. The former proves to be appropriate for the pulsar component of the analysis and the latter for the FRB component.

The final results are constraints on the DM of the MW halo from the pulsar and FRB analyses. Because pulsars are Galactic (i.e. the signals only pass through a fraction of the MW halo at most), the former is a lower limit. FRBs pass through the entire halo, and thus provide an upper limit. With 1σ confidence, we measure a MW halo of ${\rm DM} = 63^{+27}_{-21}\,({\rm stat}) \pm 9\,({\rm sys})\,{\rm pc\,cm^{-3}}$, where the uncertainties given in brackets are statistical and systematic, respectively.

Chapter 3 is laid out as follows: §3.2 presents the problem framework and comprises three subsections. §3.2.1 explains how DM measurements provide constraints on the intervening matter, §3.2.2 provides a discussion on algorithms adopted for modelling the DM of the ISM, and §3.2.3 details the problem approach and strategy. §3.3 provides the theory behind statistical models used in the analysis: §3.3.1 discusses DEFT; and §3.3.2 discusses KDE—standard and asymmetric, variable bandwidth. §3.4 presents the analysis and results. §3.4.2 relates to the observed pulsar and FRB samples, and §3.4.3 uses simulations to assess the model. §3.5 provides a discussion of the findings, and §3.6 concludes the chapter.

3.2 Framework

Here we set up the problem, derive constraints, and detail the electron density models used in the analysis.

3.2.1 Deriving Constraints

Recall the dispersion measure (DM) observed in pulsar and FRB signals,

$$\mathrm{DM} = \int_0^s \frac{n_e(z)}{1+z}\mathrm{d}s \ , \tag{3.2.1}$$

with which one can calculate the distribution of baryons along the line-of-sight to the source. Since FRBs are extragalactic, they pass through the full halo of the MW, whose signature is then imprinted in the FRB DMs. Pulsars, on the other hand, are local to the Galaxy[2] and may

[1] Generalised extreme value (GEV) theorem was also considered by a collaborator and was found to be insufficient.
[2] We excluded pulsars within the Magellanic clouds from our analysis.

only pass through a fraction of the MW halo. In fact, galactic halos are generally assumed to lack radio transients (but see Rajwade et al., 2018); the majority of detected pulsars live in the Galactic disk or globular clusters, and have a scale-height of 100 pc (Faucher-Giguère & Kaspi, 2006). By considering the excess DM—DM which cannot be attributed to the ISM—one can place constraints on the DM of the halo: the minimum excess DM of FRBs provides an upper limit and the maximum DM excess from pulsars provides a lower limit. A summary of the notation used is provided in Table 3.1.

Quantity	Description
$\mathrm{DM_{pulsar}}$	The total DM measurement of a pulsar
$\mathrm{DM_{FRB}}$	The total DM measurement of an FRB
$\Delta\mathrm{DM_{pulsar}}$	The DM of a pulsar corrected for by the ISM
$\Delta\mathrm{DM_{FRB}}$	The DM of an FRB corrected for by the ISM
$\mathrm{DM_{ISM}}$	Total sightline DM for the Galactic ISM
$\mathrm{DM^{\delta}_{ISM}}$	DM from a fraction of the Galactic ISM
$\mathrm{DM_{MW,halo}}$	DM of all gas in our Galactic halo
$\mathrm{DM^{\delta}_{MW,halo}}$	DM from a fraction of gas in our Galactic halo
$\mathrm{DM_{IGM}}$	DM from the IGM
$\mathrm{DM_{cosmic}}$	DM from IGM & intervening galaxies
$\mathrm{DM_{host}}$	DM from FRB host galaxy

Table 3.1: Summary of notation used in Chapter 3.

3.2.1.1 *Pulsar Constraints*

The DM of pulsars can be described by:

$$\mathrm{DM_{pulsar}} = \mathrm{DM^{\delta}_{ISM}} + \mathrm{DM^{\delta}_{MW,halo}} \quad , \tag{3.2.2}$$

where δ denotes that the contribution is a fraction of the total DM out to the edge of the Galaxy. Correcting for the DM of the ISM, the DM excess is given by:

$$\Delta\mathrm{DM_{pulsar}} = \mathrm{DM_{pulsar}} - \mathrm{DM_{ISM}} \quad . \tag{3.2.3}$$

Since pulsars tend to lie within the Galactic disk, $\mathrm{DM_{ISM}}$ is often greater than $\mathrm{DM_{pulsar}}$, and $\Delta\mathrm{DM_{pulsar}}$ is generally negative. Any positive $\Delta\mathrm{DM_{pulsar}}$ may be attributed to the MW halo. As such, we obtain a lower limit of:

$$\boxed{\mathrm{DM_{MW,halo}} > \max\left[\Delta\mathrm{DM_{pulsar}}\right] \quad .} \tag{3.2.4}$$

3.2.1.2 *FRB Constraints*

Similarly, the DM of FRBs can be described by:

$$\mathrm{DM_{FRB}} = \mathrm{DM_{ISM}} + \mathrm{DM_{MW,halo}} + \mathrm{DM_{cosmic}} + \mathrm{DM_{host}} \quad , \tag{3.2.5}$$

where $\mathrm{DM_{cosmic}}$ is the contribution from the IGM and intervening galaxies, and $\mathrm{DM_{host}}$ is the contribution from the FRB host galaxy. Correcting for the ISM, the DM excess is given by:

$$\Delta\mathrm{DM_{FRB}} = \mathrm{DM_{FRB}} - \mathrm{DM_{ISM}} \quad . \tag{3.2.6}$$

Since we will be considering the minimum of $\Delta\mathrm{DM_{FRB}}$, we take $\mathrm{DM_{cosmic}}$ to be negligible, i.e. the closest FRBs are expected to have small cosmic DM components. For example, out to $z = 0.03$ (the redshift of the closest extragalactic FRB to date, FRB 180916.J0158+65; Marcote et al., 2020), the average contribution from cosmic gas is calculated to be $\langle\mathrm{DM_{cosmic}}\rangle = 25\,\mathrm{pc\,cm^{-3}}$ using the Macquart DM–z relation (Macquart & Ekers, 2018). As such,

$$\mathrm{DM_{MW,halo}} + \mathrm{DM^{min}_{host}} = \min\left[\Delta\mathrm{DM_{FRB}}\right] \quad . \tag{3.2.7}$$

The upper limit of the MW halo DM is therefore given by:

$$\boxed{\mathrm{DM_{MW,halo}} < \min\left[\Delta\mathrm{DM_{FRB}}\right] \quad .} \tag{3.2.8}$$

The contribution from host galaxies is unknown, but is expected to vary significantly given the wide variety of hosts observed to date. While the median value is expected to be $\mathrm{DM_{host}} \sim 120\,\mathrm{pc\,cm^{-3}}$ (Niino, 2020), dwarf and elliptical galaxies may have $\mathrm{DM_{host}} \sim 45\,\mathrm{pc\,cm^{-3}}$ and $\mathrm{DM_{host}} \sim 37\,\mathrm{pc\,cm^{-3}}$, respectively (Xu & Han, 2015; Mahony et al., 2018). Should an FRB reside in the outskirts of a galaxy, this value may be lower still. As such, we take $\mathrm{DM_{host}^{min}}$ to be 10 to several tens $\mathrm{pc\,cm^{-3}}$. The value of $\mathrm{DM_{MW,halo}}$ is expected to vary depending on the line-of-sight. Galaxy formation models tend to predict an approximately symmetric distribution of gas in the halo with variations of about $\lesssim 10\,\mathrm{pc\,cm^{-3}}$ (Prochaska & Zheng, 2019). We did not consider these variations in Platts et al. (2020), but once there is more data this may be feasible.

3.2.2 Electron Density Models for the ISM

We employed two models to calculate the electron density (n_e) of the MW ISM: NE2001 (Cordes & Lazio, 2002) and YMW16 (Yao et al., 2017). Both estimate the distribution of free electrons in the MW using the distance measurements and DMs of pulsars. YMW16 has the same basic structure as NE2001, but seeks to improve upon some of its short-comings—e.g. a tendency to under-predict distances for some high-latitude pulsars (Gaensler et al., 2008; Chatterjee et al., 2009) and over-predict distances for some nearby pulsars (Chatterjee et al., 2009)—by better modelling the Galactic structure. In both models, systematic uncertainties are expected to be $\lesssim 10\,\mathrm{pc\,cm^{-3}}$ for high latitudes. At lower latitudes, the structure of the MW is significantly more complicated. As such, we limited our analysis to pulsar and FRB detections at higher latitudes ($|b| > 20°$ and $|b| > 30°$). Python implementations were used for both models, available at `https://github.com/FRBs/ne2001` and `https://github.com/FRBs/pygedm` for NE2001 and YMW16, respectively.

3.2.3 Strategy

The complicated physics of FRBs motivates a non-parametric approach, while the limited sample size calls for statistical methods that generalise well to the small data regime. We hence decided to explore the ability of density estimation techniques to attain the constraints derived in §3.2.1. This approach, however, came loaded with a qualitative problem: which point corresponds to the maximum or minimum of a PDF? The quantity is ill-defined—a PDF decays to zero on both sides. One can choose a cut-off value—for example, one could take the maximum to be the 95^{th} percentile—but such a choice is largely arbitrary. Instead, we developed a metric based on the gradient of the PDF, which we verified via simulations. This is discussed in §3.4.1 and §3.4.4. We performed the analysis using DEFT and KDE. DEFT was considered first because it was designed specifically for small data sets (Kinney, 2014; Chen et al., 2018). Unfortunately, it was unable to provide reasonable constraints for the FRB data (§3.4.5). KDE performed well for FRB data when we allowed for a varying bandwidth and used an asymmetric kernel (§3.4.2).

3.3 Statistical Theory

Before delving into the analysis, this section provides a theoretical overview of DEFT and KDE.

3.3.1 Density Estimation Using Field Theory

As its name suggests, Density Estimation using Field Theory (DEFT; Kinney, 2015) is a method of density estimation that invokes Bayesian field theory: a statistical learning technique based on field-theoretic methods in physics (e.g. Bialek et al., 1996; Lemm, 1999; Enßlin et al., 2009). It endeavours to establish a representative PDF given a limited amount of observed data by constructing a Bayesian prior $P(Q)$ that weights each possible density $Q(x)$ according to some measure of smoothness, from which one can establish a Bayesian posterior $P(Q|\mathrm{data})$ that identifies which densities are most consistent with the data and the prior. One of DEFT's successes is that it does not require the manual identification of critical parameters nor the specification of boundary conditions—both of which are often required in other density estimation techniques, including KDE. DEFT is implemented using the Python package `SUFTware` (Statistics Using Field Theory).[3]

[3] Available at `https://suftware.readthedocs.io`.

Recall: Bayes' theorem describes the probability of an event based on knowledge of conditions that may be relevant to the event. Mathematically, it is stated as:

$$P(A|B) = \frac{P(B|A)\,P(A)}{P(B)} \quad , \tag{3.3.1}$$

where $P(A|B)$ is the posterior probability, $P(A)$ is the prior probability, $P(B|A)$ is the likelihood, and $P(B)$ is the evidence.

Consider n data points $(x_1, x_2, ..., x_n)$ drawn from a known probability distribution $Q_{\rm true}(x)$ with x intervals of length L. We aim to calculate the best estimate $Q^*(x)$ of the true distribution and an ensemble of other plausible estimates from which we can establish an uncertainty. Now consider a candidate density $Q(x)$ that is parameterised by a real scalar field $\phi(x)$. To ensure $Q(x)$ is positive and normalised, one can set:

$$Q(x) = \frac{e^{-\phi(x)}}{\int e^{-\phi(x')}\mathrm{d}x'} \quad . \tag{3.3.2}$$

A field-theoretic prior $P(\phi|\ell)$ on ϕ is constructed such that it favours smooth probability densities. Specifically, Kinney (2015) consider priors of the form

$$P(\phi|\ell) = \frac{e^{-S^0_\ell[\phi]}}{Z^0_\ell} \quad , \tag{3.3.3}$$

where $S^0_\ell[\phi]$ is a "prior action" that constrains the field ϕ and Z^0_ℓ is a partition function that normalises the expression (for an interesting discussion on the relationship between thermodynamics and statistical inference, see LaMont & Wiggins, 2019). The prior action is given by:

$$S^0_\ell[\phi] = \int \frac{\ell^{2\alpha}}{2}\left(\partial^\alpha\phi\right)^2 \frac{\mathrm{d}x}{L} \quad , \tag{3.3.4}$$

where ℓ gives the length scale below which ϕ fluctuations are strongly damped and $\alpha = [1, 2, 3, 4]$ determines the smoothness. The partition function is given by:

$$Z^0_\ell = \int \mathcal{D}\phi e^{-S^0_\ell[\phi]} \quad , \tag{3.3.5}$$

where $\mathcal{D}\phi$ denotes integration over all paths ϕ. The resultant posterior (derived in Kinney, 2015) is given by

$$P(\phi|\mathrm{data}, \ell) = \frac{e^{-S_\ell[\phi]}}{Z_\ell} \quad . \tag{3.3.6}$$

The nonlinear action is given by:

$$S_\ell[\phi] = \int \left\{\frac{\ell^2\alpha}{2}\left(\partial^\alpha\phi\right)^2 + nLR\phi + ne^{-\phi}\right\}\frac{\mathrm{d}x}{L} \quad , \tag{3.3.7}$$

where $R(x) = \frac{1}{n}\sum_{i=1}^{n}\partial(x - x_i)$ is a histogram that summarises the data (with a bin width of zero). The partition function is given by:

$$Z_\ell = \int \mathcal{D}\phi e^{-S_\ell[\phi]} \quad . \tag{3.3.8}$$

Finally, in terms of the density Q, one has:

$$P(Q|\mathrm{data}, \ell) = \int_{-\infty}^{\infty} P(\phi|\mathrm{data}, \ell)\mathrm{d}\phi_{\rm c} \quad , \tag{3.3.9}$$

Here, $\phi(x) = \phi_{\rm nc}(x) + \phi_{\rm c}$, where $\phi(x)$ is composed of a constant Fourier component $\phi_{\rm c}$ and a non-constant Fourier component $\phi_{\rm nc}(x)$.

To solve this, one must minimise the action $S_\ell[\phi]$. This occurs at the maximum *a posteriori* (MAP) field ϕ_ℓ, which is given by the mode of the posterior distribution. Since $S_\ell[\phi]$ is a strictly convex

function, one can obtain a unique minimum without the need for boundary conditions on ϕ. In order to find the optimal length scale ℓ^*, the Bayesian evidence $P(\text{data}|\ell)$ is maximised. The best approximation is thus given by $Q^* = Q_{\ell^*}$. Detailed calculations and derivations are given in the supplemental material of Chen et al. (2018).

In order to obtain the uncertainty of Q^*, one must sample from the Bayesian posterior,

$$P(Q|\text{data}) = \int P(\ell|\text{data})P(Q|\text{data},\ell)\text{d}\ell \ . \tag{3.3.10}$$

This is done by first drawing ℓ from $P(\ell|\text{data})$ and then drawing Q from $P(Q|\text{data},\ell)$. Laplace approximation is used to estimate $P(Q|\text{data},\ell)$. As such, $P(Q|\text{data},\ell)$ is approximated by a Gaussian centered at the posterior's MAP value. The Laplace posterior is given by:

$$P_{\text{Lap}}(Q|\text{data}) = \int P(\ell|\text{data})P_{\text{Lap}}(Q|\text{data},\ell)\text{d}\ell \ , \tag{3.3.11}$$

from which an ensemble of distributions Q can be sampled. Chen et al. (2018) noticed that some Qs drawn were not representative of the underlying distribution. To alleviate this issue, the authors introduced importance resampling. Here, each ϕ is given a weight,

$$w_\ell[\phi] = \exp\left(S_\ell^{\text{Lap}}[\phi] - S_\ell[\phi]\right) \ , \tag{3.3.12}$$

proportional to its probability of being drawn.

DEFT uses importance resampling with replacement, however in Platts et al. (2020) we found that this led to a strong bias in our analyses. In particular, we found that the FRB PDF was poorly approximated by the posterior. As a result, a handful of the sampled distributions were allocated very large weights and the majority were allocated very small weights (e.g. Skare et al., 2003; Gelman et al., 2014). To avoid this, we chose to retain only the most probable distributions and performed the resampling without replacement. For example, for every 1000 distributions sampled, only the 500 most likely distributions were kept for the uncertainty analysis.

3.3.2 Kernel Density Estimation

Kernel density estimation (KDE) approximates an unknown density by constructing a kernel (distribution) at each data point and summing their contributions. There are many types of KDE that are appropriate in different contexts. For our analyses, we found that the pulsar PDF was best modelled using standard KDE and the FRB PDF was best modelled using varying bandwidths and an asymmetric kernel.

3.3.2.1 *Standard KDE*

Let us start by considering an independent and identically distributed sample $\{X_i : i = 1, ..., n\}$ drawn from some unknown distribution $f(x)$. Using KDE, an estimate $\hat{f}(x)$ of this distribution is given by:

$$\hat{f}_h(x) = \frac{1}{n}\sum_{i=1}^{n} K_h\left(x - X_i\right) = \frac{1}{nh}\sum_{i=1}^{n} K\left(\frac{x - X_i}{h}\right) \ , \tag{3.3.13}$$

where K is the kernel and $h > 0$ is the bandwidth (or smoothing parameter). In standard KDE, the kernel is symmetric; for example it may be Gaussian, triangular, cosine, biweight, triweight, or Epanechnikov. The Epanechnikov kernel is the most efficient in terms of its mean squared error, but the loss in efficiency for other kernels is marginal. A Gaussian kernel, for example, is only $\sim$5% less efficient. Thus, due to its convenient mathematical properties, the Gaussian is the most common kernel choice. In our analyses, we found no discernible difference between kernels, and hence settled on a Gaussian kernel for the pulsar PDF. The bandwidth is a trade-off between the bias of the estimator and its variance. If the bandwidth is too small, the PDF will be over-fitted; if it is too large, the PDF will be over-smoothed. If the underlying distribution is Gaussian, the bandwidth may be selected using rule-of-thumb bandwidth estimators; for example Silverman's (Silverman, 1986):

$$h = \left(\frac{4\hat{\sigma}^5}{3n}\right)^{\frac{1}{5}} \ , \tag{3.3.14}$$

where $\hat{\sigma}$ is the standard deviation of the data and n is the number of data points. In most situations, however, bandwidth selection is more complicated. One of the more popular techniques is to choose the bandwidth such that the mean integrated squared error (MISE) is minimised. Here,

$$\mathrm{MISE}(h) = \mathrm{E}\left[\int \left(\hat{f}_h(x) - f(x)\right)^2 dx\right] \quad , \tag{3.3.15}$$

and is equivalent to the expected L_2 risk function. This requires one to approximate the unknown density $f(x)$, for which there exists multiple techniques. For a review on such, see Jones et al. (1996). One can also select the optimal bandwidth via cross-validation (e.g. Horne & Garton, 2006), which is the route we opted for in Platts et al. (2020) and which is detailed below. The code is available at `https://github.com/FRBs/FRB/tree/master/frb/dm_kde`.

For our analyses, we used `scikit-learn` in Python. The `KernelDensity()` function available therein uses a nearest-neighbours approach, where the density at each point is evaluated using a number of neighbouring points assigned according to the bandwidth, as opposed to using the entire data set. This improves the efficiency of the algorithm and reduces the effects of potential outliers. To determine the optimal bandwidth, we search a range of possible bandwidths using the `GridSearchCV()` function. n-fold cross-validation is performed, where the data set is divided into n subsets. A KDE (of a given bandwidth) is generated using training data from $n-1$ subsets, and the KDE score function (Stone, 1974, 1977),[4]

$$CV(h) = -\frac{1}{n}\sum_{i=1}^{n} \log\left[\hat{f}_{h,-i}(X_i)\right] \quad , \tag{3.3.16}$$

is evaluated. This is done n times—using a different subset as the hold-out set for each iteration—and an average score is determined. The process is repeated for the remaining bandwidths. The optimal bandwidth is that which minimises the score function (for the pulsar PDF, $h \approx 10$).

3.3.2.2 *Asymmetric KDE*

Standard KDE performs well when the density of data is relatively uniform and the distribution is unbounded. As seen in §3.4.2, however, the FRB PDF is expected to be bounded on $[0, \infty)$ and has a high concentration of data towards the front of the distribution. One issue for a skew distribution with a fixed bandwidth h is the trade-off between large and small scale structure: over-dense regions are over-smoothed if h is too large and under-dense regions are overfitted if h is too small. Another issue is that in standard KDE, distributions with bounded support are subject to significant bias near their boundaries due to edge (or boundary) effects (Gasser & Müller, 1979) and are asymptotically inconsistent. This can be readily observed by considering a density function that is continuous on $x \in [0, \infty)$. For a given bandwidth h, one has the boundary interval $x \in [0, h)$ and the interior interval $x \in [h, \infty)$. Consider the expectation value for the estimators in both regions. For $x \in [h, \infty)$ and with the second order Taylor expansion of $f(x - ht)$ at x with $h \to 0$, one has:

$$\mathrm{E}\left(\hat{f}_h(x)\right) = \int_{-1}^{c} K(t) f(x - ht) \mathrm{d}t \tag{3.3.17}$$

$$\approx f(x) + \frac{h^2}{2} f''(x) \int_{-1}^{c} t^2 K(t) \mathrm{d}t + \mathcal{O}(h^4) \quad . \tag{3.3.18}$$

Now consider $x \in [0, h)$ and take $\hat{f}(ch)$ for $c \in [0, 1)$, where c is a scaling parameter. The expected value of $\hat{f}(x)$ becomes:

$$\mathrm{E}\left(\hat{f}_h(x)\right) = \int_{-1}^{c} K(t) f(x - ht) \mathrm{d}t \tag{3.3.19}$$

$$\approx f(x) \int_{-1}^{c} K(t) \mathrm{d}t - h f'(x) \int_{-1}^{c} t K(t) \mathrm{d}t \tag{3.3.20}$$

$$+ \frac{h^2}{2} f''(x) \int_{-1}^{c} t^2 K(t) \mathrm{d}t + \mathcal{O}(h^3) \quad , \tag{3.3.21}$$

[4] Note that the score function is simply a negative log likelihood function.

where $t \in [-1, 1]$ is the kernel domain. Note that the bias of the estimator,

$$\text{bias}\left(\hat{f}_h(x)\right) = \text{E}\left(\hat{f}_h(x)\right) - f(x) \quad , \tag{3.3.22}$$

is $\mathcal{O}(h)$ in the boundary interval and $\mathcal{O}(h^2)$ in the interior interval. Further, the estimator is inconsistent. At $x = 0$, the expected value cannot amount to the true value for $h \to 0$:

$$\text{E}\left(\hat{f}_h(0)\right) = \frac{1}{2} f(0) + \mathcal{O}(h) \quad . \tag{3.3.23}$$

Numerous proposals have been made over the years to resolve boundary effects, such as data reflection (Schuster, 1985), the hybrid method (Hall & Wehrly, 1991), kernels with boundaries (i.e. asymmetric kernels; Müller, 1991, 1993; Muller & Wang, 1994), generating pseudo-data (Cowling & Hall, 1996), by data binning and local polynomial fitting (Cheng et al., 1997), and many more. In Platts et al. (2020), we invoked an asymmetric gamma kernel with varying bandwidths, as proposed by Chen (2000) and expanded upon by Jeon & Kim (2013) and Hoffmann & Jones (2015).

To avoid over/under-smoothing, Terrell & Scott (1992) present two methods by which the bandwidth h can be varied: balloon estimators and sample-smoothing estimators. Balloon estimators have bandwidths that depend on the point of estimation, such that

$$\hat{f}_h(x) = \frac{1}{nh(x)} \sum_{i=1}^{n} K\left(\frac{x - X_i}{h(x)}\right) \quad , \tag{3.3.24}$$

whereas sample-smoothing estimators depend on the sample associated with each kernel,

$$\hat{f}_h(x) = \frac{1}{n} \sum_{i=1}^{n} \frac{1}{h(X_i)} K\left(\frac{x - X_i}{h(X_i)}\right) \quad . \tag{3.3.25}$$

For our analyses—following Hoffmann & Jones (2015)—we invoked the former.

The gamma kernel used is given by:

$$K_{k,\theta}(x) = \frac{x^{k-1} \exp(-\frac{x}{\theta})}{\theta^k \Gamma(k)} \quad , \tag{3.3.26}$$

where $\Gamma(\cdot)$ is the standard gamma function, k is the scale parameter and θ is the shape parameter. Chen (2000) take $k = \rho_h(x)$ and $\theta = h$ with random gamma variables X_i, such that

$$K_{\rho_h(x),h}(X_i) = \frac{X_i^{\rho_h(x)-1} \exp(-\frac{X_i}{h})}{h^{\rho_h(x)} \Gamma(\rho_h(x))} \quad , \tag{3.3.27}$$

with

$$\rho_h(x) = \begin{cases} \dfrac{x}{h}\,, & \text{if} \quad x \geq 2h \quad , \\ \left(\dfrac{x}{2h}\right)^2 + 1\,, & \text{if} \quad x \in [0, 2h) \quad . \end{cases}$$

The resultant gamma estimator is given by:

$$\hat{f}_h(x) = \frac{1}{n} \sum_{i=1}^{n} K_{\rho_h(x),h}(X_i) \quad . \tag{3.3.28}$$

The shape of the gamma estimator varies naturally, allowing for different levels of smoothness at different scales. The gamma estimator is also unlikely to allocate weight for negative values of x, since the gamma kernel itself is non-negative. As such, gamma estimators are free of boundary bias.

Another issue in standard KDE is the over-estimation of densities in sparse regions and the under-estimation of densities in dense regions. This may be overcome using shifted KDEs, where the bias is lowered by marginally shifting samples from low to high density regions (Samiuddin &

El-Sayyad, 1990). Combining shifted KDEs with balloon estimators, the final gamma estimator given by:

$$\boxed{\hat{f}_h(x) = \frac{1}{n}\sum_{i=1}^{n} K_{\rho_h(x),h(x)}\left(X_i - h^p(x)\delta(x)\right) \quad ,} \tag{3.3.29}$$

where p is the order of the kernel and $\delta(x)$ is the shift (Hoffmann & Jones, 2015).

For our analyses, we used the Python code by Hoffmann & Jones (2015),[5] where the optimal bandwidth for each kernel is selected by minimising the MISE.

3.4 Analysis

The analysis presented below focuses on KDE, which performed well for both transient samples. The DEFT analysis is presented at the end of the section (§3.4.5), where its shortfall is illustrated. The metric to determine the upper and lower bounds of the distribution is discussed in §3.4.1 and the corresponding simulations are presented in §3.4.4. §3.4.2 provides the KDE analysis for the observed transient samples, which places constraints on $\mathrm{DM_{MW,halo}}$ from $\Delta\mathrm{DM_{pulsar}}$ and $\Delta\mathrm{DM_{FRB}}$. §3.4.3 presents an analysis of the KDE methodology applied to the FRB data by simulating $\Delta\mathrm{DM_{FRB}}$. Here, random samples of size $n = 100$, 1000 and 10 000 are taken from the simulated PDF and $\min\left[\Delta\mathrm{DM_{FRB,sim}}\right]$ is compared to the known inputs. This provides a test of the methodology and gives insight into how the model may perform as more FRBs are detected.

3.4.1 Determining the Bounds of DM Distributions

As mentioned in §3.2.3, we wish to find upper and lower limits of the observed $\Delta\mathrm{DM_{pulsar}}$ and $\Delta\mathrm{DM_{FRB}}$ distributions for pulsars and FRBs, respectively. In Platts et al. (2020), we formulated a metric primarily tailored for the FRB distribution. The pulsar distribution can provide only a loose lower bound due to its incomplete MW halo information and it is limited by modelling uncertainties (§3.5). The FRB distribution, on the other hand, can be more tightly constrained as its sample size increases (and thousands of FRB detections are expected in the coming years). Based on the physical prior that the $\Delta\mathrm{DM_{FRB}}$ distribution will have a sharp cut-off, we postulated that the minimum of the distribution can be approximated by the maximum gradient of the distribution, $\max\left[f'(\Delta\mathrm{DM})\right]$. This prior is supported by current observations (see 3.4.2) and is expected to hold if the variance in $\mathrm{DM_{MW,halo}}$ is much less than the total average DM. We also experimented with simulated FRB distributions to test the performance of the metric. This is presented in §3.4.4. For the distribution of $\Delta\mathrm{DM_{pulsar}}$, we expect the metric (where the maximum of the $\Delta\mathrm{DM_{pulsar}}$ distribution is now approximated by the minimum gradient of the distribution, $\min\left[f'(\Delta\mathrm{DM})\right]$) to be more conservative because of the smooth tail and even distribution of data. This is verified by simulation (§3.4.4).

3.4.2 Observed Transient Samples

The sample of pulsars and FRBs was taken from the largest aggregation sites for each type of object: the Australia Telescope National Facility (ATNF) pulsar catalogue[6] (version 1.61; Manchester et al., 2005) and the FRBCAT[7] (downloaded 25 February 2020, verified events only; Petroff et al., 2016). Note, however, that the electron distribution is significantly more complicated at lower Galactic latitudes due to the spiral arms, HII regions and SNRs. Measurements from electron density models are therefore far more uncertain for lower latitudes. In particular, the models are most complex on scales smaller than 200 pc and within 1 kpc of the Sun (Cordes & Lazio, 2003). As such, transients that lie more than $200/1000 \approx 20°$ from the Galactic plane are considered in the analysis. All transients within 5° of the Magellanic clouds are also removed to further minimise systematic uncertainty. The final samples consisted of: 371 pulsars and 83 FRBs for a latitude limit of $|b| > 20°$; and 215 pulsars and 64 FRBs for a latitude limit of $|b| > 30°$. For $|b| > 30°$, there is a significant decrease in FRB data. As such, the final results use a Galactic latitude cut of $|b| > 20°$. Even with these restrictions, the systematic uncertainties associated with the electron

[5] Available at https://github.com/tillahoffmann/asymmetric_kde.
[6] Available at https://www.atnf.csiro.au/research/pulsar/psrcat.
[7] Available at http://frbcat.org.

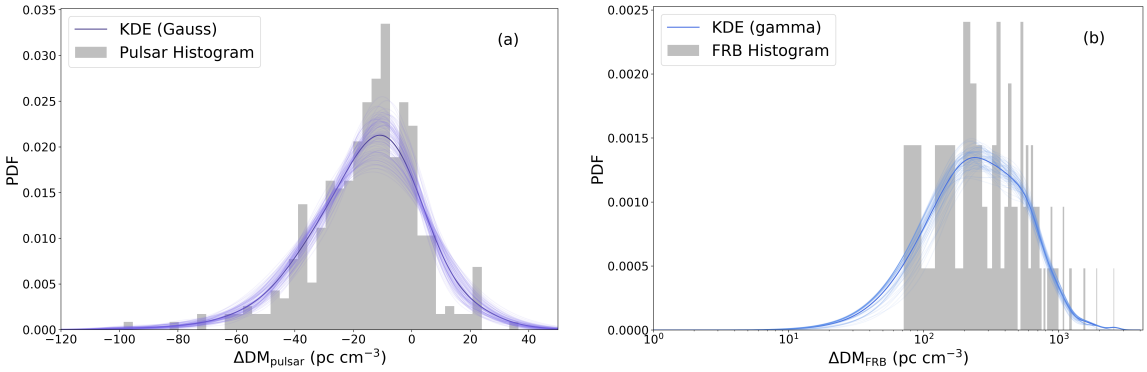

Figure 3.1: Distributions of the observed transient samples for $|b| > 20°$ with DM_{ISM} modelled using YMW16. The PDFs derived with KDE are overlaid on the data. (a) ΔDM_{pulsar} KDEs (with Gaussian kernels and fixed bandwidths). The dark purple curve shows the PDF estimated with the original data and the lighter curves show the PDFs generated with resampled data. The bandwidth for each distribution is selected via cross-correlation with a search range of $h = [8, 15]\,\mathrm{pc\,cm^{-3}}$. (b) ΔDM_{FRB} KDEs (with gamma kernels and variable bandwidths). The dark blue curve shows the PDF estimated using the original data and the lighter curves show the PDFs generated with resampled data.

density models may be as high as tens of percent at high latitudes (Schnitzeler, 2012). As such, we use both NE2001 (Cordes & Lazio, 2002) and YMW16 (Yao et al., 2017) electron density models when calculating DM_{ISM}. This provides a means to estimate the systematic uncertainty in our analyses.

	Latitude	$\max[\Delta DM_{pulsar}]$	$DM_{MW,halo}$
NE2001	$\lvert b\rvert > 20°$	$-2 \pm 2\,(\mathrm{stat}) \pm 9\,(\mathrm{sys})\,\mathrm{pc\,cm^{-3}}$	$> -11\,\mathrm{pc\,cm^{-3}}$
	$\lvert b\rvert > 30°$	$-4 \pm 3\,(\mathrm{stat}) \pm 8\,(\mathrm{sys})\,\mathrm{pc\,cm^{-3}}$	$> -13\,\mathrm{pc\,cm^{-3}}$
YMW16	$\lvert b\rvert > 20°$	$7 \pm 2\,(\mathrm{stat}) \pm 9\,(\mathrm{sys})\,\mathrm{pc\,cm^{-3}}$	$> -2\,\mathrm{pc\,cm^{-3}}$
	$\lvert b\rvert > 30°$	$4 \pm 2\,(\mathrm{stat}) \pm 8\,(\mathrm{sys})\,\mathrm{pc\,cm^{-3}}$	$> -5\,\mathrm{pc\,cm^{-3}}$

(a)

	Latitude	$\min[\Delta DM_{FRB}]$	$DM_{MW,halo}$
NE2001	$\lvert b\rvert > 20°$	$54^{+40}_{-19}\,(\mathrm{stat}) \pm 9\,(\mathrm{sys})\,\mathrm{pc\,cm^{-3}}$	$< 127\,\mathrm{pc\,cm^{-3}}$
	$\lvert b\rvert > 30°$	$45^{+39}_{-9}\,(\mathrm{stat}) \pm 7\,(\mathrm{sys})\,\mathrm{pc\,cm^{-3}}$	$< 110\,\mathrm{pc\,cm^{-3}}$
YMW16	$\lvert b\rvert > 20°$	$63^{+27}_{-21}\,(\mathrm{stat}) \pm 9\,(\mathrm{sys})\,\mathrm{pc\,cm^{-3}}$	$< 123\,\mathrm{pc\,cm^{-3}}$
	$\lvert b\rvert > 30°$	$52^{+37}_{-11}\,(\mathrm{stat}) \pm 7\,(\mathrm{sys})\,\mathrm{pc\,cm^{-3}}$	$< 113\,\mathrm{pc\,cm^{-3}}$

(b)

Table 3.2: Constraints from Platts et al. (2020) derived from (a) pulsar and (b) FRB observations. NE2001 and YMW16 are used to model DM_{ISM} with $|b| > 20°$ and $|b| > 30°$. $\max[\Delta DM_{pulsar}]$ and $\min[\Delta DM_{FRB}]$ are calculated at 1σ, and upper and lower limits for $DM_{MW,halo}$ at 95% c.l.. Systematic errors are taken to be the difference between NE2001 and YMW16 estimates. ΔDM_{pulsar} is modeled with KDE using Gaussian kernels and fixed bandwidths, and ΔDM_{FRB} is modeled with KDE using gamma kernels and varying bandwidths.

The histograms of ΔDM_{pulsar} and ΔDM_{FRB} are generated according to Equations 3.2.3 and 3.2.6 by subtracting DM_{ISM}, and are shown in Figures 3.1a and 3.1b. ΔDM_{pulsar} is predominantly negative with a small positive tail. ΔDM_{FRB} is shown on a log scale and is exclusively positive with a minimum value of $\Delta DM_{FRB} \approx 64\,\mathrm{pc\,cm^{-3}}$. KDE with Gaussian kernels and a fixed bandwidth of $h \approx 10$ was used to model the pulsar DM distribution, shown by the dark purple curve in Figure 3.1a. The pulsar data was resampled 1000 times (with replacement), from which an ensemble of KDEs was derived (light purple curves, 100 shown). KDE with gamma kernels and a varying bandwidth was used on the FRB data set to derive the dark blue curve in Figure 3.1b. KDEs were generated for 1000 resampled data sets, of which 100 are shown. The upper and lower

bounds of $\Delta\mathrm{DM}_{\mathrm{pulsar}}$ and $\Delta\mathrm{DM}_{\mathrm{FRB}}$ are shown in Table 3.2 using both electron density models and latitude cuts. The statistical uncertainties are derived by taking the 1σ limit of the ensemble of $\max[\Delta\mathrm{DM}_{\mathrm{pulsar}}]$ and $\min[\Delta\mathrm{DM}_{\mathrm{FRB}}]$ values. The systematic uncertainties are given by the difference between NE2001 and YMW16 estimates. $\mathrm{DM}_{\mathrm{MW,halo}}$ is estimated with a confidence level (c.l.) of 95%. The uncertainties for the distributions are insensitive to the Galactic latitude limit. The uncertainty of the $\Delta\mathrm{DM}_{\mathrm{pulsar}}$ distribution is dominated by the systematic error, whereas the uncertainty of $\Delta\mathrm{DM}_{\mathrm{FRB}}$ is dominated by the statistical error. As the sample size increases, the statistical error is expected to decrease. The YMW16 model predicts smaller $\mathrm{DM}_{\mathrm{ISM}}$ values than NE2001, and thus YMW16 gives larger estimates of $\max[\Delta\mathrm{DM}_{\mathrm{pulsar}}]$ and $\min[\Delta\mathrm{DM}_{\mathrm{FRB}}]$. Since we expect the lower limit of $\mathrm{DM}_{\mathrm{MW,halo}}$ to be positive, we choose YMW16 for the final results ($\mathrm{DM}_{\mathrm{MW,halo}} > -2$ with YWM16 versus $\mathrm{DM}_{\mathrm{MW,halo}} > -11$ with NE2001). There is a notable difference in estimates for the FRB sample using different Galactic latitude cuts. The difference in results for pulsars using difference latitude limits, however, is negligible. This suggests the effect is due to sample size: the FRB sample decreases from 83 to 64 as the latitude limit is increased from $|b| > 20°$ to $|b| > 30°$. The $> 20\%$ loss of FRB data motivated a $|b| > 20°$ cut for the final results.

3.4.3 Simulated FRB Sample

To predict how the estimation of $\min[\Delta\mathrm{DM}_{\mathrm{FRB}}]$ may improve as the FRB sample size increases and to verify the metric chosen to approximate $\min[\Delta\mathrm{DM}_{\mathrm{FRB}}]$, we simulated $\Delta\mathrm{DM}_{\mathrm{FRB}}$.[8] From Equation 3.2.5,

$$\Delta\mathrm{DM}_{\mathrm{FRB}} = \mathrm{DM}_{\mathrm{MW,halo}} + \mathrm{DM}_{\mathrm{cosmic}} + \mathrm{DM}_{\mathrm{host}} \quad . \tag{3.4.1}$$

$\mathrm{DM}_{\mathrm{cosmic}}$ and $\mathrm{DM}_{\mathrm{host}}$, in principle, have minimum values of of zero, and $\mathrm{DM}_{\mathrm{MW,halo}}$ has a positive minimum. $\mathrm{DM}_{\mathrm{MW,halo}}$ thus provides a zero-point offset (or absolute minimum) for $\Delta\mathrm{DM}_{\mathrm{FRB}}$, i.e. $\min[\Delta\mathrm{DM}_{\mathrm{FRB}}] > 0$. In Platts et al. (2020), we chose to model $\mathrm{DM}_{\mathrm{MW,halo}}$ with a delta function at 30 $\mathrm{pc\,cm^{-3}}$ and $\mathrm{DM}_{\mathrm{host}}$ with a log-normal distribution with a mean of $\mu = 40$ $\mathrm{pc\,cm^{-3}}$ and a standard deviation of $\sigma = 0.5$. The choice of $\mathrm{DM}_{\mathrm{MW,halo}}$ is motivated by its small variance. The distribution of $\mathrm{DM}_{\mathrm{host}}$ is based on the observation that galaxy size (luminosity or stellar mass) is well described by a log-normal function (Shen et al., 2003) and the assumption that FRBs occur in a broad range of galaxy types. Other possible distributions and their effects are discussed in §3.4.4.

The cosmic DM contribution was modelled using the Macquart (DM–z) relation (Macquart & Ekers, 2018):[9]

$$\langle\mathrm{DM}(z)\rangle = \frac{3H_0 c}{8\pi G m_p}\Omega_b \int_0^z \frac{(1+z)f_e(z)}{\left[(1+z)^3\Omega_m + \Omega_\Lambda\right]^{0.5}}\mathrm{d}z' \quad , \tag{3.4.2}$$

where $f_e(z) = \frac{3}{4}X_{e,\mathrm{H}}(z) + \frac{1}{8}X_{e,\mathrm{He}}(z)$ with $X_{e,\mathrm{He}}$ and $X_{e,\mathrm{He}}$ the ionisation fractions of hydrogen and helium. H_0 is the Hubble constant, m_p is the proton mass, Ω_b is the cosmic baryonic density, Ω_m is the dark matter density and Ω_Λ is the dark energy density. This requires a distribution of FRB redshifts, for which we chose to use the observed $\mathrm{DM}_{\mathrm{FRB}}$ values with a latitude cut of $|b| > 20°$ and removed $\mathrm{DM}_{\mathrm{ISM}}$ using NE2001. The distribution of FRB DMs was modelled using standard KDE with a Gaussian kernel. Random draws were taken from the PDF of the z values, which were fed back into the Macquart relation to obtain the average cosmic contribution to the DM. Deviations from the average are modelled more simply than in Macquart & Ekers (2018). We assumed a fractional standard deviation for $\langle\mathrm{DM}_{\mathrm{cosmic}}\rangle$ of $\sigma_{\mathrm{DM}}(z) = Fz^{-1/2}$ with $F = 0.2$. The final cosmic DM contribution becomes:

$$\langle\mathrm{DM}_{\mathrm{cosmic}}(z)\rangle = \langle\mathrm{DM}(z)\rangle + \langle\mathrm{DM}(z)\rangle\sigma_{\mathrm{DM}}(z)n_{\mathrm{Gauss}} \quad , \tag{3.4.3}$$

where n_{Gauss} is Gaussian noise given by random draws from a Gaussian distribution characterised by $\sigma = 1$ and truncated at $\pm 1\sigma$. Throughout, it is ensured that $\mathrm{DM}_{\mathrm{cosmic}}$ is positive. The final simulated $\Delta\mathrm{DM}_{\mathrm{FRB}}$ distribution is obtained by summing $\mathrm{DM}_{\mathrm{cosmic}}$ with $\mathrm{DM}_{\mathrm{MW,halo}}$ and $\mathrm{DM}_{\mathrm{host}}$.

Figure 3.2a shows the simulated FRB distribution, overlaid with KDE approximations made with $n = 10\,000$ draws. The absolute minimum (given by $\mathrm{DM}_{\mathrm{MW,halo}}$) is $\Delta\mathrm{DM}_{\mathrm{FRB}} = 30$ $\mathrm{pc\,cm^{-3}}$, after which the distribution rises sharply due to contributions from the host and $\mathrm{DM}_{\mathrm{cosmic}}$. The dark

[8] Available at https://github.com/FRBs/FRB/tree/master/frb/dm_kde.
[9] Available at https://github.com/FRBs/FRB.

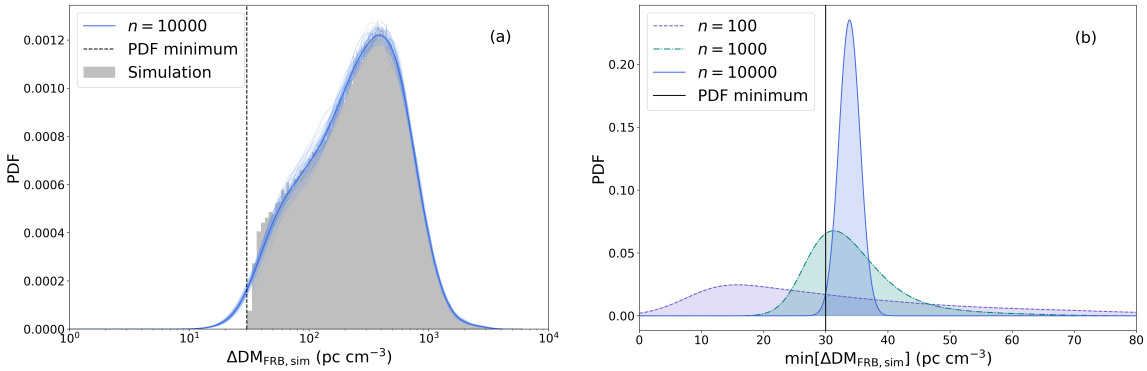

Figure 3.2: Based on Figure 3 of Platts et al. (2020). (a) Distribution of $\Delta\mathrm{DM}_{\mathrm{FRB,sim}}$ from simulated data. The KDE (gamma) estimation for $n = 10\,000$ is shown by the dark blue line. The thinner blue lines show the ensemble of KDEs from resampled data. (b) Distributions of $\min\left[\Delta\mathrm{DM}_{\mathrm{FRB,sim}}\right]$ given by the maximum gradients of the KDE (gamma) PDFs. As the sample size increases, the uncertainty decreases and the minimum value approaches $\min\left[\Delta\mathrm{DM}_{\mathrm{FRB,sim}}\right] = 34\,\mathrm{pc\,cm^{-3}}$, which is $4\,\mathrm{pc\,cm^{-3}}$ above the absolute minimum.

blue curve is modelled using the original data set and the light blue curves are modelled using resampled data (with replacement).

No. FRBs	$\min\left[\Delta\mathrm{DM}_{\mathrm{FRB}}\right]$	$\mathrm{DM}_{\mathrm{MW,halo}}$
100	$37 \pm 24\,(\mathrm{stat})\,\mathrm{pc\,cm^{-3}}$	$< 114\,\mathrm{pc\,cm^{-3}}$
1000	$35 \pm 7\,(\mathrm{stat})\,\mathrm{pc\,cm^{-3}}$	$< 55\,\mathrm{pc\,cm^{-3}}$
10000	$34 \pm 2\,(\mathrm{stat})\,\mathrm{pc\,cm^{-3}}$	$< 44\,\mathrm{pc\,cm^{-3}}$

Table 3.3: Simulation estimates for $\min\left[\Delta\mathrm{DM}_{\mathrm{FRB,sim}}\right] = 30\,\mathrm{pc\,cm^{-3}}$ from Platts et al. (2020) using sample sizes of $n = 100, 1000$ and $10\,000$. The second column gives $\min\left[\Delta\mathrm{DM}_{\mathrm{FRB}}\right]$ evaluated at 1σ and the last column gives an upper limit for $\mathrm{DM}_{\mathrm{MW,halo}}$ with a 95% c.l..

We analysed the sensitivity of the method by comparing the limits derived using sample sizes of $n = 100$, 1000 and $10\,000$ to the absolute (known) minimum. An ensemble of 1000 KDEs was produced to derive the uncertainties. The minimum value $\min\left[\mathrm{DM}_{\mathrm{FRB}}\right]$ for each PDF is given by the DM at which the slope of the PDF is maximised. The results are presented in Table 3.3 and the distribution of $\min[\Delta\mathrm{DM}_{\mathrm{FRB}}]$ values is shown in Figure 3.2b. As n increases, the central values of $\min[\Delta\mathrm{DM}_{\mathrm{FRB}}]$ approach $\approx 34\,\mathrm{pc\,cm^{-3}}$ and the spread of the PDFs decrease. Between $n = 1000$ and $n = 10\,000$, the results for the central value and its uncertainty improve. Adding more than $10\,000$ samples does not notably improve the estimate. For small n, the distribution is skewed to the left and has a significant tail out to the right. As n increases, the distribution becomes Gaussian. For $n = 100$, the uncertainty is too high to place a constraint on $\mathrm{DM}_{\mathrm{MW,halo}}$ with reasonable confidence.

3.4.4 Simulation for Bounds

To check whether the metric $\min[\Delta\mathrm{DM}_{\mathrm{FRB}}] = \max\left[f'(\Delta\mathrm{DM}_{\mathrm{FRB}})\right]$ is reasonably robust to changes in the FRB simulation—i.e. that the metric applies for a range of plausible $\Delta\mathrm{DM}_{\mathrm{FRB}}$ distributions—the analysis was repeated using different distributions of $\mathrm{DM}_{\mathrm{host}}$.[10] In general, the smoother the front of the $\Delta\mathrm{DM}_{\mathrm{FRB}}$ distribution, the more conservative the limits. For a very sharp edge at the front of the distribution, the minimum is well described by the metric. This is demonstrated with two examples that represent extreme possibilities for the $\Delta\mathrm{DM}_{\mathrm{FRB}}$ distribution: modelling $\mathrm{DM}_{\mathrm{host}}$ as a δ-function at $30\,\mathrm{pc\,cm^{-3}}$ and as a broad Gaussian distribution with $\mu = 60\,\mathrm{pc\,cm^{-3}}$ and $\sigma = 15\,\mathrm{pc\,cm^{-3}}$ (Figure 3.3a). The results are shown in Figures 3.4a and 3.4b, respectively. When $\mathrm{DM}_{\mathrm{host}}$ is a δ-function, the central values converge to $59.9 \pm 0.2\,\mathrm{pc\,cm^{-3}}$, which is in good agreement with the absolute minimum of $60\,\mathrm{pc\,cm^{-3}}$. When $\mathrm{DM}_{\mathrm{host}}$ is a broad Gaussian, the central values converge to $48.7 \pm 4.1\,\mathrm{pc\,cm^{-3}}$, which is approximately $18\,\mathrm{pc\,cm^{-3}}$ above the absolute

[10] Since $\mathrm{DM}^{\delta}_{\mathrm{ISM}}$ is expected to vary by only $\sim 10\,\mathrm{pc\,cm^{-3}}$, different plausible $\mathrm{DM}^{\delta}_{\mathrm{ISM}}$ distributions did not significantly affect the overall structure of $\Delta\mathrm{DM}_{\mathrm{FRB}}$.

minimum. We thus conclude that the metric is suitable if $\mathrm{DM_{MW,halo}} + \mathrm{DM_{host}}$ is reasonably sharp, and expect the metric to provide more conservative results for smooth distributions (this would apply to $\Delta\mathrm{DM_{pulsar}}$).

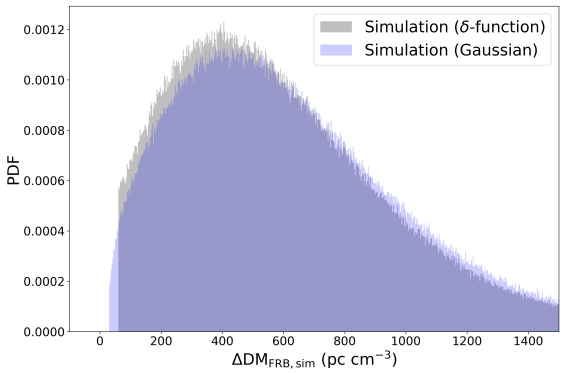

Figure 3.3: Distributions for $\Delta\mathrm{DM_{FRB}}$ with $\mathrm{DM_{host}}$ a δ-function at $30\,\mathrm{pc\,cm^{-3}}$ (grey) and a broad Gaussian distribution with $\mu = 60\,\mathrm{pc\,cm^{-3}}$ and $\sigma = 15\,\mathrm{pc\,cm^{-3}}$ (blue).

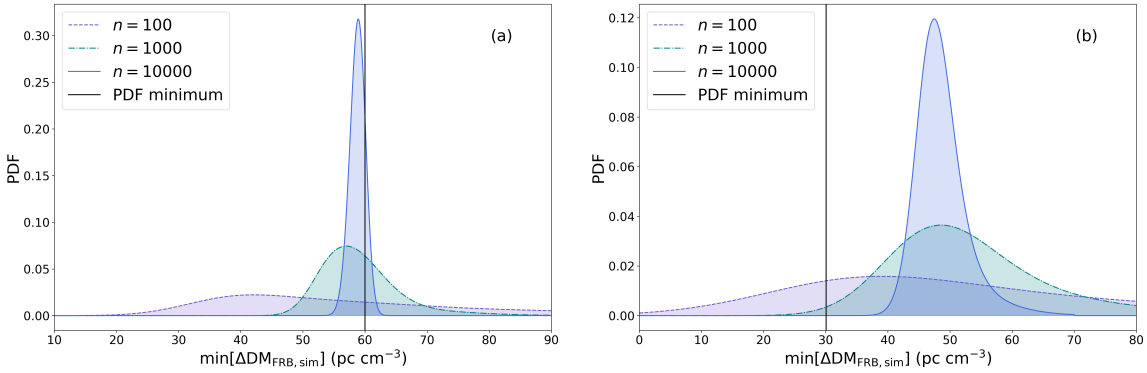

Figure 3.4: Based on Figure 5 of Platts et al. (2020). (a) $\min[\Delta\mathrm{DM_{FRB}}]$ with $\mathrm{DM_{host}}$ a delta function at 30 $\mathrm{pc\,cm^{-3}}$. The absolute minimum is 60 $\mathrm{pc\,cm^{-3}}$. (b) $\min[\Delta\mathrm{DM_{FRB}}]$ for a Gaussian $\mathrm{DM_{host}}$ with $\mu = 60\,\mathrm{pc\,cm^{-3}}$ and $\sigma = 15\,\mathrm{pc\,cm^{-3}}$. The absolute minimum is $30\,\mathrm{pc\,cm^{-3}}$.

3.4.5 DEFT Analysis

When used to model $\Delta\mathrm{DM_{pulsar}}$, DEFT gave limits on $\mathrm{DM_{MW,halo}}$ consistent with the results from standard KDE presented in §3.4.2. For $\Delta\mathrm{DM_{FRB}}$, however, DEFT failed to adequately represent the sharp leading edge of the distribution. This is shown in Figure 3.5 via simulation. Even with a sample size of $n = 10\,000$, the distribution has a tail that extends to negative (non-physical) values and misses most of the front structure of the PDF (Figure 3.5a). If we enforce a boundary at $\mathrm{DM} = 0\,\mathrm{pc\,cm^{-3}}$, we get edge effects (Figure 3.5b), where there is a significant probability of having $\mathrm{DM} = 0\,\mathrm{pc\,cm^{-3}}$ when we expect this to be small. As such, we limited our final results to KDE analyses.

3.5 Discussion

The primary result of Platts et al. (2020) is a conservative upper limit on the DM contribution of the Milky Way halo derived from FRB observations. We chose to present calculations that used the YMW16 model as the final results, one of the reasons being that YMW16 is the most up-to-date electron density model. We found that $\mathrm{DM_{MW,halo}} = 63^{+27}_{-21}\,(\mathrm{stat}) \pm 9\,(\mathrm{sys})\,\mathrm{pc\,cm^{-3}}$ ($|b| > 20°$), where the statistical uncertainty is given at 1σ. Converting this to an upper limit with a 95% c.l., we obtained $\mathrm{DM_{MW,halo}} < 123\,\mathrm{pc\,cm^{-3}}$. This includes a non-zero contribution from the IGM and intervening galaxies, which is expected to be low: the closest FRB to date is at z=0.03

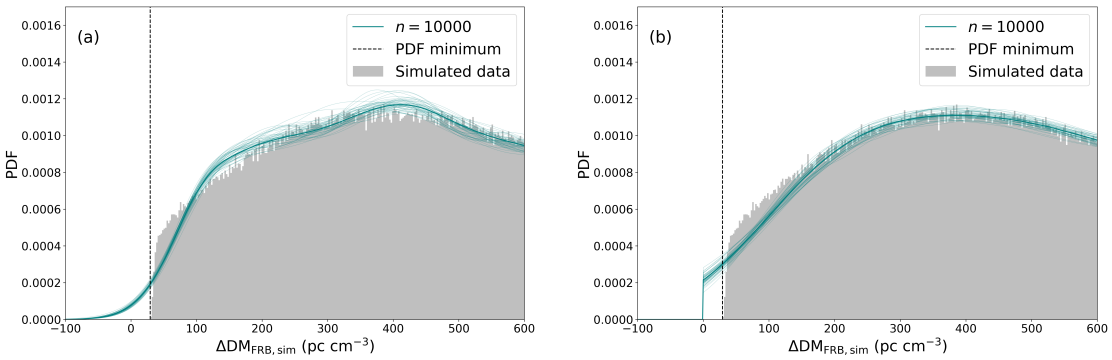

Figure 3.5: Distribution of $\Delta\mathrm{DM}_{\mathrm{FRB}}$, with a latitude limit of $|b| > 20°$ and modelling $\mathrm{DM}_{\mathrm{ISM}}$ with NE2001. (a) is unbound and (b) enforces a boundary at 0. Overlaid on the histogram are PDFs approximated with DEFT using 10 000 samples. The thick line shows the DEFT Bayesian posterior and the finer lines show the PDFs obtained by sampling the Bayesian posterior.

(Marcote et al., 2020), which translates to a DM contribution of $\mathrm{DM}_{\mathrm{cosmic}} \approx 25\,\mathrm{pc\,cm^{-3}}$ via the Macquart relation. The estimate also includes a contribution from the FRB host galaxy, which is expected to be several tens of $\mathrm{pc\,cm^{-3}}$. These considerations give a (speculative) upper limit of $\mathrm{DM}_{\mathrm{MW,halo}} \approx 50\,\mathrm{pc\,cm^{-3}}$. As more FRBs are observed, the minimum values of these contributions may decrease; for example if an FRB resides in the outskirts of its host galaxy and if an FRB is observed at a lower (extragalactic) redshift. As such, constraints may become tighter.

Two measures of uncertainty were used: systematic and statistical. The systematic uncertainty is owed to errors in estimating the electron density of the MW ISM. We derived constraints on $\mathrm{DM}_{\mathrm{MW,halo}}$ using the NE2001 and YMW16 models, and conservatively took the systematic uncertainty to be the difference between them. For both pulsars and FRBs, the systematic uncertainty was found to be approximately $\pm 8\,\mathrm{pc\,cm^{-3}}$. Another consideration was the Galactic latitude limit, where samples near the Galactic plane or Magnellanic clouds were excluded to reduce the systematic error. The difference in results for pulsars with $|b| > 20°$ and $|b| > 30°$ (with sample sizes of 371 and 215, respectively) was negligible, at about $3\,\mathrm{pc\,cm^{-3}}$. The results for FRBs differed more substantially, which we attributed to sample size: with $|b| > 30°$, there were only 64 FRBs in the sample, compared to 83 with $|b| > 20°$. As such, we chose a Galactic cut of $|b| > 20°$. The statistical errors were found using a bootstrapping technique, where the original sample was resampled (with replacement) a number of times to create an ensemble of possible distributions.

The pulsar constraints are primarily limited by systematic uncertainties. The results using YMW16 are $\sim$10 $\mathrm{pc\,cm^{-3}}$ higher than NE2001 for pulsars. The expectation of a positive minimum value for $\mathrm{DM}_{\mathrm{MW,halo}}$ motivated using the YMW16 model for final results: $\max\left[\Delta\mathrm{DM}_{\mathrm{pulsar}}\right] = 7 \pm 2\,(\mathrm{stat}) \pm 9\,(\mathrm{sys})\,\mathrm{pc\,cm^{-3}}$ (1σ uncertainty) and $\mathrm{DM}_{\mathrm{MW,halo}} > -2\,\mathrm{pc\,cm^{-3}}$ (95% c.l.). Estimates of $\mathrm{DM}_{\mathrm{ISM}}$ in our sample may be improved by characterising the line of sight to MW pulsars to find HII regions that would bias measurements. More precise pulsar distances from Gaia will also help improve ISM models. We note that should pulsars (or FRBs) be observed in Andromeda or another Local Group galaxy, one would have a strict upper bound on $\mathrm{DM}_{\mathrm{MW,halo}}$.

The FRB constraints are dominated by statistical uncertainties, i.e. results are largely limited by sample size. By modelling $\Delta\mathrm{DM}_{\mathrm{FRB}}$ and estimating the distribution using KDE with sample sizes of $n = 100$, 1000 and 10 000, we showed that the constraints may improve significantly as n increases. Specifically, with an absolute value of $\mathrm{DM}_{\mathrm{MW,halo}} = 30\,\mathrm{pc\,cm^{-3}}$, we obtained $\mathrm{DM}_{\mathrm{MW,halo}} < 114\,\mathrm{pc\,cm^{-3}}$, $\mathrm{DM}_{\mathrm{MW,halo}} < 55\,\mathrm{pc\,cm^{-3}}$, and $\mathrm{DM}_{\mathrm{MW,halo}} < 44\,\mathrm{pc\,cm^{-3}}$ (95% c.l.) for the different sample sizes. We thus expect our constraints to tighten notably once thousands of FRBs have been reported.

The upper limit derived for observed FRBs is conservative, at $\mathrm{DM}_{\mathrm{MW,halo}} < 123\,\mathrm{pc\,cm^{-3}}$. Nonetheless, it may provide a valuable bound for models of the Galactic halo and the Local Group (within which the MW lies), especially as constraints become tighter. If one assumes a Galactic halo mass of $M_{\mathrm{halo}} \approx 10^{12.2}\,\mathrm{M_\odot}$, where the MW has retained all of its cosmic baryons, one expects

$\mathrm{DM_{MW,halo}} > 50\,\mathrm{pc\,cm^{-3}}$ (e.g. Prochaska & Zheng, 2019, but see Keating & Pen, 2020). If one further assumes that the gas traces the dark matter profile (i.e. that all dark matter is dragged into the halo as the Galaxy collapses), one expects $\mathrm{DM_{MW,halo}} > 200\,\mathrm{pc\,cm^{-3}}$ (Prochaska & Zheng, 2019). This scenario is ruled out with our model, which is in agreement with analyses of Galactic X-ray emission (e.g. Fang et al., 2013, 2015). Currently, our model cannot determine whether the Galaxy has retained the majority of its baryons or whether they have been expelled, but in the future and with a larger FRB sample, it may well be able to.

Ongoing FRB projects will offer constraints on the distribution and size of $\mathrm{DM_{MW,halo}}$ and $\mathrm{DM_{host}}$. As more FRBs are localised to host galaxies, the redshift distribution will become better mapped, as will the distribution of host DMs. One can, for example, estimate the DM contribution from the ISM of the host galaxy by measuring Balmer line emission. FRB 121102 and FRB 190608 have been shown to have $\mathrm{DM_{host,ISM}} \approx 50{-}200\,\mathrm{pc\,cm^{-3}}$ and $\mathrm{DM_{host,ISM}} \approx 82 \pm 35\,\mathrm{pc\,cm^{-3}}$, respectively (Tendulkar et al., 2017; Chittidi et al., 2020). Other FRB hosts, for example that of FRB 180924 (Bannister et al., 2019), have negligible Balmer emission at the FRB location, implying a contribution of $\mathrm{DM_{host,ISM}} < 50\,\mathrm{pc\,cm^{-3}}$. The halo contribution from the host may be estimated from the stellar mass of the host galaxy by assuming a galaxy formation model. The host of FRB 180924, for example, has $\mathrm{DM_{host,halo}} < 20\,\mathrm{pc\,cm^{-3}}$ (Prochaska & Zheng, 2019), and the massive host galaxy of FRB 180924 has $\mathrm{DM_{host,halo}} \approx 50\,\mathrm{pc\,cm^{-3}}$ (Bannister et al., 2019).

If one wishes to estimate the minimum contribution of $\mathrm{DM_{cosmic}}$ from the redshift distribution of FRBs, one must be aware of selection effects. Due to (for example) flux limits and differences in the radio frequencies of emission, the localised FRB sample may be biased and not representative of the true population. One would either have to account for this when modelling the distribution, or base analyses solely on the localised sample once it has grown to a reasonable size (i.e. a couple hundred sources).

There are a number of upcoming projects that will offer constraints on $\mathrm{DM_{MW,halo}}$. One example is the Japanese X-Ray Imaging and Spectroscopy Mission (XRISM), which will provide high-precision X-ray absorption-line spectroscopy for the Galactic halo with a spectral resolution far greater than current X-ray satellites. This will provide reliable estimates of $\mathrm{O^{+5}}$ and $\mathrm{O^{+6}}$ column densities across the sky, from which one can attain at least conservative lower limits of $\mathrm{DM_{MW,halo}}$.

3.6 Conclusion

In Platts et al. (2020), we demonstrated a novel way in which one can probe the DM—i.e. the line-of-sight electron column density—of the MW Galactic halo. Using KDE, we modelled the ISM-corrected $\mathrm{DM_{pulsar}}$ and $\mathrm{DM_{FRB}}$ distributions, from which we obtained a conservative upper and lower limit on $\mathrm{DM_{MW,halo}}$. We found that $\max[\mathrm{DM_{pulsar}}] \approx 7 \pm 2\,(\mathrm{stat}) \pm 9\,(\mathrm{sys})\,\mathrm{pc\,cm^{-3}}$ and $\min[\mathrm{DM_{FRB}}] \approx 63^{+27}_{-21}\,(\mathrm{stat}) \pm 9\,(\mathrm{sys})\,\mathrm{pc\,cm^{-3}}$ (1σ uncertainty). This corresponds to bounds of $\mathrm{DM_{MW,halo}} > -2\,\mathrm{pc\,cm^{-3}}$ and $\mathrm{DM_{MW,halo}} < 123\,\mathrm{pc\,cm^{-3}}$ (95% c.l.). The lower limit from pulsars reflects only part of the MW halo, since pulsars are predominantly found in the Galactic disk. The upper limit from FRBs includes a contribution from the IGM and the host galaxy DM. Should FRBs be discovered in neighbouring galaxies and/or in the outskirts of galaxies, the methodology presented will yield more representative values of $\mathrm{DM_{MW,halo}}$. In the latter case, progenitors may be exotic (e.g. dipole collisions (Thompson, 2017a,b) or cosmic strings (Vachaspati, 2008; Yu et al., 2014; Zadorozhna, 2015; Brandenberger et al., 2017)) or magnetars that have been kicked far from their birth sites.

We did not consider the variation of $\mathrm{DM_{MW,halo}}$ as a function of Galactic latitude. This may be feasible only once thousands of FRBs are observed, and is thus left for future work. The current estimate cannot inform whether the MW is likely to have retained its cosmic average of baryons ($\mathrm{DM_{MW,halo}} > 50\,\mathrm{pc\,cm^{-3}}$), however with a sample size of a couple thousand FRBs we demonstrated that the methodology may complement other analyses. Thus, in the near future, the model may help discern the viability of Galactic halo models.

CHAPTER 4

FINE STRUCTURE IN FRBS: AUTOCORRELATION FUNCTIONS

4.1 Introduction

FRB 121102—discussed in §2.2.3—is one of the most well-studied FRBs to date. It was the first FRB observed to repeat (Spitler et al., 2016) and the first to be localised to a host galaxy: a low metallicity dwarf (Chatterjee et al., 2017; Tendulkar et al., 2017; Marcote et al., 2017). It resides in a region of high star-formation (Bassa et al., 2017)—offset slightly from the peak region (Tendulkar et al., 2021)—and is very active. This, together with its host galaxy type, suggests a young magnetar origin (§2.3.1), where the magnetar was possibly born in a rare type of core-collapse event—a Type I SLSN (e.g. Bhandari et al., 2020; Li & Zhang, 2020; Heintz et al., 2020; Bochenek et al., 2020a). Indeed, FRB 121102 does not appear to be a typical FRB: most FRBs are one-offs or have low repetition rates, and reside in older, more massive galaxies (§2.1.7; e.g. Li & Zhang, 2020). This suggests most FRBs may be associated with an older population of magnetars formed in conventional CC-SNe. While other FRB progenitors cannot be ruled out, the recent association of FRB 200428 with a Galactic magnetar does make this channel the most plausible.[1]

While the emission from Galactic pulsars and magnetars displays a range of time-frequency structures, FRBs exhibit different features, possibly due to higher energetics and propagation effects (Hessels et al., 2019). For example, FRB 121102 and several other FRBs (e.g. Farah et al., 2018; Amiri et al., 2020) have pulses with sub-bursts that drift to lower frequencies at later times. This behaviour is often present in repeating FRBs, but does not occur in all pulses—some are narrow and have no apparent substructure. Recently, Caleb et al. (2020) reported 11 bursts of FRB 121102 detected using the Meer Karoo Array Telescope (MeerKAT) radio telescope in South Africa, some of which have complex frequency structures akin to those presented by Hessels et al. (2019). Paper II of Caleb et al. (2020)—Platts et al. (2021)—provides an analysis of the burst structure and presents the structure-optimised DMs, i.e. the DMs that maximise the structure of the frequency-averaged pulse profiles.

The detections were made using the Meer TRAnsients and Pulsars (MeerTRAP) system and single pulse detection pipeline at the MeerKAT radio telescope. The observations were taken over a ∼3 hour period on the 10$^{\text{th}}$ September 2019 during FRB 121102's active phase. MeerKAT's wide band receiver extends over 900–1670 MHz, which allowed an analysis of the complex frequency structure of FRB 121102 at a relatively low frequency. The wide contiguous bandwidth reveals a number of interesting features present in the 11 bursts. Some of the bursts appear to change behaviour at ∼1250 MHz, where they either become significantly fainter, have a complex bifurcated substructure, or appear to deviate from the characteristic arrival time $\Delta t \sim \nu^{-2}$. Two of the pulses (bursts 03 and 05) are observed as pulse pairs. Here, small 'precursor' bursts are separated from the main bursts by ∼28 ms and ∼34 ms, respectively, with the inter-pulse signal level equal to the noise floor.

Pulse pairs have been observed in FRB 121102 before. Precursors have been detected by the Effelsberg telescope (∼34 ms separation; Hardy et al., 2017) and the Lovell telescope (∼17 ms separation; Rajwade et al., 2020a). Postcursor bursts have also been observed, where a bright main pulse arrives before a fainter pulse. These have been detected by the Arecibo telescope (∼26 ms separation; Gourdji et al., 2019), the Green Bank telescope (∼37 ms separation; Scholz et al., 2017), and the

[1] As well as SNR models (§2.3.1), this includes NS-asteroid progenitor models (§2.3.4.1). Periodicity would be a result of system configuration, and not a feature common to all FRBs.

Effelsberg radio telescope (∼38 ms separation; Cruces et al., 2021). Other FRBs have also been observed with pulse pairs, for example: FRB 180916.J0158+65 (Andersen et al., 2019; Chawla et al., 2020; Amiri et al., 2020; Marthi et al., 2020), FRB 190212.J18+81 (Fonseca et al., 2020), FRB 181112 (Prochaska et al., 2019; Cho et al., 2020), FRB 190102 (Day et al., 2020), FRB 190611 (Day et al., 2020), and FRB 200428 (Bochenek et al., 2020a; Andersen et al., 2020), with separation times between ∼0.1−90 ms. Many repeating FRBs have multiple sub-bursts, and it can be ambiguous whether these are separate bursts or components of the same burst.

As previously mentioned, a common feature of repeating FRBs is a downward drift in frequency (e.g. Hessels et al., 2019; Andersen et al., 2019; Amiri et al., 2020; Fonseca et al., 2020). In fact, it has recently been shown that FRB 121102, FRB 180916.J0158+65 and FRB 180814.J0422+73 have an inverse relationship between their frequency drift rate and the temporal durations of their sub-bursts (Chamma et al., 2020). Upward drifting substructure, however, has yet to be definitively observed. Some pulse pairs might be examples of upward drift, where the second burst arrived at a higher frequency than the first, but it is unclear whether the bursts are emitted within the same burst envelope or are independent events. Examples of this are FRB 180916.J0158+65 (Chawla et al., 2020; Amiri et al., 2020), FRB 190611 (Day et al., 2020), FRB 200428 (Bochenek et al., 2020a; Andersen et al., 2020), burst 6 (Hilmarsson et al., 2021) and burst 03 (Caleb et al., 2020; Platts et al., 2021). If the bursts are indeed emitted within the same envelope, upward drift could be evidence of plasma lensing, which could help inform of the local environment and emission mechanisms for FRBs.

Repeating bursts also tend to have a bandwidth of ∼200 MHz at 1.5 GHz (Hessels et al., 2019; Gourdji et al., 2019). This is apparent in the MeerKAT data set, too. Pleunis et al. (2020) show that the fractional bandwidth of repeaters is typically ∼20−30%, however there are exceptions (e.g. Law et al., 2017). Indeed, the main bursts of bursts 03 and 05 appear to be have bandwidths of least 500 MHz.

The burst morphology of some FRBs evolves with frequency, which means there is an ambiguity between burst structure and the DM (Gajjar et al., 2018; Hessels et al., 2019). A pulse is de-dispersed to best represent the pulse at inception, i.e. to align the emission such that all frequencies were emitted at the same time. For a narrow pulse with no discernible structure, the optimal DM is determined by maximising the signal-to-noise (S/N). For a burst with substructure, however, different frequencies are not necessarily emitted at the same time. The DM is thus affected by the innate frequency-dependent emission time, as well as local and global propagation effects. In order to understand FRB mechanisms, it is essential that components intrinsic to FRBs are resolved. One way of doing this is by maximising the frequency-averaged pulse structure. This allows one to derive sub-pulse timescales and calculate frequency drift rates. An important caveat, however, is the possible presence of unresolved sub-bursts. There may be unresolved features that would significantly effect the DM calculation; for example see Marthi et al. (2020), where a burst that appears to have a different DM to other bursts may be made up of unresolved sub-bursts that drift down in frequency.

In Platts et al. (2021), we calculated the structure-optimised DM with two approaches: by using ACFs to minimise the width of pulse structure and by applying the algorithm `DM_phase` (Seymour et al., 2019; Seymour et al., *in prep*) to maximise the coherent power spectrum of a pulse. This allowed a detailed look at 10 out of the 11 bursts of FRB 121102 reported in Caleb et al. (2020).

This chapter is laid out as follows. A brief description of the observations and data reduction is given in §4.2 (a detailed description can be found in Caleb et al., 2020). The methodology is described in §4.3, and the analysis and results are presented in 4.4. The chapter concludes with §4.5.

4.2 Observations and Data Reduction

The South African Radio Astronomy Observatory (SARAO) Meer Karoo Array Telescope (MeerKAT, where "meer" means "more" in Afrikaans; Jonas & MeerKAT Team, 2016; Camilo et al., 2018; Mauch et al., 2020) is a radio interferometer in the Karoo region of South Africa, and is the

precursor to the Square Kilometre Array (SKA) telescope. It consists of 64 dishes, each with a 13.96 m diameter, distributed out to a radius of 4 km. 61% of the dishes lie within ∼1 km of the array center. The observations presented in Caleb et al. (2020) were found while using an operating center frequency of 1284 MHz with a usable bandwidth of ∼770 MHz. The MeerKAT telescope hosts the MeerTRAP project (Sanidas et al., 2018), which performs fully commensal, real-time, high time-resolution searches for pulsars and fast transients in conjunction with other ongoing MeerKAT Large Survey Projects. MeerKAT operates in a coherent and incoherent mode simultaneously using the MeerTRAP backend. In the coherent mode, data from the inner 40 dishes is typically combined to form 396 beams on the sky with a field-of-view of ∼0.2 square degrees. In the incoherent mode, all 64 MeerKAT dishes are combined to form a wide (less sensitive) field-of-view of ∼1 square degree. For the observations presented in Caleb et al. (2020), a phased array of 60 MeerKAT dishes was used. The final data have 4096 channels over a 856 MHz bandwidth with a time-resolution of 306 µs. The data have only Stokes I information, i.e. no polarisation data is available. The radio frequency interference (RFI) was removed from the data manually, which masked ∼30% of the band. The data reduction was done using PSRCHIVE[2] (van Straten et al., 2012) and SIGPROC[3] (Lorimer, 2011). A step-by-step guide on the process is given in Appendix A.

4.3 Methodology

4.3.1 Optimising the DM

By maximising the S/N of each pulse, the DM of FRB 121102 is found to be between 553–569 pc cm^{-3} (Spitler et al., 2014; Law et al., 2017; Scholz et al., 2016). Upon the discovery of substructure, however, Gajjar et al. (2018) optimised the S/N of the individual sub-bursts, which resulted in higher DM values compared with those previously reported. The S/N of individual components was found by maximising the structure parameter: the average absolute rate of change of the total flux density across the pulse window,

$$\text{Structure Parameter} = \frac{1}{n}\sum_{i}^{n}\left|\frac{S_i - S_{i+1}}{\Delta t}\right| \ , \tag{4.3.1}$$

where n is the number of bins, S_i is the flux at the i^{th} bin, and Δt is the time-resolution. Following on from this, Hessels et al. (2019) calculated the optimal DM by maximising the steepness of peaks in the frequency-averaged profile. Specifically, they considered the DM that maximises the mean square of each profile's forward difference time derivative. The time-resolution of the MeerKAT data (306 µs), however, is too coarse for these approaches. Dispersion smearing compounds this problem: using Equation 1.4.4, the dispersion smearing is at best ∼1 ms at 1 GHz and ∼250 µs at 1.6 GHz. As such, in Platts et al. (2021) we considered two alternative methods: minimising the pulse widths using autocorrelation functions (ACFs; e.g. Cordes et al., 1990; Lange et al., 1998) and maximising the coherent power across the bandwidth using the `DM_phase` algorithm (Seymour et al., 2019). Both methods are applicable to higher resolution data, too. The data was de-dispersed across a trial range of DM = 540−590 pc cm^{-3} with a step size of 0.1 pc cm^{-3}.

4.3.2 Autocorrelation Functions

4.3.2.1 *Theory*

ACFs define the correlation between series of data at different times (e.g. Kardashev et al., 1978; Cordes et al., 1990), i.e. they define the correlation of a signal with a delayed copy of itself as a function of the time lag. ACFs are a useful tool in determining the typical widths of structures in a single transient pulse, and proved to be appropriate for our analysis of FRB 121102. The narrow structures of the pulse contribute to the ACF up to a scale that corresponds to their pulse width. As such, the presence of narrow structure is evidenced by a flattening in the ACF, i.e. where the ACF flattens, the narrow features no longer contribute to it. The lower the time lag value at which

[2] Available `http://psrchive.sourceforge.net`.

[3] Latest version available at `https://github.com/SixByNine/sigproc`. For documentation, `http://sigproc.sourceforge.net/`.

the ACF flattens, the shorter the pulse width and the more enhanced the substructure.

The ACF of a single pulse can be defined as:

$$a_i(n) = K_i \sum_{j=1}^{N_{\rm bin}} I_i(j) \cdot I_i\left((j+n) - N_{\rm bin} \cdot \Theta\left(j+n-N_{\rm bin}\right)\right) \quad , \tag{4.3.2}$$

where $I_i(j)$ is the intensity of the $j^{\rm th}$ sample of the pulse, Θ is the Heaviside function, K_i is a normalization factor, and $N_{\rm bin}$ is the number of samples in the pulse. $a_i(n)$ corresponds to the input flux data at bin n for a frequency i. The averaged ACF of k single pulses is then:

$$A(n) = \frac{1}{k} \sum_{i=1}^{k} a_i(n) \quad . \tag{4.3.3}$$

Via the Wiener–Khinchin theorem, the autocorrelation can be calculated from raw data $x(t)$ with fast Fourier transforms (FFTs). With time lag $\tau = t_2 - t_1$ and data $x(t)$, the ACF $A(\tau)$ can be computed via:

$$F_A(f) = \mathrm{FFT}\left[x(t)\right] \quad , \tag{4.3.4}$$
$$S(f) = F_A(f) F_A^*(f) \quad , \tag{4.3.5}$$
$$A(\tau) = \mathrm{IFFT}\left[S(f)\right] \quad , \tag{4.3.6}$$

where $S(f)$ is the power spectral density, IFFT is the inverse FFT, and the asterisk denotes the complex conjugate.

The point at which the ACF flattens is defined by Hankins (1972) to be the point of intersection between two tangents fitted to the steep (narrow) region and the shallow (broad) region of the ACF. This is illustrated in Figure 4.1a. To automate this process, Lange et al. (1998) developed the Turn-Off Point (TOP) algorithm, where instead of fitting tangents by hand, a point of 'significant flattening' is determined by comparing the gradient of the ACF in different regions. We implemented this algorithm in Python, as described in §4.3.2.2. An example is given in Figure 4.1b, where the ACFs for burst 11 are shown for DM $= 563.7 \pm 1.0\,\mathrm{pc\,cm^{-3}}$, with $\mathrm{DM_{struct}} = 563.7\,\mathrm{pc\,cm^{-3}}$. Figure 4.2 shows the corresponding dynamic spectra and frequency-averaged pulse profiles (lower panel), and the DM versus time lag obtained via the TOP algorithm (upper panel). Where pulses were particularly faint, the ACF curves were smoothed slightly to avoid the effects of noise spikes on the TOP algorithm.

Final results were obtained by interpolating the DM versus time lag curve ($f_{\rm ACF}$) and taking $\mathrm{DM_{struct}}$ to be the value where the time lag is minimised. The standard deviation was calculated via the Taylor series,

$$\sigma_{\rm DM} = \sqrt{\left| \frac{2\sigma_{f_{\rm ACF}}^2}{f''_{\rm ACF}(\mathrm{DM_{struct}})} \right|} \quad , \tag{4.3.7}$$

where σ_f is given by the residuals of the interpolation.

4.3.2.2 *Optimisation routine*

Using the TOP algorithm,[4] we calculated the point at which each bursts' ACF becomes significantly flatter for each DM in the trial range. The zero-lag ACF point contains system noise, which is broadened by dispersion smearing and can influence the first lag. The algorithm therefore starts from the second lag. Two tests were performed to find the turn-off point; the first checks for local flattening and the second for non-local flattening. The algorithm is as follows:

1. Search for local flattening at each lag over a 4 bin period. The absolute value of the local difference $|d_{n_i} = A(n_i) - A(n_i - 1)|$ is calculated for the starting ACF lag point n_0 and compared to the following $d(n_i)$ for $i = 0, ..., 4$. If a $d(n_i)$ is significantly lower than $d(n_0)$—defined as $d(n_i) > d(n_0)/c_1$—then the corresponding n_i becomes a candidate flattening point that is passed to Test 2. If no $d(n_i)$ satisfy this condition, the test restarts with $n_0 = n_0 + 1$.

[4] Our version available in Python at https://github.com/EmPlatts/FRB_121102_meerkat.

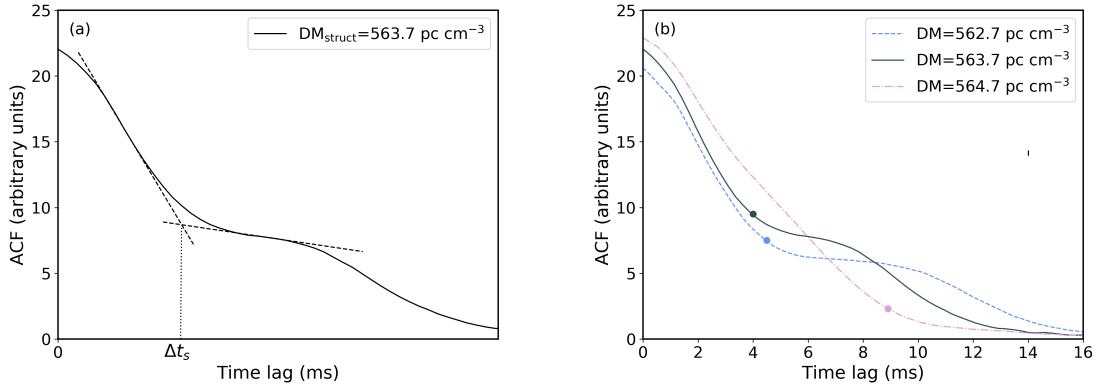

Figure 4.1: Based on Figure 1 of Platts et al. (2021). (a) The frequency-averaged ACF for burst 11 with $\mathrm{DM_{struct}} = 563.7\,\mathrm{pc\,cm^{-3}}$. The sub-pulse is depicted by the first bump, whose structure contributes up to a timescale of Δt_s ms—the point at which the ACF flattens—as determined by the intersecting tangents. (b) An example of ACFs for burst 11 de-dispersed to different DMs. The circles correspond to the points of flattening—determined using the TOP algorithm—and give the structure timescales. The time lag is minimised at the structure-optimised DM of $563.7\,\mathrm{pc\,cm^{-3}}$. By DM = $564.7\,\mathrm{pc\,cm^{-3}}$, the ACF smooths out, driving the flattening point to significantly lower values.

2. To avoid the influence of noise, test for non-local flattening. The candidate point n_c is compared to a non-local difference of 8 bins before and after the point. To pass the second test, we require $|A(n_c) - A(n_c - 8)| < c_2|A(n_c) - A(n_c + 8)|$. If this condition is not satisfied, the procedure repeats from Test 1 with $n_0 = n_c + 1$.

c_1 and c_2 are the sensitivity parameters, chosen by hand for each pulse. c_1 is 2, 3 or 4, and c_2 is in the range 1.5−4 in step sizes of 0.5. Pulses with an obvious flattening have values close to $c_1 = 2$ and $c_2 = 1.5$, and pulses with subtle turn-off points have values closer to $c_1 = c_2 = 4$, i.e. the sensitivity is higher (c higher) for ACFs which curve less at the flattening point (see Figure 4.3.). Lange et al. (1998) uses $c_1 = 2$ and $c_2 = 1.5$ for their pulsar sample.

4.3.3 Coherent Power Spectra

`DM_phase`[5] finds the structure-optimised DM of a pulse by maximising the coherent power across the bandwidth (Seymour et al., 2019). The dynamic spectrum $D(t', f)$ is given as a function of emission frequency and time, where t' is the time shifted by the delay expected at the corresponding frequency. Casting this into the Fourier domain, one obtains:

$$\mathcal{F}\left[D(t', f)\right] \rightarrow D(\omega, f) e^{i\omega C\, DM/f^2} \quad , \tag{4.3.8}$$

where $\mathcal{F}$ denotes the Fourier transform, ω is the Fourier frequency and C is the dispersion constant. From this it is evident that all of the dispersion information is encoded in the phase angle $\Phi(\omega) = \omega C\, DM/f^2$. One can thus divide by the amplitudes to retain only the phase angle information. A coherent spectrum is created by integrating over the emission frequency. Here, coherent Fourier frequencies will sum to have the maximum amplitude. Since it is the burst structure that is of interest, the time-derivative of the power spectrum is taken to obtain:

$$P_{\mathrm{dCo}}(\omega, DM) = \omega^2 \left| \int \frac{\mathcal{F}\left[D(t', f)\right]}{\left|\mathcal{F}\left[D(t', f)\right]\right|} \mathrm{d}f \right|^2 \quad . \tag{4.3.9}$$

The DM versus power is interpolated to obtain the final result, where the point of maximum power corresponds to the structure-optimised DM.

To obtain uncertainties, Seymour et al. (2019) find the standard deviation of the power spectrum $P_{\mathrm{dCo}}(\omega, DM)$ and from this deduce the standard deviation of the DM. A uniform distribution in

[5] Available at https://github.com/danielemichilli/DM_phase.

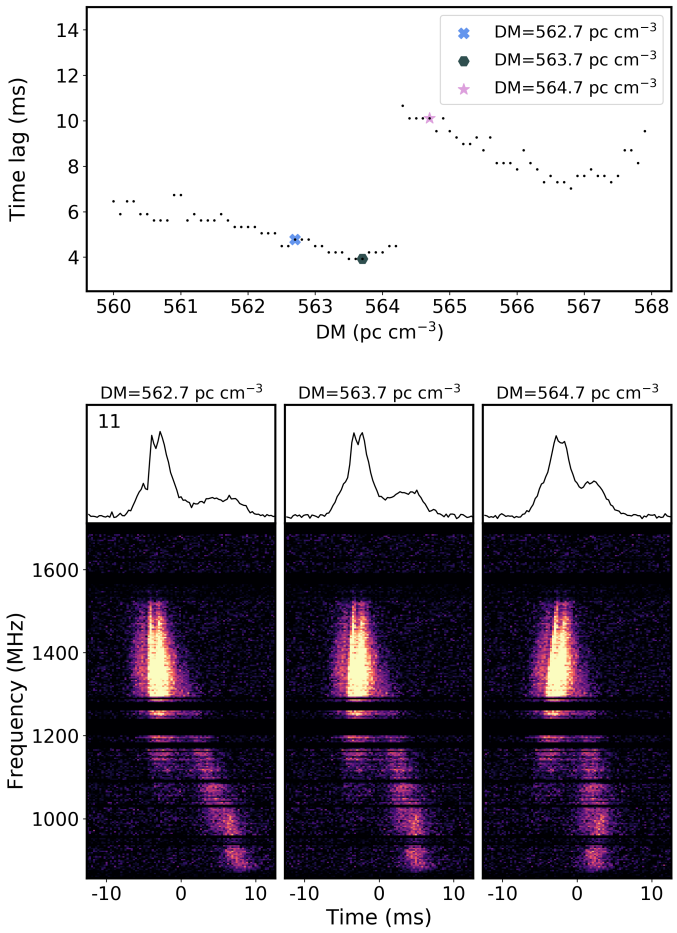

Figure 4.2: Based on Figure 2 of Platts et al. (2021). The top panel shows the DM versus time lag for burst 11. At DM $\approx 564.3\,\mathrm{pc\,cm^{-3}}$, there is a jump to higher time lag values, which is reflected by the behaviour of the ACFs in Figure 4.1b. The bottom panel shows the frequency-averaged pulse profiles and waterfall plots de-dispersed to the corresponding DMs. The resolution of the spectra is decimated to 256 channels.

phase angles between $-\pi$ to π is modeled as $\mathrm{PDF}(\theta) = \frac{\mathrm{d}\theta}{2\pi}$. With the X component as $X = \cos\theta$,

$$\mathrm{PDF}(X) = \frac{\mathrm{d}X}{2\pi \sin\left(a\cos(X)\right)} \quad , \tag{4.3.10}$$

with an expectation value of zero and a standard deviation of $\sigma_x = \frac{1}{2}$. Summing over the frequency channels n_{chan} and applying the central limit theorem,

$$\sigma_{\sum x} = \frac{\sqrt{n_{\mathrm{chan}}}}{2} \quad . \tag{4.3.11}$$

The uniform PDF is then re-parameterised to a power distribution given by $\Gamma(2, n_{\mathrm{chan}})$. This results in an expectation value of $\langle P_{\mathrm{Co}} \rangle = n_{\mathrm{chan}}$ and a standard deviation of $\sigma_{P_{\mathrm{Co}}} = \frac{n_{\mathrm{chan}}}{\sqrt{2}}$. Summing across the Fourier frequency and applying the central limit theorem,

$$\sigma^2_{\sum P_{\mathrm{dCo}}} \equiv \sigma_P = \frac{n_{\mathrm{chan}}}{2} \sum \omega^4 \quad , \tag{4.3.12}$$

where the ω^2 term is the weighting from Equation 4.3.9 when going from the power spectrum to its time derivative.

The uncertainty in the coherent power spectrum σ_P is converted into an uncertainty in DM (σ_{DM}) via the Taylor series to obtain:

$$\sigma_{\mathrm{DM}} = \sqrt{\left| \frac{2\sigma_P^2}{P''(\mathrm{DM_{struct}})} \right|} \quad , \tag{4.3.13}$$

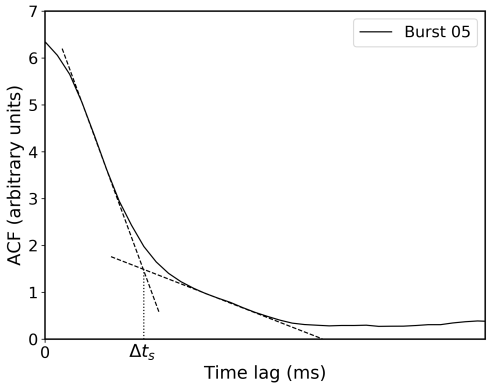

Figure 4.3: The ACF of burst 05. The flattening is more subtle than for burst 11 (Figure 4.1), for example. This illustrates the requirement for bursts to have their own set of sensitivity parameters for the algorithm described in §4.3.2.2.

where P'' is the second derivative of the coherent power with respect to the DM.

4.4 Analysis and Results

The structure-optimised DMs obtained using ACFs and `DM_phase` are presented in Table 4.1. The corresponding frequency spectra (or "waterfall plots") are shown in Figure 4.4. The flux of burst 01 is too low to determine $\mathrm{DM_{struct}}$ with either method, and thus the burst is not shown. Where the structure-optimised DMs given by the ACF and `DM_phase` methods agree, bursts are de-dispersed to the mean of the two results. Where they differ, the most likely candidate DM is used (as discussed in §4.4.1). §4.4.1 provides a comparison of the two methods. In §4.4.2 the average DM for the epoch is calculated. A number of caveats in determining $\mathrm{DM_{struct}}$ are highlighted here. The sub-bursts and pulse pairs are discussed in §4.4.3 and §4.4.4, respectively. Frequency drift is discussed in §4.4.5.

Table 4.1: Structure-optimised DMs for the 11 FRB 121102 bursts. Due to their low fluxes, including/excluding the precursors in the analysis for bursts 03 and 05 did not affect the value of $\mathrm{DM_{struct}}$. For bursts 07, 08 and 10, `DM_phase` gave multiple possible values, as discussed in Section 4.4.1. Asterisks denote the selected sample of best estimates used in the second calculation of the average DM.

Burst	ACF Method ($\mathrm{pc\,cm^{-3}}$)	DM_phase ($\mathrm{pc\,cm^{-3}}$)
01	—	—
02	$564.1 \pm 0.3^*$	$565.1 \pm 0.4^*$
03	566.0 ± 0.2	565.8 ± 0.2
04	572.0 ± 0.8	572.7 ± 0.3
05	564.5 ± 0.3	564.4 ± 0.3
06	562.8 ± 0.9	563.4 ± 0.7
07	563.1 ± 0.4	$562.9 \pm 0.2^*$
		564.4 ± 0.2
		565.6 ± 0.2
08	564.4 ± 0.4	$563.6 \pm 0.1^*$
		564.9 ± 0.6
09	565.0 ± 0.9	565.2 ± 1.1
10	563.3 ± 0.4	563.6 ± 0.4
		565.8 ± 0.4
11	563.7 ± 0.6	$562.8 \pm 0.3^*$

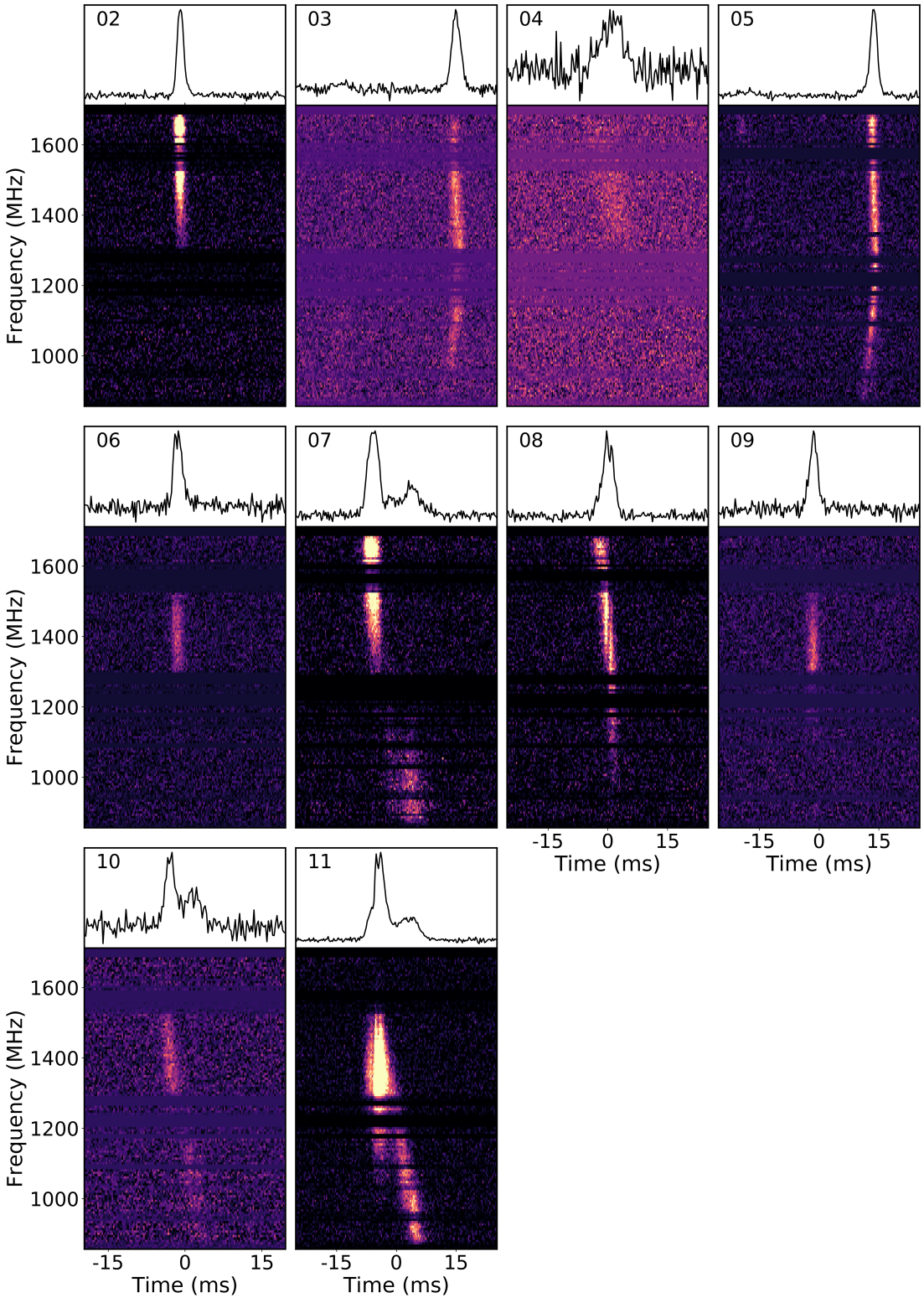

Figure 4.4: Based on Figure 3 of Platts et al. (2021). The dynamic spectra of 10 of the 11 bursts detected with MeerKAT in September 2019. The structure-optimised DM of burst 01 could not be found with reasonable certainty. The top panels show the frequency-averaged pulse profile. The bottom panels show the frequency spectra with the resolution of each burst decimated to 256 channels to enhance visibility. The time-resolution of the pulses is 306.24 µs. The data was cleaned manually. The data are uncalibrated, and the flux densities are in arbitrary units. The bursts are de-dispersed to the structure-optimised DMs given in Table 4.1 (the mean of ACF and `DM_phase`). Bursts 07, 08 and 10—for which multiple DMs are given—are de-dispersed to 563.0 pc cm^{-3}, 563.6 pc cm^{-3} and 563.4 pc cm^{-3}, respectively.

4.4.1 Comparison of Methods

ACFs and the `DM_phase` algorithm gave results that largely agree (1σ c.l.). Both methods failed to identify $\mathrm{DM_{struct}}$ with reasonable certainty for burst 01 and the precursor of burst 03, because the burst fluxes are too low. The uncertainties associated with the methods are comparable. `DM_phase` gave multiple possible values for bursts 07, 08 and 10, i.e. the coherent power spectrum had multiple peaks. There are three possible values for burst 07, shown in Figure 4.7a. The first is $\mathrm{DM} = 562.9 \pm 0.2\,\mathrm{pc\,cm^{-3}}$, which agrees with the ACF method ($\mathrm{DM} = 563.1 \pm 0.4\,\mathrm{pc\,cm^{-3}}$). At least three distinct sub-pulses are apparent. We took this to be the structure-optimised DM. For the next two `DM_phase` values for $\mathrm{DM_{struct}}$, the sub-pulses begin to sweep under the main pulse, thereby reducing substructure in the frequency-averaged profile. `DM_phase` gives two possible values for burst 08 (Figure 4.7b). The second panel shows the DM that agrees with the ACF result ($\mathrm{DM_{struct}} = 564.9 \pm 0.6\,\mathrm{pc\,cm^{-3}}$ versus $\mathrm{DM_{struct}} = 564.4 \pm 0.4\,\mathrm{pc\,cm^{-3}}$), but here one can see that the substructure has been lost. As such, we took $\mathrm{DM_{struct}} = 563.6 \pm 0.1\,\mathrm{pc\,cm^{-3}}$, where two distinct sub-bursts are visible and drift downwards in frequency. Figure 4.7c shows the two $\mathrm{DM_{struct}}$ values given by `DM_phase` for burst 10. At $\mathrm{DM_{struct}} = 563.6\,\mathrm{pc\,cm^{-3}}$, there are two distinct bursts. This is in agreement with the ACF method ($\mathrm{DM_{struct}} = 563.3 \pm 0.4\,\mathrm{pc\,cm^{-3}}$). At $\mathrm{DM_{struct}} = 565.8\,\mathrm{pc\,cm^{-3}}$, the sub-bursts align and wash out the structure in the pulse profile. Here, the two sub-bursts do not appear to align perfectly vertically and they appear to be separated by a region of dimness. This suggests they are indeed two distinct sub-bursts. It is possible, however, that the missing frequency bands near 1250 MHz create an illusion of two separate bursts. We thus tentatively took $\mathrm{DM_{struct}} = 563.6 \pm 0.4\,\mathrm{pc\,cm^{-3}}$ for burst 10, and noted that it is similar to bursts 07 and 11 in appearance and behaviour. The DM values for burst 11 given by `DM_phase` and the ACF method differ marginally ($\mathrm{DM_{struct}} = 562.8\,\mathrm{pc\,cm^{-3}}$ and $\mathrm{DM_{struct}} = 563.7\,\mathrm{pc\,cm^{-3}}$, respectively). By eye, the `DM_phase` result appears most correct (Figure 4.2).

`DM_phase` successfully identified structure in 10 of the 11 bursts. When multiple values were given by `DM_phase`, the highest peak did not necessarily correspond to $\mathrm{DM_{struct}}$. One should thus check results carefully by eye. The ACF method was unable to identify substructure in burst 08. Here the time between sub-bursts was less than a millisecond. `DM_phase` is therefore more sensitive than the ACF method. The ACF method is also limited because it requires one to manually adjust smoothing parameters c_1 and c_2 (described in §4.3.2.2) to suit the data. Since `DM_phase` proved to be more sensitive to structure than the ACF method, we did not attempt to automate the parameter selection. `DM_phase`, on the other hand, is robust for a range of different pulses.

While the two definitions of 'maximum structure' give results that are largely consistent with each other, ambiguity still exists within the metric. For example, at 2σ, the two solutions for burst 8 are compatible, but visual inspection shows they are clearly alternative to each other. Care should be taken when performing these types of analyses and results should be accepted with a measure of caution.

4.4.2 Average DM for the Epoch

The average structure-optimised DM of the epoch is calculated in two ways. In the first, the average is taken over the 10 bursts, weighted by the errors, to give $\mathrm{DM_{struct}} = 564.8 \pm 0.6(\mathrm{sys}) \pm 2.5(\mathrm{stat})\,\mathrm{pc\,cm^{-3}}$ and $\mathrm{DM_{struct}} = 564.4 \pm 0.6(\mathrm{sys}) \pm 2.9(\mathrm{stat})\,\mathrm{pc\,cm^{-3}}$ using the ACF method and `DM_phase`, respectively. The first uncertainty is the systematic uncertainty given by the respective methods and the second is the statistical uncertainty given by the standard deviation of the data. The values of $\mathrm{DM_{struct}}$ for some of the bursts fall outside of this region. The most notable is burst 04, which is $\sim 8\,\mathrm{pc\,cm^{-3}}$ greater than the average. We attribute this difference to insufficient S/N. Unresolved components in the bursts may also significantly influence the resultant $\mathrm{DM_{struct}}$. Caution should thus be taken when interpreting the DM change between bursts. The errors given by both methods are also under-representations of the true uncertainty on the measurement, as they do not take into account potentially unresolved components. As such, even individual results with small uncertainties should be closely examined. Good examples of this are bursts 03 and 05, whose ambiguity is discussed in §4.4.4.2.
sub-components

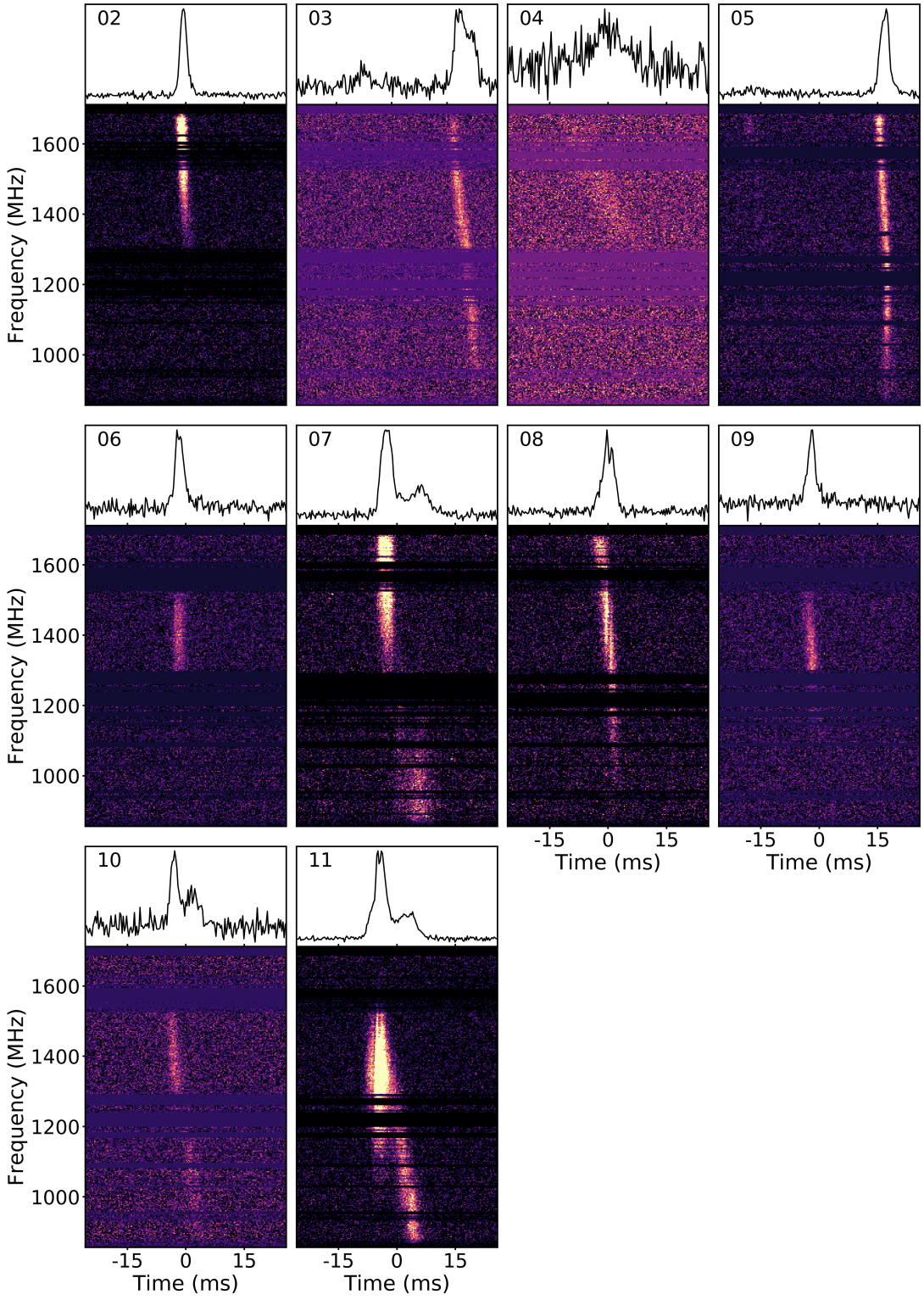

Figure 4.5: Bursts de-dispersed to an average structure optimised DM of $\sim$563.5 pc cm^{-3}. Note the difference in the behaviour of the main bursts of 03 and 05 from that shown in Figure 4.4. Instead of showing an apparent deviation from the $t \sim \nu^{-2}$ relationship, the middle section of the main bursts are misaligned, and are thus possibly made up of unresolved downward drifting sub-bursts.

As such, it is arguably more appropriate to calculate the mean DM for the epoch by only considering bursts whose sub-components appear to be reasonably resolved (e.g. Hessels et al., 2019; Majid et al., 2020). The average DM is calculated with a selected sample of bursts and their best estimates. The final data set consists of burst 02 (mean of ACF and `DM_phase`), burst 08 (`DM_phase`), burst 07 (`DM_phase`) and burst 11 (`DM_phase`). This gives a structure-optimised DM of $563.5 \pm 0.2(\text{sys}) \pm 0.8(\text{stat})\,\text{pc}\,\text{cm}^{-3}$. Figure 4.5 shows the bursts de-dispersed to $563.5\,\text{pc}\,\text{cm}^{-3}$. An important question then is whether this single DM creates a cohesive picture of the burst sample. This is discussed in Section 4.4.4.2.

The average structure-optimised DM is consistent with 2019 observations ($563.6 \pm 0.1\,\text{pc}\,\text{cm}^{-3}$; Majid et al., 2020) and with 2018 observations ($563.6 \pm 0.5\,\text{pc}\,\text{cm}^{-3}$; Josephy et al. 2019 and $563.5 \pm 1.3\,\text{pc}\,\text{cm}^{-3}$; Oostrum et al. 2020). The uncertainties make it unclear whether the average DM has indeed remained constant over this period, or whether it has increased or even decreased. A linear interpolation with 2016 observations ($\sim 560.6\,\text{pc}\,\text{cm}^{-3}$; Hessels et al., 2019) reveals an average increase of $\sim 1\,\text{pc}\,\text{cm}^{-3}$. This is roughly consistent the $\sim 1\text{–}3\,\text{pc}\,\text{cm}^{-3}$ increase from 2012 to 2016 reported by Hessels et al. (2019), however more data is needed in our case to confirm whether the increase is indeed secular. Note that Seymour et al. (*in prep*) show that the relationship is unlikely to be linear.

Table 4.2: The average structure-optimised DM of FRB 121102 for observations occurring between 2016 and 2019.

Obs Date	$\text{DM}_{\text{struct}}$ ($\text{pc}\,\text{cm}^{-3}$)	Method	Reference
Sept 2016	560.57 ± 0.07	max steepness	Hessels et al. (2019)
Nov 2018	563.6 ± 0.5	max steepness	Josephy et al. (2019)
Nov 2018	563.5 ± 1.3	`DM_phase`	Oostrum et al. (2020)
Sept 2019	563.6 ± 0.1	`DM_phase`	Majid et al. (2020)
	563.5 ± 1.0	ACF and `DM_phase`	Platts et al. (2021)

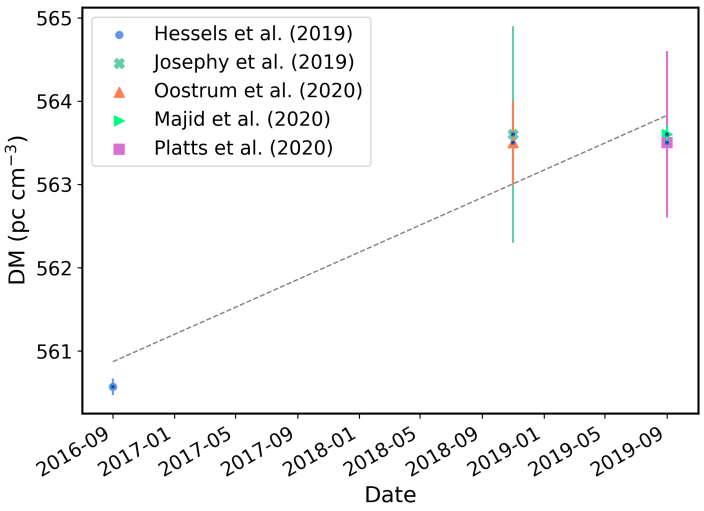

Figure 4.6: Based on Figure 7 of Platts et al. (2021). Structure-optimised DMs measured for FRB 121102 between 2016 and 2019. The dashed grey line shows a linear interpolation of the data. Note, however, that Seymour et al. (*in prep*) suggests the relationship is not simply linear.

An increasing or constant DM may at first seem inconsistent with SNR theories, since the DM is typically expected to decrease as the nebula expands. A persistent increase in DM, however, is expected if the SN ejecta expands into a high density ISM (Yang & Zhang, 2017; Piro & Gaensler, 2018). A young remnant star may also ionise surrounding gas, driving outward expansion into a surrounding HII region (Yang & Zhang, 2017). The FRB source may also be rapidly moving

through an HII region due to a SN kick. In this scenario the DM may increase or decrease depending on the direction of the kick (Yang & Zhang, 2017). In magnetar flare models, the increase may be attributed to the photoionisation of neutral gas by the UV and X-ray radiation from the shock (Margalit & Metzger, 2018). On a time scale of days to months, an increase of $0.01-1\,\mathrm{pc\,cm^{-3}}$ can reasonably be expected. Plasma lensing can also cause the DM to increase for a period of time, however because the geometry of the lens is expected to change over time (e.g. Cordes et al., 2017), the DM should begin to decrease in the future. In this case, plasma lensing would be local to the source (for example in the nebula) or the host galaxy (for example in AGNs; Cordes et al., 2017). Non-local propagation effects—such as from Hubble expansion, gas density fluctuations in large-scale structure and gravitational potential fluctuations—cannot account for the DM variations of FRB 121102 (Yang & Zhang, 2017).

4.4.3 Sub-bursts

Several bursts have notable substructure. Here we limit our discussion to bursts 07, 08, 10 and 11. Those with precursors (bursts 03 and 05) are discussed in §4.4.4. The remaining bursts are narrow with no apparent substructure, although this may be due to insufficient time-resolution.

Bursts 07 and 11 (and possibly 10) have a bifurcating structure at ∼1250 MHz. Similar behaviour has been observed in FRB 121102 before (burst GB-01; Hessels et al., 2019) and in FRB 180916.J0158+65 (burst 11; Marthi et al., 2020), where the right-most component of each burst appears to follow a different DM to the previous components. Burst 11 in Marthi et al. (2020) is particularly notable: here, a bright component that aligns with the previous sub-bursts is embedded in the right-most sub-burst. This presents the possibility that the sub-bursts of bursts 07 and 11 are not single bursts with a different DM, but rather comprise multiple components that drift down in frequency. We investigate the apparent change in by de-composing the pulses into their two constituent sub-bursts by considering the upper and lower frequency regions. Burst 07 we split at 1250 MHz. The DM of the higher frequency sub-burst is $\sim 1\,\mathrm{pc\,cm^{-3}}$ lower than that of the lower frequency sub-burst ($563.3 \pm 0.7\,\mathrm{pc\,cm^{-3}}$ versus $564.4 \pm 0.4\,\mathrm{pc\,cm^{-3}}$, using `DM_phase`). For burst 11 (whose divide is less clear-cut) was split at 1100 MHz. The DM of the higher frequency sub-burst is $\sim 2\,\mathrm{pc\,cm^{-3}}$ higher than that of the lower frequency sub-burst ($564.9 \pm 0.5\,\mathrm{pc\,cm^{-3}}$ versus $562.7 \pm 0.4\,\mathrm{pc\,cm^{-3}}$, using `DM_phase`).

This relatively large change in apparent DM on a short timescale has implications for progenitor models and local environment. The bursts may be multiply imaged by plasma lensing, which can account for a DM variation of up to $\sim 1\,\mathrm{pc\,cm^{-3}}$ (Cordes et al., 2017). Different sight-lines through dense plasma may also cause the observed change in DM (Cho et al., 2020; Day et al., 2020); for example, in the case of a neutron star origin, the line-of-sight through a nebula will vary depending on the NS rotation phase (Simard & Ravi, 2020). This differential DM, however, is expected to be low. Similarly, the observed DM variation cannot be attributed to frequency-dependent emission times in the magnetosphere. It will be interesting to see in higher resolution data whether similar sub-bursts truly do misalign with previous sub-bursts or if the effect is a result of downward drifting substructure. This clearly has implications on the DM of FRB 121102 for an epoch. If the right-most sub-bursts are made up of unresolved sub-bursts that align with the main burst, then the DM of the burst is best described by the DM of the main burst.

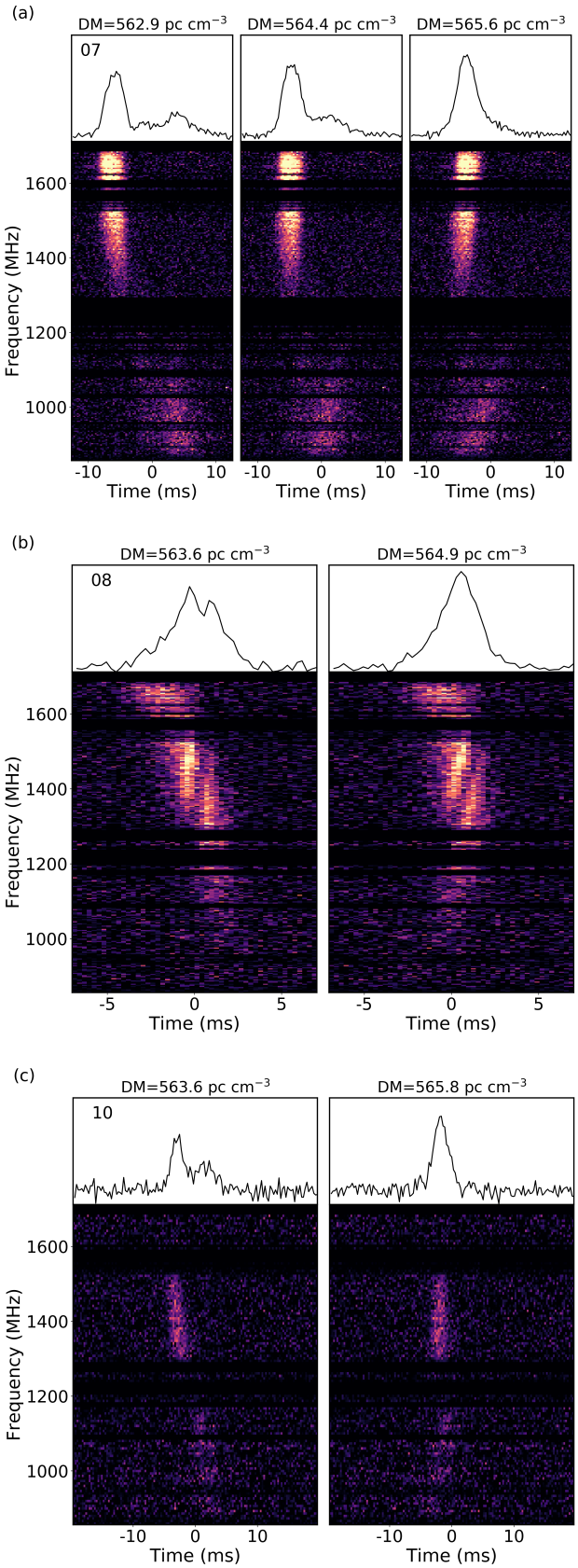

Figure 4.7: Based on Figures 4, 5 and 6 of Platts et al. (2021). `DM_phase` results. (a) Burst 07. The first panel agrees with the ACF method ($\mathrm{DM_{struct}} = 563.1 \pm 0.2\,\mathrm{pc\,cm^{-3}}$). The profile has less substructure as the lower frequency pulses begin to sweep under the main pulse. (b) Burst 08. The second panel agrees with the ACF result ($\mathrm{DM_{struct}} = 564.6 \pm 0.6\,\mathrm{pc\,cm^{-3}}$), however the two sub-pulses are not visible in the frequency-averaged profile. At $\mathrm{DM_{struct}} = 563.6\,\mathrm{pc\,cm^{-3}}$ the sub-pulses are distinct and have a downward frequency drift. (c) Burst 10. The first panel agrees with the ACF result ($\mathrm{DM_{struct}} = 563.3 \pm 0.4\,\mathrm{pc\,cm^{-3}}$). In this case, there are two sub-bursts. In the second panel, the lower burst sweeps under the upper burst. The appearance of two sub-bursts may, however, be caused by the missing frequency bands at ∼1250 MHz.

Table 4.3: Based on Table 3 of Platts et al. (2021). Pulse pairs observed in FRBs. Where bursts are from repeaters, the burst name for the individual burst (given in italics) follows the naming convention of the relevant paper. If there is no convention, the name corresponds to the observation number X in the relevant paper as BX. Apparently one-off FRBs are named as per usual.

FRB	Separation (ms)	Type	Reference
FRB 121102:			
GB 1/2	∼37	post	Scholz et al. (2017)
B10/11	∼34	pre	Hardy et al. (2017)
B35/36	∼26	post	Gourdji et al. (2019)
B20/21	∼38	post	Cruces et al. (2021)
Burst 2	∼17	pre	Rajwade et al. (2020a)
Burst 03	∼28	pre	Caleb et al. (2020); Platts et al. (2021)
Burst 05	∼34	pre	Caleb et al. (2020); Platts et al. (2021)
FRB 180916.J0158+65:			
181019	∼60	post	Andersen et al. (2019)
191219A/B	∼60	pre	Chawla et al. (2020); Amiri et al. (2020)
200620	∼90	post	Marthi et al. (2020)
FRB 190212.J18+81:			
190213	∼19	post	Fonseca et al. (2020)
FRB 200428:			
B1/2	∼29	pre	Bochenek et al. (2020a); Andersen et al. (2020)
FRB 181112	∼0.5	post	Prochaska et al. (2019); Cho et al. (2020)
FRB 190102	∼0.1	pre	Day et al. (2020)
FRB 190611	∼0.7	post	Day et al. (2020)

4.4.4 Pulse Pairs

Bursts 03 and 05 raise two main topics of discussion: i) the precursors of the main pulses; and ii) the apparent deviation from the characteristic arrival time $\Delta t \sim \nu^{-2}$.

4.4.4.1 *Precursors*

Bursts 03 and 05 each comprise a faint precursor pulse followed by a bright main pulse, with separation times of ∼28 ms and ∼34 ms, respectively. Similar behaviour has been observed in FRB 121102 before. Precursors have been detected by the Effelsberg radio telescope (∼34 ms separation; Hardy et al., 2017) and by the Lovell telescope (∼17 ms separation; Rajwade et al., 2020a); and postcursors have been detected by the Green Bank telescope (∼37 ms separation; Scholz et al., 2017), the Arecibo telescope (∼26 ms separation; Gourdji et al., 2019) and by the Effelsberg telescope (∼38 ms separation; Cruces et al., 2021). Gajjar et al. (2018) and Gourdji et al. (2019) report bursts separations of just ∼2 ms and ∼9 ms, respectively, however it is unclear whether the pulses are sub-bursts or a distinct pair of bursts: pulse pairs are distinguished from sub-bursts by their lack of an emission bridge between them (e.g. Day et al., 2020). Pulse pairs are not unique to FRB 121102: they have been observed in both repeating and apparently non-repeating FRBs. Table 4.3 provides a summary of these observations.

If FRB 200428 is a repeater (as suggested by Kirsten et al., 2020), the waiting time between the pulse pairs of apparently one-off bursts appear to be significantly shorter than those of repeaters. This could be random chance, however, due to the small sample size.

For a neutron star origin, if the source is actively emitting for the duration of a rotation period, then one may occasionally observe both pre- and postcursor bursts. Whether or not pulse pairs arise from independent events, however, is currently under debate. For example, Cruces et al. (2021) suggest that pulse pairs are broad bursts with only two resolvable components. It is also possible that the precursors are echoes of the main pulses caused by lensing. To determine this, however, one requires the burst polarisation properties (e.g. Main et al., 2017).

To help determine whether or not the pulses are independent, we attempted to calculate $\mathrm{DM_{struct}}$ for the precursors of bursts 03 and 05. The former could not be resolved and the latter was found to be $\sim$1$-$2 pc cm^{-3} higher than the main pulse ($\mathrm{DM_{struct}} = 566.0 \pm 0.4$ pc cm^{-3} for the precursor versus $\mathrm{DM_{struct}} = 564.5 \pm 0.3$ pc cm^{-3} for the main pulse). This relatively large difference in $\mathrm{DM_{struct}}$ may suggest the bursts are indeed independent, but other effects, such as lensing, cannot be ruled out.

The association of FRB 200428 with Galactic magnetar SGR 1935+2154 afforded Simard & Ravi (2020) the unique opportunity to study the FRB pulse pair in relation to the progenitor NS.[6] The spectral variation between pulses is consistent with scintillation arising from the SNR, which allowed for the motion of the magnetar emission region to be constrained. If the bursts are independent, the spatial separation between them would be 8.3×10^4 m. If the bursts are released from the same emission region, the source would have an apparent superluminal transverse motion of $V_{\mathrm{src,app}} \geq 9.5c$. This implies the bursts are more likely independent events. Unfortunately, this analysis cannot be broadly applied to other FRBs since scintillation is not observed in many extragalactic FRBs and no other FRBs have definitively been associated with a magnetar. Simard & Ravi (2020) do, however, apply the analysis to FRB 190611 (which has similar scintillation) by assuming a magnetar origin in a SNR with a $\sim$16 pc radius. A conclusion of independent bursts is reached in this case, too.

One can also compare the duration between bursts to the duration of the longest single burst to determine whether sustained activity from the same emission region is likely. In the case of FRB 121102, the duration between pulse pairs ranges from 19 ms to 38 ms (Rajwade et al., 2020a; Cruces et al., 2021, respectively), and the longest single multi-component burst lasts $\sim$39 ms (pulse B31; Cruces et al., 2021). It is thus possible that the bursts in the pulse pairs of FRB 121102 are emitted within the same burst envelope. Should this be the case, burst 03 would be an example of upward frequency drift. Currently, however, this cannot be confirmed nor ruled out.

4.4.4.2 *Apparent Change in Behaviour*

The main pulses of bursts 03 and 05 each have a kink in their tails at $\sim$1210 MHz, which may indicate a deviation from the standard $\Delta t \sim \nu^{-2}$ relationship (Figures 4.8a and 4.8b). We calculated $\mathrm{DM_{struct}}$ for the pulse above and below the kinks by dividing the frequency band at 1210 MHz. We found that the lower frequency bands have $\mathrm{DM_{struct}}$ values that are $\sim$1$-$2 pc cm^{-3} lower than the higher frequency bands. Specifically, for burst 03, the lower frequency region has $\mathrm{DM_{struct}} = 564.7 \pm 0.7$ pc cm^{-3} and the higher frequency region has $\mathrm{DM_{struct}} = 567.1 \pm 0.5$ pc cm^{-3}; and for burst 05, the lower frequency region has $\mathrm{DM_{struct}} = 563.3 \pm 0.2$ pc cm^{-3} and the higher frequency region has $\mathrm{DM_{struct}} = 565.3 \pm 0.2$ pc cm^{-3}. This may indicate a deviation from the ν^{-2} law. On the other hand, it is possible that correctly de-dispersing the lower frequency parts of the bursts may give the most representative DM, even though that component is not dominant over the observed bandwidth. In this case, the upper part of the bursts would comprise unresolved downward drifting sub-bursts. In support of this scenario, the lower DM values are more in line with other bursts in the sample and with the previously reported DM values for FRB 121102 (Hessels et al., 2019; Josephy et al., 2019; Oostrum et al., 2020; Majid et al., 2020).

Interestingly, there is a differential DM of $\sim$1 pc cm^{-3} between the main bursts of burst 03 and 05, as illustrated by their near-identical shapes at the DMs depicted in Figures 4.8a and 4.8b. This further highlights the challenges in determining an average or representative DM for an epoch—there may be no single DM that best describes all bursts in a sample, and it is difficult to isolate genuine changes in DMs between bursts.

An apparent deviation from the standard $\Delta t \sim \nu^{-2}$ relationship can be explained by a number of phenomena. As discussed in §1.4.1, the arrival time of FRBs travelling through a dense, magnetised plasma also depends on the Faraday RM and the emission measure. In regions with sufficiently strong magnetic fields, Faraday rotation may cause an notable $\Delta t \sim \nu^{-3}$ delay at low frequencies (e.g. Li et al., 2019b; Vedantham & Ravi, 2019). Unfortunately, polarisation information is not

[6] Note that the bright bursts reported by Kirsten et al. (2020) are separated by 1.4 s, which is shorter than the 3.2 s rotational period of SGR 1935+2154.

available for our FRB sample, and we were unable to investigate further.

Another possible cause of deviation from the $\Delta t \sim \nu^{-2}$ relationship is pulsar lensing. A detailed discussion by R. Main is given in Section 4.4.3 of Platts et al. (2021). In summary, we found that the local environment of the FRB is likely incompatible with the required lens. The host galaxy, however, may provide sufficient material to create the necessary lensing. Cordes et al. (2017) show that caustics in a host galaxy may cause a change in DM of $\sim$1 pc cm^{-3} with a $\sim$10 ms time delay. In our case, the observed delays in bursts 03 and 05 may be formed by a Gaussian lens with a 10 AU width.

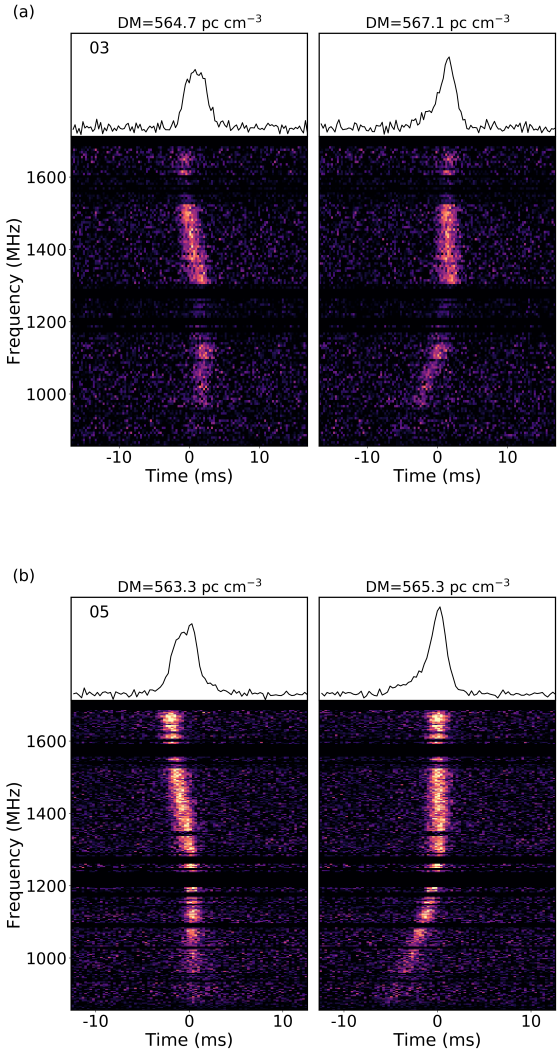

Figure 4.8: Based on Figures 8 and 9 of Platts et al. (2021). The resolution of the spectra are decimated to 256 channels. (a) Burst 03 and (b) burst 05 de-dispersed to the structure-optimised DMs given by frequency bands below (first panels) and above (second panels) 1210 MHz.

4.4.5 Frequency Drift

Downward drifting substructure appears to be a common feature in repeating FRBs (e.g. Andersen et al., 2019; Hessels et al., 2019; Fonseca et al., 2020). In Paper I, Caleb et al. (2020) used the structure-optimised DMs reported in Platts et al. (2021) to characterise the drift-rates of the pulses in the sample using a 2D ACF method. The drift rates were found to be consistent with other published bursts with frequency ranges between 600−6500 MHz, with a slope of $\alpha = -0.147 \pm 0.014\,\mathrm{ms}^{-1}$. Upward drifting substructure, however, has yet to be definitively observed in an FRB. Tentative cases of upward drift exist in some pulse pairs, for example burst 03.

As shown in the second panel of Figure 4.4, the faint precursor is between ∼1000−1200 MHz and the main pulse is between ∼1000−1700 MHz. Other pulse pairs with potential upward frequency drift are observed in FRB 180916.J0158+65 (∼60 ms separation; Amiri et al., 2020; Chawla et al., 2020), FRB 190611 (∼0.7 ms separation; Day et al., 2020) and FRB 200428 (∼29 ms separation; Bochenek et al., 2020a; Andersen et al., 2020).

Plasma lensing is a possible cause of frequency drift, and can successfully account for the intermittency and timescale of variation in FRB spectral features (Cordes et al., 2017; Hessels et al., 2019). Cordes et al. (2017) show this via example by considering one-dimensional plasma structures in the host galaxy of FRB 121102. The multiple spectral peaks observed in FRBs may also be explained by lensing, for example the delayed copies—or echoes—observed in the Crab pulsar can be attributed to plasma lensing by filamentary structures in its nebula. Further, Main et al. (2018) report extreme lensing in the "Black Widow" pulsar, and draw similarities between the resultant frequency structures and those of FRB 121102. The predominance of downward frequency drifts in repeating FRBs, however, presents a conundrum. Should the drift be caused by lensing, one would expect to observe downward and upward frequency drift due to changes in the viewing geometry. One would thus require a single dominant lens—a feature that has yet to be observed in pulsars (Hessels et al., 2019).

The predominance of downward drifting substructure in repeating FRBs may be intrinsic to the emission mechanism. Radius-to-frequency mapping (e.g. Thorsett, 1992), where frequencies are radiated preferentially at different altitudes from the surface of a NS, is one possible explanation (Lyutikov, 2020). Here, assuming a NS origin (e.g. Popov & Postnov, 2013; Beloborodov, 2017; Lyubarsky, 2020), emission near the surface of the star is at a higher frequency than emission further out. Pulsar-like sparking and cosmic comb models also predict a downward frequency drift (Wang et al., 2019, 2020b), where bunches of charged particles stream outwards from the inner region of the magnetosphere (e.g. Popov & Postnov, 2013; Yang & Zhang, 2018; Lu et al., 2020a; Kumar & Bošnjak, 2020; Wang et al., 2020b). Emission observed at earlier times is emitted from further along the field lines, where the lines are more curved and hence radiation is at a higher frequency. Another possibility is that radiative processes (i.e. the release of FRB emission) near the NS surface decrease the Lorentz factor of electrons (Gu et al., 2020). Since the characteristic frequency of curvature radiation ν_c is proportional to γ^3, lower energy emission may be released at later times. Flare models also predict downward drifting substructure, where the Lorentz factor of the shocked gas decreases as the blast wave decelerates and the optical depth of the upstream medium decreases (Metzger et al., 2019).

4.5 Final Thoughts

The complex and varied substructure of FRB 121102 holds valuable clues about its origins. Ongoing follow-up observations will help to identify which structures are intrinsic to the emission mechanism and which are due to propagation effects. The MeerKAT data presented in Caleb et al. (2020) is unfortunately lacking polarisation information, and thus the analysis in Platts et al. (2021) only focused on the DM. Polarisation information would have offered valuable insight, and may have helped clarify the cause of deviation from the standard $\Delta t \sim \nu^{-2}$ relationship observed in bursts 03 and 05. Michilli et al. (2018b) and Day et al. (2020), for example, provide detailed analyses of the polarisation properties and their implications for FRB 121102 (and other FRBs).

We found the average structure-optimised DM of FRB 121102 to be consistent with 2018 and 2019 observations. Together with findings by Hessels et al. (2019), this suggests the DM has been increasing for the past 7 years. We note, however, that our burst sample is small, and thus may not be truly representative of the epoch. In the case of a NS origin, an increasing or constant DM may be caused if the nebula expands into a high density ISM (Yang & Zhang, 2017; Piro & Gaensler, 2018); if the remnant star is young and drives the expansion of ionised gas into an HII region (Yang & Zhang, 2017); or if the radiation from the shock in a magnetar flare model photoionises neutral gas ahead of the burst (Margalit & Metzger, 2018). The FRB source may also be rapidly moving deeper into an HII region (Yang & Zhang, 2017). If in the future the DM is observed to decrease, the change may be attributed to lensing in the host galaxy.

Two of the bursts are closely separated pulse pairs (bursts 03 and 05), where the leading pulse is significantly fainter than the main pulse. Whether the pairs are emitted within the same burst envelope or not is uncertain. The time difference between bursts is comparable to the longest reported burst from FRB 121102 ($\sim$39 ms; Cruces et al., 2021), which implies it is possible they were formed by the same event. The precursors may also be echoes caused by lensing, but unfortunately we could not explore this possibility without the bursts' polarisation information.

The main pulses of bursts 03 and 05 appear to deviate from the standard $\Delta t \sim \nu^{-2}$, as evidenced by a kink in their tails at $\sim$1210 MHz. The DMs are found to be $\sim 1-2\,\mathrm{pc\,cm^{-3}}$ higher in the lower frequency bands compared to the higher frequency bands. We showed that lensing in the host galaxy may account for this. Alternatively, it may be caused by Faraday delay. It is also possible that the effect is due to insufficient resolution—the burst may be composed of unresolved sub-bursts that drift down in frequency.

Finally, we urge caution when calculating the structure-optimised DM. There may be no DM that truly represents the burst at inception (e.g. when the time-frequency relationship of a burst deviates from the standard $\Delta t \sim \nu^{-2}$). This is true of sub-bursts, where propagation effects influence each sub-burst differently (e.g. where sub-bursts do not align). Further, the DM may be ambiguous. For burst 07, for example, it is difficult to say with any certainty which DM value provides the most representative view of the pulse (Figure 4.7a). Supplementary information, such as polarisation properties and rotation measures, are therefore very valuable when performing these types of analyses.

CHAPTER 5

In Closing

In this thesis, we have investigated the quickly evolving world of Fast Radio Bursts (FRBs). Speculation has painted these mysterious signals as everything from RFI to aliens, but slowly a picture of their true origin is coming into view. To date, 137[1] FRBs have been published; 22 of which have been observed to repeat and 13 of which have been localised to host galaxies. One FRB has been associated with a Galactic magnetar, which implies that at least some FRBs have NS progenitors. Chapter 1 gives an introduction to FRBs and provides some theoretical background. Chapter 2 reviews FRB characteristics and progenitor models. The broad range of observed properties—such as repetition, repetition rates, periodicity, and pulse structure—complicates the task of building a unified model, and it may yet be found that multiple FRB populations exist.

Chapter 3 presents a novel way in which one can use the DM of radio transients to measure the baryonic density of the Milky Way Galactic halo (first presented in Platts et al., 2020). We used a non-parametric technique to constrain the contribution of the MW halo to the total observed DM for pulsars and FRBs. By constructing PDFs of the observed DMs and subtracting off the ISM component using NE2001 and YMW16 electron density estimation models, we were able to find a lower limit from pulsar data (given by the maximum of the pulsar PDF) and an upper limit from FRB data (given by the minimum of the FRB PDF). We tried two methods to model the PDFs: Density Estimation using Field Theory (DEFT) and kernel density estimation (KDE). The dearth of FRB data led us to first consider DEFT, which was specifically developed for the small data regime. While DEFT performed well for the pulsar data, the boundary at DM $= 0\,\mathrm{pc\,cm^{-3}}$ led to edge effects in the FRB PDF. Further, DEFT was unable to recognise the sharp leading edge of the FRB PDF and thus over-smoothed the region. KDE proved to be effective for both data sets, albeit in different forms. Standard KDE was applied to the pulsar data, and asymmetric variable bandwidth KDE was applied to the FRB data. The pulsar data has a smooth, continuous distribution, and hence standard KDE performed adequately. The FRB distribution, however, has a sharp leading edge and a lower bound at DM $= 0\,\mathrm{pc\,cm^{-3}}$. A single bandwidth for the kernels at each data point therefore either over-smooths the front of the distribution (which results in edge effects and incorrectly estimates the PDF structure) or over-fits the rest of the distribution. We implemented KDE using a gamma kernel with a varying bandwidth (e.g. Chen, 2000; Jeon & Kim, 2013; Hoffmann & Jones, 2015), where the gamma kernel ensured a positive distribution.

The pulsar analysis served primarily as a means to evaluate systematic uncertainties and select the most appropriate electron density model (NE2001 or YMW16) for the final results. This is because Galactic pulsars are not expected to extend into the MW halo (but see Rajwade et al., 2018). The FRB constraints are conservative, as they include a minimal contribution from the host galaxy and IGM. Using a latitude cut of $|b| > 20^\circ$ to decrease the systematic uncertainty associated with modelling the Galactic disk, the sample comprised 83 FRBs. The DM contribution of the halo (plus a minimal contribution from the IGM and host galaxy) was found to be $63^{+27}_{-21}\,(\mathrm{stat}) \pm 9\,(\mathrm{sys})$ with 1σ uncertainty. This corresponds to an upper limit of $\mathrm{DM_{MW,halo}} < 123\,\mathrm{pc\,cm^{-3}}$ with a 95% confidence level. By simulating the FRB DM distribution and applying the analysis to random samples of FRBs drawn from the distribution, we show that the constraints are expected to become significantly tighter for a higher number of FRBs. Using a sample of 100 FRBs, we found a 1σ (statistical) uncertainty of $\pm 24\,\mathrm{pc\,cm^{-3}}$. For 10 000 FRBs, the uncertainty decreased to $\pm 2\,\mathrm{pc\,cm^{-3}}$. Even a sample of 1000 FRBs showed a significant improvement, with an uncer-

[1] All events; 118 of which are verified (FRBCAT; Petroff et al., 2016).

tainty of $\pm 7\,\mathrm{pc\,cm^{-3}}$. We are thus hopeful that once more FRBs are published (it is well known that CHIME/FRB, for example, has already detected close to 1000 FRBs), our model will provide constraints that complement other analyses.

With a few thousand FRBs, our model may be able to discern whether the Galaxy is likely to have retained the majority of its cosmic baryons ($\mathrm{DM_{MW,halo}} > 50\,\mathrm{pc\,cm^{-3}}$). At the very least, it will provide an informative (albeit conservative) measure of the MW halo. We did not address how the DM of the MW halo varies in different directions. In the future it may be possible to probe regions of the sky that contain a high number of FRBs. One could, for example, analyse a few square degrees of the sky at a time. This, however, is not expected to give strong constraints on the DM variation of the MW halo, because the estimate includes a minimal contribution from the IGM and host galaxy. Unless a significant number of FRBs are detected per region, the minimal DM of the IGM and host galaxy will vary depending on the region of the sky begin probed. The problem is further compounded by the relatively large systematic uncertainty associated with modelling the ISM ($\sim 8\,\mathrm{pc\,cm^{-3}}$).

Chapter 4 provides an analysis of the time-frequency structure of 10 bursts from FRB 121102 detected by the MeerKAT radio telescope in South Africa (bursts presented in Caleb et al., 2020; analysis presented in Platts et al., 2021). The wide contiguous bandwidth of the observations revealed interesting burst structures. Two of the bursts have small precursor pulses separated from the main pulses by ~ 28 ms and ~ 34 ms, respectively. The main pulses of these bursts appear to deviate from the standard time-frequency dispersion relationship $\Delta t \sim \nu^{-2}$. Two (possibly three) of the bursts have a bifurcating structure near the middle of the bandwidth at ~ 1250 MHz, and one of the bursts comprises two vertically-aligned sub-bursts. The remaining bursts are narrow, single pulses with no discernible substructure. Unfortunately, no polarisation data is available for the bursts, thus limiting the study to the dispersion. As such, we analysed the time-frequency structure by determining the structure-optimised DMs of the bursts.

Methodology by Gajjar et al. (2018) and Hessels et al. (2019) invokes the forward difference time derivative of the frequency-averaged pulse profile to maximise the structure of the burst with respect to the DM. We found that for our MeerKAT data the technique yielded ambiguous results because of the relatively coarse time-resolution of the telescope (306.24 µs; which is further reduced by dispersion smearing). Noting that fine structure in pulsar data has been studied for many years, we reflected back to a technique suitable for the coarse resolution of our data but generally applicable to higher resolution data: autocorrelation functions (ACFs; e.g. Cordes et al., 1990; Lange et al., 1998). Here, the widths of structures are determined by studying the shape of the ACFs of the frequency-averaged pulse profile at different DMs. The DM corresponding to the ACF that flattens earliest is that which minimises the pulse width, and hence maximises individual burst components. With this technique, we could calculate the structure-optimised DM for 10 out of the 11 available bursts. The first burst in the sample has a very low S/N and we could not establish a reliable result.

To check the performance and consistency of the ACF method, we compared results to those obtained using the recently developed `DM_phase` algorithm (Seymour et al., 2019; Seymour et al., *in prep*). Here, the structure-optimised DM is determined by maximising the coherent power spectrum of the frequency-averaged pulse profile. The results largely agree with those obtained via the ACF method. `DM_phase` was found to be more sensitive than ACF by revealing substructure in one of the bursts that was missed by the ACF method. `DM_phase` occasionally gave multiple values for the structure-optimised DM, at which point manual intervention is required to establish the most likely result. Otherwise, the algorithm is fully automated for a range of pulses. In its current form, the ACF method requires manual checks during the analysis for each pulse. The algorithm compares the gradient of the ACF at different points to find where the ACF first flattens. A local and non-local comparison is made over a number of bins. The value at which the difference between the gradients at each point becomes significant, however, varies from pulse to pulse: some ACFs have a more defined flattening point with a larger difference in gradients before and after the point. As such, we needed to adjust the sensitivity parameters that determine the gradient difference where flattening is deemed significant. Since the ACF method did not perform as well as `DM_phase`, we did not attempt to automate the parameter selection. To choose the parameters, one

requires knowledge of approximately where the flattening point is and how quickly the gradient changes about that point. To automate the process, one could potentially search for inflection points in the ACF and then define the degree of inflection that qualifies as "significant" flattening. Noise in the data would complicate this search, and one may have to smooth the data appropriately.

The average structure-optimised DM of the FRB sample was found to be $\mathrm{DM_{struct}} = 564.8 \pm 0.6\,\mathrm{pc\,cm^{-3}}$ and $\mathrm{DM_{struct}} = 564.4 \pm 0.6\,\mathrm{pc\,cm^{-3}}$ using the ACF method and `DM_phase`, respectively. This is an increase of $\sim 1{-}2\,\mathrm{pc\,cm^{-3}}$ since observations of FRB 121102 taken in 2018 (1 year prior; Josephy et al., 2019; Oostrum et al., 2020). Together with findings by Hessels et al. (2019), this suggests the DM of FRB 121102 has been increasing for at least 7 years. Progenitors consistent with this behaviour include FRBs with a NS origin whose SN ejecta expands into a high density ISM (Yang & Zhang, 2017; Piro & Gaensler, 2018) or an HII region (Yang & Zhang, 2017). In the magnetar flare model by Margalit & Metzger (2018), the photoionisation of neutral gas by the UV and X-ray radiation from the shock could also produce the observed DM increase. Alternatively, the FRB source may be rapidly moving through an HII region, for instance due to a SN kick (Yang & Zhang, 2017). The increase may also be due to lensing, in which case the DM should decrease in the future as the lens geometry and alignment changes. Continued monitoring of FRB 121102 will reveal whether this is occurs.

One of the most striking features noted in the sample is an apparent deviation from the standard $\Delta t \sim \nu^{-2}$ relationship observed in two of the pulses. The main pulses of bursts 03 and 05 tilt abruptly to the left at $\sim$1250 MHz. A differential DM of $1{-}2\,\mathrm{pc\,cm^{-3}}$ was found between the upper and lower frequency region of the bursts, split at the kink. A major caveat, however, is that the effect may be due to insufficient resolution. Should the effect be genuine, it could be due to plasma lensing in the host galaxy or due to Faraday rotation, where the dispersion goes as $\Delta t \sim \nu^{-3}$. Unfortunately, no polarisation data is available to explore possible Faraday delay. The sub-bursts of bursts 07 and 11 also have differential DMs of $\sim 1\,\mathrm{pc\,cm^{-3}}$ and $\sim 2\,\mathrm{pc\,cm^{-3}}$, respectively. It is possible that the bursts are multiply imaged by plasma lensing, which can account for a DM difference of up to $\sim 1\,\mathrm{pc\,cm^{-3}}$ between sub-bursts. The change in DM is too large to be attributed to different viewing angles through a nebula or different emission regions in the magnetosphere of a NS.

The sample includes two pulse pairs (bursts 03 and 05). Similar pairs have been observed in FRB 121102 and other FRBs numerous times, but whether or not such bursts are emitted within the same burst envelope is currently unknown. The bursts may be one extended burst with only two resolvable peaks, they may be two independent events, or they may be related events emitted from the same region. The bursts may also be echoes caused by plasma lensing, as observed in Galactic pulsars (e.g. Michilli et al., 2018a). To determine whether the bursts are independent, one might compare the duration of a single pulse to the emission time of the burst pair. In the case of FRB 121102, the longest duration for a single pulse is 39 ms (Cruces et al., 2021), which is comparable to the total duration of the observed pulse pairs. It is thus possible the events are related, but this is purely speculative.

FRB pulses have a variety of different structures that may be intrinsic to the emission mechanism or caused by propagation effects. Careful study of the structure allows one to gradually tease apart the different effects, allowing one to probe the environment of the FRB (local and galactic) and the origin of the FRB emission itself. Polarisation information is a valuable diagnostic when determining the cause of structure. Currently MeerTRAP is not equipped to record the polarisation data from MeerKAT, but the pulsar processor (PTUSE) on MeerKAT is (Bailes et al., 2020). Thus follow up observations by MeerKAT will be capable of coherently de-dispersing the data and doing polarimetry.

In closing, FRBs have inspired new science from a range of disciplines and have proven to be useful probes of the Universe around us. While we appear to be slowly honing in on their true nature, there is still much to be done and much to be learnt. We have thousands of FRB detections to look forward to in the coming years from telescopes such as CHIME/FRB, the South African Hydrogen Intensity and Real-time Analysis eXperiment (HIRAX), the Chinese Five-hundred-meter Aperture Spherical radio Telescope (FAST), and the full SKA. With FRBs, the future certainly is bright.

Final Acknowledgements

I am supported by a PhD fellowship from the National Institute of Theoretical Physics (NITheP) and a South African L'Oréal-UNESCO For Women in Science Young Talents grant. Thank you very much to these organisations for the support and for this opportunity.

Figure 1.1 makes use of FRB observations taken with the Parkes Radio Telescope: "Fast Radio Bursts: Parkes Data" (PI: Keane) http://researchdata.ands.org.au/fast-radio-bursts-parkes/468266.

Chapter 4 makes use of data taken by the MeerKAT telescope, which is operated by the South African Radio Astronomy Observatory (SARAO)—a facility of the National Research Foundation (NRF) of the Department of Science and Innovation (DSI).

Acronyms

ACF autocorrelation function

AGN active galactic nuclei

AIC accretion induced collapse

AQN axion quark nugget

AXP anomalous X-ray pulsar

BH black hole

BNS binary neutron star

BPT Baldwin-Phillips-Terlevich

CC-SN core-collapse supernova

CGM circumgalactic medium

CHIME/FRB Canadian Hydrogen Intensity Mapping Experiment

CMB cosmic microwave background

DEFT Density Estimation using Field Theory

DM dispersion measure

DSPSR Digital Signal Processing Software for Pulsar Astronomy

DSR Dicke's superradiance

EM electromagnetic

$\mathbf{e^+e^-}$ electron-positron

FAST Five-hundred-meter Aperture Spherical radio Telescope

FFT fast Fourier transform

FRB Fast Radio Burst

GEV generalised extreme value

GRB gamma-ray burst

GW gravitational wave

HIRAX Hydrogen Intensity and Real-time Analysis eXperiment

HMXB high-mass X-ray binary

HTRU High Time Resolution Universe

ICM intra-cluster medium

IGM intergalactic medium

IR infrared

ISM interstellar medium

KBH Kerr black hole

KDE kernel density estimation

KNBH Kerr-Newman black hole

KS Kolmogorov–Smirnov

LGRB long-duration gamma-ray burst

LINER low-ionization nuclear emission-line region

LMC Large Magellanic Cloud

LMXB low-mass X-ray binary

LSD large superconducting dipole

MAP maximum *a posteriori*

MeerKAT Meer Karoo Array Telescope

MeerTRAP Meer TRAnsients and Pulsars

MISE mean integrated squared error

MW Milky Way

MWN magnetar wind nebula

NS neutron star

PBH primordial black hole

PDF probability density function

PWN pulsar wind nebula

QED quantum electrodynamics

QN quark-nova

QSO quasi-stellar object

RDM radial dark matter flow

RFI radio frequency interference

RM rotation measure

S/N signal-to-noise

SARAO South African Radio Astronomy Observatory

SCS superconducting cosmic string

SFR star-formation rate

SGR soft gamma-ray repeater

sGRB short-duration gamma-ray burst

SKA Square Kilometre Array

SLSN superluminous supernova

SMBH supermassive black hole

SN supernova

SNR supernova remnant

SQM strange quark matter

SS strange star

SZ Sunyaev-Zel'dovich

TOP Turn-Off Point

UV ultra-violet

VLA Very Large Array

WD white dwarf

WH white hole

References

Abbott B. P., et al., 2017a, Physical Review Letters, 119, 161101

Abbott B. P., et al., 2017b, Astrophysical Journal, 848, L13

Abbott B. P., et al., 2020, Astrophysical Journal, 892, L3

Abramowicz M. A., Becker J. K., Biermann P. L., Garzilli A., Johansson F., Qian L., 2009, Astrophysical Journal, 705, 659

Abramowicz M. A., Bejger M., Wielgus M., 2018, Astrophysical Journal, 868, 17

Acciari V. A., et al., 2018, Monthly Notices of the Royal Astronomical Society, 481, 2479

Ai S., Gao H., Zhang B., 2020, arXiv e-prints, p. arXiv:2007.02400

Albrecht A., Battye R. A., Robinson J., 1997, Physical Review Letters, 79, 4736

Alcock C., Farhi E., Olinto A., 1986, Astrophysical Journal, 310, 261

Ali-Haïmoud Y., Kamionkowski M., 2017, Physical Review D, 95, 043534

Alpar M. A., 2001, Astrophysical Journal, 554, 1245

Alpar M. A., Cheng A. F., Ruderman M. A., Shaham J., 1982, Nature, 300, 728

Amato E., Arons J., 2006, Astrophysical Journal, 653, 325

Amiri M., et al., 2019, Nature, 566, 235

Amiri M., et al., 2020, Nature, 582, 351

Andersen B. C., et al., 2019, Astrophysical Journal Letters, 885, L24

Andersen B. C., et al., 2020, Nature, 587, 54

Anderson M. E., Bregman J. N., Dai X., 2013, Astrophysical Journal, 762, 106

Andreoni I., et al., 2017, Publications of the Astronomical Society of Australia, 34, e069

Armillotta L., Fraternali F., Werk J. K., Prochaska J. X., Marinacci F., 2017, Monthly Notices of the Royal Astronomical Society, 470, 114

Arvanitaki A., Dubovsky S., 2011, Physical Review D, 83, 044026

Arvanitaki A., Dimopoulos S., Dubovsky S., Kaloper N., March-Russell J., 2010, Physical Review D, 81, 123530

Baade W., Zwicky F., 1934, Proceedings of the National Academy of Science, 20, 254

Backer D. C., Wong T., Valanju J., 2000, Astrophysical Journal, 543, 740

Bagchi M., 2017, Astrophysical Journal Letters, 838, L16

Bagchi M., Nieves A. C., McLaughlin M., 2012, Monthly Notices of the Royal Astronomical Society, 425, 2501

Bai Y., Hamada Y., 2018, Physics Letters B, 781, 187

Bailes M., et al., 2020, Publications of the Astronomical Society of Australia, 37, e028

Baldwin J. A., Phillips M. M., Terlevich R., 1981, Publications of the Astronomical Society of the Pacific, 93, 5

Bannister K. W., Madsen G. J., 2014, Monthly Notices of the Royal Astronomical Society, 440, 353

Bannister K. W., et al., 2019, Science, 365, 565

Barceló C., Carballo-Rubio R., Garay L. J., 2014, International Journal of Modern Physics D, 23, 1442022

Bardeen J. M., Petterson J. A., 1975, Astrophysical Journal Letters, 195, L65

Bardeen J. M., Press W. H., Teukolsky S. A., 1972, Astrophysical Journal, 178, 347

Baring M. G., Harding A. K., 2007, Astrophysics and Space Science, 308, 109

Barrau A., Rovelli C., Vidotto F., 2014, Physical Review D, 90, 127503

Barrau A., Moulin F., Martineau K., 2018, Physical Review D, 97, 066019

Barton A., Brandenberger R. H., Lin L., 2015, Journal of Cosmology and Astroparticle Physics, 2015, 022

Bassa C. G., et al., 2017, Astrophysical Journal Letters, 843, L8

Bastian T. S., Bookbinder J., Dulk G. A., Davis M., 1990, Astrophysical Journal, 353, 265

Belczynski K., Bulik T., Rudak B., 2002, Astrophysical Journal, 571, 394

Beloborodov A. M., 2012, Astrophysical Journal, 762, 13

Beloborodov A. M., 2017, Astrophysical Journal Letters, 843, L26

Beloborodov A. M., 2020, Astrophysical Journal, 896, 142

Beloborodov A. M., Thompson C., 2007, Astrophysical Journal, 657, 967

Ben Achour J., Brahma S., Mukohyama S., Uzan J. P., 2020, Journal of Cosmology and Astroparticle Physics, 2020, 020

Beniamini P., Hotokezaka K., van der Horst A., Kouveliotou C., 2019, Monthly Notices of the Royal Astronomical Society, 487, 1426

Beniamini P., Wadiasingh Z., Metzger B. D., 2020, Monthly Notices of the Royal Astronomical Society, 496, 3390

Berger E., 2008, Astrophysical Journal, 690, 231

Berger E., f. Fong W., Chornock R., 2013, Astrophysical Journal, 774, L23

Bergeron J., 1986, Astronomy and Astrophysics, 155, L8

Bhandari S., et al., 2018, Monthly Notices of the Royal Astronomical Society, 475, 1427

Bhandari S., et al., 2020, Astrophysical Journal, 895, L37

Bhattacharya D., 1995, Journal of Astrophysics and Astronomy, 16, 217

Bhattacharya D., van den Heuvel E. P. J., 1991, Physics Reports, 203, 1

Bhattacharyya S., 2017, arXiv e-prints, p. arXiv:1711.09083

Bialek W., Callan C. G., Strong S. P., 1996, Physical Review Letters, 77, 4693

Bietenholz M. F., Bartel N., 2017, Astrophysical Journal, 851, 124

Bildsten L., Cutler C., 1992, Astrophysical Journal, 400, 175

Blaes O., Blandford R., Goldreich P., Madau P., 1989, Astrophysical Journal, 343, 839

Blanchard P. K., Berger E., Fong W.-f., 2016, Astrophysical Journal, 817, 144

Blandford R. D., Znajek R. L., 1977, Monthly Notices of the Royal Astronomical Society, 179, 433

Blandford R. D., McKee C. F., Rees M. J., 1977, Nature, 267, 211

Blandford R., Meier D., Readhead A., 2019, Annual Review of Astronomy and Astrophysics, 57, 467

Bloom J. S., Kulkarni S. R., Djorgovski S. G., 2002, Astronomical Journal, 123, 1111

Bochenek C. D., Ravi V., Dong D., 2020a, arXiv e-prints, p. arXiv:2009.13030

Bochenek C. D., Ravi V., Belov K. V., Hallinan G., Kocz J., Kulkarni S. R., McKenna D. L., 2020b, Nature, 587, 59

Bodmer A. R., 1971, Physical Review D, 4, 1601

Bombaci I., 1996, Astronomy and Astrophysics, 305, 871

Booth C. M., Schaye J., Delgado J. D., Dalla Vecchia C., 2012, Monthly Notices of the Royal Astronomical Society, 420, 1053

Bostick W. H., 1956, Physical Review, 104, 292

Bower G. C., Wright M. C. H., Falcke H., Backer D. C., 2003, Astrophysical Journal, 588, 331

Boylan-Kolchin M., Bullock J. S., Sohn S. T., Besla G., van der Marel R. P., 2013, Astrophysical Journal, 768, 140

Bradt H. V. D., McClintock J. E., 1983, Annual Review of Astronomy and Astrophysics, 21, 13

Bramberger S. F., Brandenberger R. H., Jreidini P., Quintin J., 2015, Journal of Cosmology and Astroparticle Physics, 2015, 007

Brandenberger R. H., 1987, Nuclear Physics B, 293, 812

Brandenberger R. H., Sornborger A. T., Trodden M., 1993, Physical Review D, 48, 940

Brandenberger R., Cyr B., Varna Iyer A., 2017, arXiv e-prints, p. arXiv:1707.02397

Bregman J. N., Anderson M. E., Miller M. J., Hodges-Kluck E., Dai X., Li J.-T., Li Y., Qu Z., 2018, Astrophysical Journal, 862, 3

Buckley J. H., Bhupal Dev P. S., Ferrer F., Huang F. P., 2020, arXiv e-prints, p. arXiv:2004.06486

Burchett J. N., et al., 2019, Astrophysical Journal Letters, 877, L20

Burgess J. M., Bégué D., Greiner J., Giannios D., Bacelj A., Berlato F., 2020, Nature Astronomy, 4, 174

Burke-Spolaor S., Bailes M., Ekers R., Macquart J.-P., Crawford Fronefield I., 2011, Astrophysical Journal, 727, 18

Burles S., Tytler D., 1996, Astrophysical Journal, 460, 584

Cai Y.-F., Sabancilar E., Vachaspati T., 2012a, Physical Review D, 85, 023530

Cai Y.-F., Sabancilar E., Steer D. A., Vachaspati T., 2012b, Physical Review D, 86, 043521

Caleb M., et al., 2018, Monthly Notices of the Royal Astronomical Society, 478, 2046

Caleb M., Stappers B. W., Rajwade K., Flynn C., 2019, Monthly Notices of the Royal Astronomical Society, 484, 5500

Caleb M., et al., 2020, Monthly Notices of the Royal Astronomical Society, 496, 4565

Camilo F., et al., 2018, Astrophysical Journal, 856, 180

Carr B. J., 1975, Astrophysical Journal, 201, 1

Cerutti B., Beloborodov A. M., 2017, Space Science Reviews, 207, 111

Chamma M. A., Rajabi F., Wyenberg C. M., Mathews A., Houde M., 2020, arXiv e-prints, p. arXiv:2010.14041

Champion D. J., et al., 2016, Monthly Notices of the Royal Astronomical Society, 460, L30

Chandra P., Frail D. A., 2012, Astrophysical Journal, 746, 156

Chandrasekhar S., 1957, An introduction to the study of stellar structure.. University of Chicago Press

Charnock T., Avgoustidis A., Copeland E. J., Moss A., 2016, Physical Review D, 93, 123503

Chatterjee S., Cordes J. M., 2004, Astrophysical Journal Letters, 600, L51

Chatterjee P., Hernquist L., Narayan R., 2000, Astrophysical Journal, 534, 373

Chatterjee S., et al., 2009, Astrophysical Journal, 698, 250

Chatterjee S., et al., 2017, Nature, 541, 58

Chawla P., et al., 2020, Astrophysical Journal Letters, 896, L41

Chen S. X., 2000, Annals of the Institute of Statistical Mathematics, 52, 471

Chen W.-C., 2020, Publications of the Astronomical Society of Japan, 72, L8

Chen H.-W., Lanzetta K. M., Webb J. K., 2001, Astrophysical Journal, 556, 158

Chen W.-C., Tareen A., Kinney J. B., 2018, Physical Review Letters, 121, 160605

Chen G., Ravi V., Lu W., 2020, Astrophysical Journal, 897, 146

Cheng M.-Y., Fan J., Marron J. S., 1997, The Annals of Statistics, 25, 1691

Cheng Y., Zhang G. Q., Wang F. Y., 2020, Monthly Notices of the Royal Astronomical Society, 491, 1498

Chernoff D. F., Tye S. H. H., 2015, International Journal of Modern Physics D, 24, 1530010

Chernoff D. F., Li S. Y., Tye S. H. H., 2020, arXiv e-prints, p. arXiv:2003.07275

Chittidi J. S., et al., 2020, arXiv e-prints, p. arXiv:2005.13158

Cho H., et al., 2020, Astrophysical Journal Letters, 891, L38

Cline T. L., et al., 1980, Astrophysical Journal Letters, 237, L1

Colaiuda A., Kokkotas K. D., 2011, Monthly Notices of the Royal Astronomical Society, 414, 3014

Colgate S. A., Petschek A. G., 1981, Astrophysical Journal, 248, 771

Collazzi A. C., et al., 2015, Astrophysical JournalSupplement Series, 218, 11

Cong K., Zhang Q., Wang Y., Noe G. T., Belyanin A., Kono J., 2016, J. Opt. Soc. Am. B, 33, C80

Connor L., Sievers J., Pen U.-L., 2016a, Monthly Notices of the Royal Astronomical Society, 458, L19

Connor L., Pen U.-L., Oppermann N., 2016b, Monthly Notices of the Royal Astronomical Society, 458, L89

Contaldi C., Hindmarsh M., Magueijo J., 1999, Physical Review Letters, 82, 2034

Cooke R. J., Pettini M., Steidel C. C., 2018, Astrophysical Journal, 855, 102

Cordes J. M., 1978, Astrophysical Journal, 222, 1006

Cordes J. M., Chatterjee S., 2019, Annual Review of Astronomy and Astrophysics, 57, 417

Cordes J. M., Lazio T. J. W., 2002, arXiv e-prints, pp astro–ph/0207156

Cordes J. M., Lazio T. J. W., 2003, arXiv e-prints, pp astro–ph/0301598

Cordes J. M., Wasserman I., 2016, Monthly Notices of the Royal Astronomical Society, 457, 232

Cordes J. M., Weisberg J. M., Hankins T. H., 1990, Astrophysical Journal, 100, 1882

Cordes J. M., Wasserman I., Hessels J. W. T., Lazio T. J. W., Chatterjee S., Wharton R. S., 2017, Astrophysical Journal, 842, 35

Costa E., et al., 1997, Nature, 387, 783

Costa R., Gordin J. E. B., Weltman A., 2018, arXiv e-prints, p. arXiv:1807.01976

Cowling A., Hall P., 1996, Journal of the Royal Statistical Society. Series B (Methodological), 58, 551

Cowperthwaite P. S., et al., 2017, Astrophysical Journal Letters, 848, L17

Crawford F., Rane A., Tran L., Rolph K., Lorimer D. R., Ridley J. P., 2016, Monthly Notices of the Royal Astronomical Society, 460, 3370

Cruces M., et al., 2021, Monthly Notices of the Royal Astronomical Society, 500, 448

Dai Z. G., 2020, Astrophysical Journal Letters, 897, L40

Dai Z. G., Zhong S. Q., 2020, Astrophysical Journal Letters, 895, L1

Dai Z. G., Wang X. Y., Wu X. F., Zhang B., 2006, Science, 311, 1127

Dai X., Bregman J. N., Kochanek C. S., Rasia E., 2010, Astrophysical Journal, 719, 119

Dai Z. G., Wang J. S., Wu X. F., Huang Y. F., 2016, Astrophysical Journal, 829, 27

Dai Z. G., Wang J. S., Yu Y. W., 2017, Astrophysical Journal Letters, 838, L7

Damour T., Deruelle N., Ruffini R., 1976, Nuovo Cimento Lettere, 15, 257

Day C. K., et al., 2020, Monthly Notices of the Royal Astronomical Society, 497, 3335

DeLaunay J. J., et al., 2016, Astrophysical Journal Letters, 832, L1

Deng W., Zhang B., 2014, Astrophysical Journal Letters, 783, L35

Dennison B., 2014, Monthly Notices of the Royal Astronomical Society: Letters, 443, L11

Dermer C. D., Atoyan A., 2003, Physical Review Letters, 91, 071102

Desvignes G., et al., 2018, Astrophysical Journal Letters, 852, L12

Detweiler S., 1980, Physical Review D, 22, 2323

Dicke R. H., 1954, Physical Review, 93, 99

Dionysopoulou K., Alic D., Palenzuela C., Rezzolla L., Giacomazzo B., 2013, Physical Review D, 88, 044020

Doggett J. B., Branch D., 1985, Astronomical Journal, 90, 2303

Dokuchaev V. I., Eroshenko Y. N., 2017, arXiv e-prints, p. arXiv:1701.02492

Dong Y.-Z., Gu W.-M., Liu T., Wang J., 2018, Monthly Notices of the Royal Astronomical Society, 475, L101

Drake J. J., Cohen O., Yashiro S., Gopalswamy N., 2013, Astrophysical Journal, 764, 170

Du S., Wang W., Wu X., Xu R., 2020, arXiv e-prints, p. arXiv:2004.11223

Duncan R. C., Thompson C., 1992, Astrophysical Journal Letters, 392, L9

Duque R., Daigne F., Mochkovitch R., 2019, Astronomy and Astrophysics, 631, A39

Dyson F. J., 1960, Science, 131, 1667

Eftekhari T., Berger E., 2017, Astrophysical Journal, 849, 162

Eftekhari T., Berger E., Williams P. K. G., Blanchard P. K., 2018, Astrophysical Journal, 860, 73

Egorov A. E., Postnov K. A., 2009, Astronomy Letters, 35, 241

Eichler D., Livio M., Piran T., Schramm D. N., 1989, Nature, 340, 126

Enßlin T. A., Frommert M., Kitaura F. S., 2009, Physical Review D, 80, 105005

Epstein R. I., Link B., 2000, Starquake-induced glitches in pulsars. Kluwer Academic Publishers, p. 95, doi:10.1007/978-94-010-0878-5_12

Evans P. A., et al., 2017, Science, 358, 1565

Ewen H. I., Purcell E. M., 1951, Nature, 168, 356

Faerman Y., Sternberg A., McKee C. F., 2017, Astrophysical Journal, 835, 52

Falcke H., Rezzolla L., 2014, Astronomy and Astrophysics, 562, A137

Fang T., Bullock J., Boylan-Kolchin M., 2013, Astrophysical Journal, 762, 20

Fang T., Buote D., Bullock J., Ma R., 2015, Astrophysical Journal Supplement Series, 217, 21

Farah W., et al., 2018, Monthly Notices of the Royal Astronomical Society, 478, 1209

Faucher-Giguère C.-A., Kaspi V. M., 2006, Astrophysical Journal, 643, 332

Filippenko A. V., 1997, Annual Review of Astronomy and Astrophysics, 35, 309

Fonseca E., et al., 2020, Astrophysical Journal Letters, 891, L6

Forman W., Kellogg E., Gursky H., Tananbaum H., Giacconi R., 1972, Astrophysical Journal, 178, 309

Frail D. A., Kulkarni S. R., Nicastro L., Feroci M., Taylor G. B., 1997, Nature, 389, 261

Frederiks D., et al., 2008, in Galassi M., Palmer D., Fenimore E., eds, American Institute of Physics Conference Series Vol. 1000, Gamma-ray Bursts 2007. pp 271–275, doi:10.1063/1.2943461

Frolov V. P., Vilkovsky G. A., 1982, in Marcel Grossmann Meeting: General Relativity. p. 455

Fruchter A. S., et al., 2006, Nature, 441, 463

Fukugita M., Hogan C. J., Peebles P. J. E., 1998, Astrophysical Journal, 503, 518

Fuller J., Ott C. D., 2015, Monthly Notices of the Royal Astronomical Society, 450, L71

Gaensler B. M., Madsen G. J., Chatterjee S., Mao S. A., 2008, Publications of the Astronomical Society of Australia, 25, 184

Gajjar V., et al., 2018, Astrophysical Journal, 863, 2

Gal-Yam A., 2019, Annual Review of Astronomy and Astrophysics, 57, 305

Gallant Y. A., Hoshino M., Langdon A. B., Arons J., Max C. E., 1992, Astrophysical Journal, 391, 73

Gao H., Li Z., Zhang B., 2014, Astrophysical Journal, 788, 189

Gao H., Zhang B., Lü H.-J., 2016, Physical Review D, 93, 044065

García-Bellido J., Linde A., Wands D., 1996, Physical Review D, 54, 6040

Gasser T., Müller H.-G., 1979, in Gasser T., Rosenblatt M., eds, Smoothing Techniques for Curve Estimation. Springer Berlin Heidelberg, Berlin, Heidelberg, pp 23–68

Gavriil F. P., Kaspi V. M., Woods P. M., 2002, Nature, 419, 142

Gelfand J. D., et al., 2005, Astrophysical Journal Letters, 634, L89

Gelman A., Carlin J. B., Stern H. S., Rubin D. B., 2014, Chapman & Hall, London

Geng J. J., Huang Y. F., 2015, Astrophysical Journal, 809, 24

Geng J.-J., Li B., Li L.-B., Xiong S.-L., Kuiper R., Huang Y.-F., 2020, Astrophysical Journal Letters, 898, L55

Getman K. V., Feigelson E. D., Broos P. S., Micela G., Garmire G. P., 2008a, Astrophysical Journal, 688, 418

Getman K. V., Feigelson E. D., Micela G., Jardine M. M., Gregory S. G., Garmire G. P., 2008b, Astrophysical Journal, 688, 437

Ghisellini G., Locatelli N., 2018, Astronomy and Astrophysics, 613, A61

Giacomazzo B., Perna R., 2013, Astrophysical Journal Letters, 771, L26

Gill R., Granot J., Lyubarsky Y., 2017, Monthly Notices of the Royal Astronomical Society, 474, 3535

Gold T., 1968, Nature, 218, 731

Goldreich P., Julian W. H., 1969, Astrophysical Journal, 157, 869

Goldstein A., et al., 2017, Astrophysical Journal, 848, L14

Gondek-Rosińska D., Gourgoulhon E., Haensel P., 2003, Astronomy and Astrophysics, 412, 777

Gourdji K., Michilli D., Spitler L. G., Hessels J. W. T., Seymour A., Cordes J. M., Chatterjee S., 2019, Astrophysical Journal Letters, 877, L19

Graham Smith F., Lyne A. G., Jordan C., 2011, Monthly Notices of the Royal Astronomical Society, 410, 499

Granot J., et al., 2006, Astrophysical Journal, 638, 391

Gregory P. C., Fahlman G. G., 1980, Nature, 287, 805

Gross M., Haroche S., 1982, Physics Reports, 93, 301

Gruzinov A., Levin Y., 2019, Astrophysical Journal, 876, 74

Gu W.-M., Dong Y.-Z., Liu T., Ma R., Wang J., 2016, Astrophysical Journal Letters, 823, L28

Gu W.-M., Yi T., Liu T., 2020, Monthly Notices of the Royal Astronomical Society, 497, 1543

Güdel M., 2002, Annual Review of Astronomy and Astrophysics, 40, 217

Gudel M., Benz A. O., Bastian T. S., Furst E., Simnett G. M., Davis R. J., 1989, Astronomy and Astrophysics, 220, L5

Guetta D., Granot J., 2003, Physical Review Letters, 90, 201103

Gupta P. D., Saini N., 2018, Journal of Astrophysics and Astronomy, 39, 14

Gursky H., Kellogg E. M., Leong C., Tananbaum H., Giacconi R., 1971, Astrophysical Journal Letters, 165, L43

Guseinov O. K., Zel'dovich Y. B., 1966, Soviet Astronomy, 10, 251

Gutenberg B., Richter C. F., 1936, Science, 83, 183

Haggard H. M., Rovelli C., 2015, Physical Review D, 92, 104020

Haggard D., Nynka M., Ruan J. J., Kalogera V., Cenko S. B., Evans P., Kennea J. A., 2017, Astrophysical Journal Letters, 848, L25

Hall P., Wehrly T. E., 1991, Journal of the American Statistical Association, 86, 665

Hallinan G., et al., 2017, Science, 358, 1579

Hani M. H., Ellison S. L., Sparre M., Grand R. J. J., Pakmor R., Gomez F. A., Springel V., 2019, Monthly Notices of the Royal Astronomical Society, 488, 135

Hankins T. H., 1972, Astrophysical Journal, 177, L11

Hardy L. K., et al., 2017, Monthly Notices of the Royal Astronomical Society, 472, 2800

Heger A., Fryer C. L., Woosley S. E., Langer N., Hartmann D. H., 2003, Astrophysical Journal, 591, 288

Heintz K. E., et al., 2020, Astrophysical Journal, 903, 152

Heitsch F., Putman M. E., 2009, Astrophysical Journal, 698, 1485

Helfand D. J., 1994, Monthly Notices of the Royal Astronomical Society, 267, 490

Henley D. B., Shelton R. L., Kwak K., Joung M. R., Mac Low M.-M., 2010, Astrophysical Journal, 723, 935

Hessels J. W. T., et al., 2019, Astrophysical Journal, 876, L23

Hewish A., Bell S. J., Pilkington J. D. H., Scott P. F., Collins R. A., 1968, Nature, 217, 709

Hill J. C., Baxter E. J., Lidz A., Greco J. P., Jain B., 2018, Physical Review D, 97, 083501

Hillebrandt W., Niemeyer J. C., 2000, Annual Review of Astronomy and Astrophysics, 38, 191

Hillebrandt W., Kromer M., Röpke F. K., Ruiter A. J., 2013, Frontiers of Physics, 8, 116

Hilmarsson G. H., et al., 2021, Astrophysical Journal Letters, 908, L10

Hobbs G., Lorimer D. R., Lyne A. G., Kramer M., 2005, Monthly Notices of the Royal Astronomical Society, 360, 974

Hoffmann T., Jones N. S., 2015, arXiv e-prints, p. arXiv:1512.03188

Hogan C., Rees M., 1988, Physics Letters B, 205, 228

Horne J. S., Garton E. O., 2006, Journal of Wildlife Management, 70, 641

Hoshino M., Arons J., Gallant Y. A., Langdon A. B., 1992, Astrophysical Journal, 390, 454

Hotokezaka K., Kiuchi K., Kyutoku K., Okawa H., Sekiguchi Y.-i., Shibata M., Taniguchi K., 2013, Physical Review D, 87, 024001

Houde M., Mathews A., Rajabi F., 2018a, Monthly Notices of the Royal Astronomical Society, 475, 514

Houde M., Rajabi F., Gaensler B. M., Mathews A., Tranchant V., 2018b, Monthly Notices of the Royal Astronomical Society, 482, 5492

Huang Y. F., Geng J. J., 2016, in Qain L., Li D., eds, Astronomical Society of the Pacific Conference Series Vol. 502, Frontiers in Radio Astronomy and FAST Early Sciences Symposium 2015. p. 1 (arXiv:1512.06519)

Huang Y. F., Lu T., 1997, Astronomy and Astrophysics, 325, 189

Huppenkothen D., et al., 2014a, Astrophysical Journal, 787, 128

Huppenkothen D., Heil L. M., Watts A. L., Göğüş E., 2014b, Astrophysical Journal, 795, 114

Hurley K., et al., 2005, Nature, 434, 1098

Inserra C., et al., 2018, Monthly Notices of the Royal Astronomical Society, 475, 1046

Ioka K., Zhang B., 2020, Astrophysical Journal Letters, 893, L26

Israel G. L., Mereghetti S., Stella L., 1994, Astrophysical Journal Letters, 433, L25

Israel G. L., et al., 2008, Astrophysical Journal, 685, 1114

Istomin Y. N., Komberg B. V., 2002, Astronomy Reports, 46, 908

Itoh N., 1970, Progress of Theoretical Physics, 44, 291

Iwazaki A., 1999, Physical Review D, 60, 025001

Iwazaki A., 2014, arXiv e-prints, p. arXiv:1412.7825

Iwazaki A., 2015, Physical Review D, 91, 023008

Iwazaki A., 2017, arXiv e-prints, p. arXiv:1707.04827

Iwazaki A., 2020, Progress of Theoretical and Experimental Physics, 2020

Jaikumar P., Meyer B. S., Otsuki K., Ouyed R., 2007, Astronomy and Astrophysics, 471, 227

Jeon Y., Kim J. H., 2013, Insurance: Mathematics and Economics, 53, 569

Jiang J.-C., Wang W.-Y., Luo R., Du S., Chen X., Lee K.-J., Xu R.-X., 2020, Research in Astronomy and Astrophysics, 20, 056

Jonas J., MeerKAT Team 2016, in MeerKAT Science: On the Pathway to the SKA. p. 1

Jones M. C., Marron J. S., Sheather S. J., 1996, Journal of the American Statistical Association, 91, 401

Josephy A., et al., 2019, Astrophysical Journal Letters, 882, L18

Kardashev N. S., Kuzmin A. D., Nikolaev N. Y., 1978, Soviet Astronomy, 22, 22

Kasen D., Bildsten L., 2010, Astrophysical Journal, 717, 245

Kashiyama K., Murase K., 2017, Astrophysical Journal Letters, 839, L3

Kashiyama K., Ioka K., Mészáros P., 2013, Astrophysical Journal Letters, 776, L39

Kaspi V. M., Beloborodov A. M., 2017, Annual Review of Astronomy and Astrophysics, 55, 261

Kaspi V. M., Gavriil F. P., Woods P. M., Jensen J. B., Roberts M. S. E., Chakrabarty D., 2003, Astrophysical Journal Letters, 588, L93

Katz J. I., 2017a, Monthly Notices of the Royal Astronomical Society, 467, L96

Katz J. I., 2017b, Monthly Notices of the Royal Astronomical Society, 469, L39

Katz J. I., 2017c, Monthly Notices of the Royal Astronomical Society, 471, L92

Katz J. I., 2018, Monthly Notices of the Royal Astronomical Society, 476, 1849

Katz J. I., Toole H. A., Unruh S. H., 1994, Astrophysical Journal, 437, 727

Kaup D. J., 1968, Physical Review, 172, 1331

Keane E. F., Petroff E., 2015, Monthly Notices of the Royal Astronomical Society, 447, 2852

Keane E. F., Kramer M., Lyne A. G., Stappers B. W., McLaughlin M. A., 2011, Monthly Notices of the Royal Astronomical Society, 415, 3065

Keane E. F., Stappers B. W., Kramer M., Lyne A. G., 2012, Monthly Notices of the Royal Astronomical Society, 425, L71

Keane E. F., et al., 2016, Nature, 530, 453

Keating L. C., Pen U.-L., 2020, Monthly Notices of the Royal Astronomical Society: Letters,

Keeney B. A., et al., 2017, Astrophysical Journal Supplement Series, 230, 6

Keith M. J., et al., 2010, Monthly Notices of the Royal Astronomical Society, 409, 619

Kellermann K. I., Pauliny-Toth I. I. K., 1969, Astrophysical Journal Letters, 155, L71

Kellogg E., Tananbaum H., Gursky H., Giacconi R., Pounds K., 1972, in Bulletin of the American Astronomical Society. p. 260

Kelly P. L., Kirshner R. P., 2012, Astrophysical Journal, 759, 107

Kettner C., Weber F., Weigel M. K., Glendenning N. K., 1995, Physical Review D, 51, 1440

Kibble T. W. B., 1976, Journal of Physics A Mathematical General, 9, 1387

King A. R., Pringle J. E., Wickramasinghe D. T., 2001, Monthly Notices of the Royal Astronomical Society, 320, L45

Kinney J. B., 2014, Physical ReviewE, 90, 011301

Kinney J. B., 2015, Physical Review E, 92, 032107

Kirsten F., Snelders M. P., Jenkins M., Nimmo K., van den Eijnden J., Hessels J. W. T., Gawroński M. P., Yang J., 2020, Nature Astronomy,

Kisaka S., Enoto T., Shibata S., 2017, Publications of the Astronomical Society of Japan, 69, L9

Klimenko S., Nikitin I., Nikitina L., 2017, International Journal of Modern Physics C, 28, 1750096

Kocherlakota P., Joshi P. S., Bhattacharyya S., Chakraborty C., Ray A., Biswas S., 2019, Monthly Notices of the Royal Astronomical Society, 490, 3262

Kocz J., Bailes M., Barnes D., Burke-Spolaor S., Levin L., 2012, Monthly Notices of the Royal Astronomical Society, 420, 271

Kolb E. W., Tkachev I. I., 1993, Physical Review Letters, 71, 3051

Kolb E. W., Tkachev I. I., 1994, Physical Review D, 50, 769

Kolb E. W., Tkachev I. I., 1996, Astrophysical Journal Letters, 460, L25

Kouveliotou C., Meegan C. A., Fishman G. J., Bhat N. P., Briggs M. S., Koshut T. M., Paciesas W. S., Pendleton G. N., 1993, Astrophysical Journal Letters, 413, L101

Kulkarni S. R., et al., 1998, Nature, 393, 35

Kulkarni S. R., Ofek E. O., Neill J. D., Zheng Z., Juric M., 2014, Astrophysical Journal, 797, 70

Kumar P., Bošnjak Ž., 2020, Monthly Notices of the Royal Astronomical Society, 494, 2385

Kumar H. S., Ibrahim A. I., Safi-Harb S., 2010, Astrophysical Journal, 716, 97

Kumar P., Lu W., Bhattacharya M., 2017, Monthly Notices of the Royal Astronomical Society, 468, 2726

Kumar P., et al., 2019, Astrophysical Journal Letters, 887, L30

Kundu E., Ferrario L., 2020, Monthly Notices of the Royal Astronomical Society, 492, 3753

LaMont C. H., Wiggins P. A., 2019, Physical Review E, 99, 052140

Lai D., 2012, Astrophysical Journal Letters, 757, L3

Landau L. D., 1932, Physikalische Zeitschrift der Sowjetunion, 1, 285

Lang K. R., 1986, Solar Physics, 104, 227

Lang K. R., Bookbinder J., Golub L., Davis M. M., 1983, Astrophysical Journal Letters, 272, L15

Lange C., Kramer M., Wielebinski R., Jessner A., 1998, Astronomy and Astrophysics, 332, 111

Law C. J., et al., 2017, Astrophysical Journal, 850, 76

Lawrence E., Vander Wiel S., Law C., Burke Spolaor S., Bower G. C., 2017, Astronomical Journal, 154, 117

Lea S. M., Silk J., Kellogg E., Murray S., 1973, Astrophysical Journal Letters, 184, L105

Lehner N., O'Meara J. M., Fox A. J., Howk J. C., Prochaska J. X., Burns V., Armstrong A. A., 2014, Astrophysical Journal, 788, 119

Lehner N., Howk J. C., Wakker B. P., 2015, Astrophysical Journal, 804, 79

Lemm J. C., 1999, arXiv e-prints, p. physics/9912005

Levin Y., Lyutikov M., 2012, Monthly Notices of the Royal Astronomical Society, 427, 1574

Levin Y., Beloborodov A. M., Bransgrove A., 2020, Astrophysical Journal Letters, 895, L30

Levkov D. G., Panin A. G., Tkachev I. I., 2020, Physical Review D, 102, 023501

Li L.-X., Paczyński B., 1998, Astrophysical Journal Letters, 507, L59

Li Y., Zhang B., 2020, Astrophysical Journal Letters, 899, L6

Li L.-B., Huang Y.-F., Geng J.-J., Li B., 2018, Research in Astronomy and Astrophysics, 18, 061

Li B., Li L.-B., Zhang Z.-B., Geng J.-J., Song L.-M., Huang Y.-F., Yang Y.-P., 2019a, arXiv e-prints, p. arXiv:1901.03484

Li D., Lin F. X., Main R., Pen U.-L., van Kerkwijk M. H., Yang I. S., 2019b, Monthly Notices of the Royal Astronomical Society, 484, 5723

Li C. K., et al., 2020a, arXiv e-prints, p. arXiv:2005.11071

Li Q.-C., Yang Y.-P., Dai Z.-G., 2020b, Astrophysical Journal, 896, 71

Liang C. J., Chen H.-W., 2014, Monthly Notices of the Royal Astronomical Society, 445, 2061

Lieu R., 2017, Astrophysical Journal, 834, 199

Lim S. H., Mo H. J., Li R., Liu Y., Ma Y.-Z., Wang H., Yang X., 2018, Astrophysical Journal, 854, 181

Lin H.-N., Sang Y., 2020, Monthly Notices of the Royal Astronomical Society, 491, 2156

Lin L., et al., 2012, Astrophysical Journal, 756, 54

Lingam M., Loeb A., 2017, Astrophysical Journal, 837, L23

Liu X., 2018, Astrophysics and Space Science, 363, 242

Liu X., 2020, arXiv e-prints, p. arXiv:2002.03693

Liu Q. Z., van Paradijs J., van den Heuvel E. P. J., 2005, Astronomy and Astrophysics, 442, 1135

Liu Q. Z., van Paradijs J., van den Heuvel E. P. J., 2006, Astronomy and Astrophysics, 455, 1165

Liu Q. Z., van Paradijs J., van den Heuvel E. P. J., 2007, Astronomy and Astrophysics, 469, 807

Liu T., Romero G. E., Liu M.-L., Li A., 2016, Astrophysical Journal, 826, 82

Loeb A., Shvartzvald Y., Maoz D., 2014, Monthly Notices of the Royal Astronomical Society, 439, L46

Lorimer D. R., 2011, SIGPROC: Pulsar Signal Processing Programs (ascl:1107.016)

Lorimer D. R., Bailes M., McLaughlin M. A., Narkevic D. J., Crawford F., 2007, Science, 318, 777

Lu W., Kumar P., 2018, Monthly Notices of the Royal Astronomical Society, 477, 2470

Lu W., Piro A. L., 2019, Astrophysical Journal, 883, 40

Lu W., Kumar P., Zhang B., 2020a, Monthly Notices of the Royal Astronomical Society, 498, 1397

Lu W., Piro A. L., Waxman E., 2020b, Monthly Notices of the Royal Astronomical Society, 498, 1973

Luan J., Goldreich P., 2014, Astrophysical Journal Letters, 785, L26

Luo R., Lee K., Lorimer D. R., Zhang B., 2018, Monthly Notices of the Royal Astronomical Society, 481, 2320

Luo R., Men Y., Lee K., Wang W., Lorimer D. R., Zhang B., 2020, Monthly Notices of the Royal Astronomical Society, 494, 665

Lyman J. D., et al., 2018, Nature Astronomy, 2, 751

Lyubarsky Y., 2010, Astrophysical Journal Letters, 725, L234

Lyubarsky Y., 2014, Monthly Notices of the Royal Astronomical Society, 442, L9

Lyubarsky Y., 2019, Monthly Notices of the Royal Astronomical Society, 483, 1731

Lyubarsky Y., 2020, Astrophysical Journal, 897, 1

Lyutikov M., 2015, Monthly Notices of the Royal Astronomical Society, 447, 1407

Lyutikov M., 2017, Astrophysical Journal Letters, 838, L13

Lyutikov M., 2020, Astrophysical Journal, 889, 135

Lyutikov M., Lorimer D. R., 2016, Astrophysical Journal Letters, 824, L18

Lyutikov M., McKinney J. C., 2011, Physical Review D, 84, 084019

Lyutikov M., Popov S., 2020, arXiv e-prints, p. arXiv:2005.05093

Lyutikov M., Burzawa L., Popov S. B., 2016, Monthly Notices of the Royal Astronomical Society, 462, 941

Lyutikov M., Barkov M. V., Giannios D., 2020, Astrophysical Journal Letters, 893, L39

MacFadyen A. I., Woosley S. E., Heger A., 2001, Astrophysical Journal, 550, 410

MacGibbon J. H., Brandenberger R. H., 1990, Nuclear Physics B, 331, 153

MacGibbon J. H., Brandenberger R. H., 1993, Physical Review D, 47, 2283

Macquart J. P., Ekers R. D., 2018, Monthly Notices of the Royal Astronomical Society, 474, 1900

Macquart J. P., Johnston S., 2015, Monthly Notices of the Royal Astronomical Society, 451, 3278

Macquart J. P., et al., 2020, Nature, 581, 391

Mahony E. K., et al., 2018, Astrophysical Journal Letters, 867, L10

Main R., van Kerkwijk M., Pen U.-L., Mahajan N., Vanderlinde K., 2017, Astrophysical Journal Letters, 840, L15

Main R., et al., 2018, Nature, 557, 522

Majid W. A., Pearlman A. B., Nimmo K., Hessels J. W. T., Prince T. A., Naudet C. J., Kocz J., Horiuchi S., 2020, Astrophysical Journal Letters, 897, L4

Malafarina D., 2017, Universe, 3, 48

Manchester R. N., Taylor J. H., 1977, Pulsars. W. H. Freeman

Manchester R. N., Hobbs G. B., Teoh A., Hobbs M., 2005, Astronomical Journal, 129, 1993

Manchester R. N., Fan G., Lyne A. G., Kaspi V. M., Crawford F., 2006, Astrophysical Journal, 649, 235

Maoz D., Loeb A., 2017, Monthly Notices of the Royal Astronomical Society, 467, 3920

Maoz D., Mannucci F., Nelemans G., 2014, Annual Review of Astronomy and Astrophysics, 52, 107

Maoz D., et al., 2015, Monthly Notices of the Royal Astronomical Society, 454, 2183

Marcote B., et al., 2017, Astrophysical Journal Letters, 834, L8

Marcote B., et al., 2020, Nature, 577, 190

Margalit B., Metzger B. D., 2016, Monthly Notices of the Royal Astronomical Society, 461, 1154

Margalit B., Metzger B. D., 2018, Astrophysical Journal Letters, 868, L4

Margalit B., Metzger B. D., 2019, Astrophysical Journal, 880, L15

Margalit B., Metzger B. D., Berger E., Nicholl M., Eftekhari T., Margutti R., 2018, Monthly Notices of the Royal Astronomical Society, 481, 2407

Margalit B., Berger E., Metzger B. D., 2019, Astrophysical Journal, 886, 110

Margalit B., Metzger B. D., Sironi L., 2020a, Monthly Notices of the Royal Astronomical Society, 494, 4627

Margalit B., Beniamini P., Sridhar N., Metzger B. D., 2020b, Astrophysical Journal Letters, 899, L27

Margutti R., et al., 2017, Astrophysical Journal Letters, 848, L20

Marnoch L., et al., 2020, Astronomy and Astrophysics, 639, A119

Marrone D. P., Moran J. M., Zhao J.-H., Rao R., 2007, Astrophysical Journal Letters, 654, L57

Marthi V. R., Gautam T., Li D., Lin H.-H., Main R., Naidu A. K., Pen U.-L., Wharton R., 2020, arXiv e-prints, p. arXiv:2007.14404

Martin D. C., et al., 2007, Astrophysical Journal Supplement Series, 173, 342

Masui K., et al., 2015, Nature, 528, 523

Mauch T., et al., 2020, Astrophysical Journal, 888, 61

Mazets E. P., Golentskii S. V., Ilinskii V. N., Aptekar R. L., Guryan I. A., 1979, Nature, 282, 587

Mazets E. P., et al., 1981, Astrophysics and Space Science, 80, 3

McWilliams S. T., Levin J., 2011, Astrophysical Journal, 742, 90

Mereghetti S., Stella L., 1995, Astrophysical Journal Letters, 442, L17

Mereghetti S., et al., 2020a, Astrophysical Journal Letters, 898, L29

Mereghetti S., Savchenko V., Gotz D., Ducci L., Ferrigno C., Bozzo E., Borkowski J., Bazzano A., 2020b, GRB Coordinates Network, 27668, 1

Mészáros P., Waxman E., 2001, Physical Review Letters, 87, 171102

Metzger B. D., et al., 2010, Monthly Notices of the Royal Astronomical Society, 406, 2650

Metzger B. D., Berger E., Margalit B., 2017, Astrophysical Journal, 841, 14

Metzger B. D., Margalit B., Sironi L., 2019, Monthly Notices of the Royal Astronomical Society, 485, 4091

Metzger B. D., Fang K., Margalit B., 2020, arXiv e-prints, p. arXiv:2008.12318

Michilli D., et al., 2018a, Monthly Notices of the Royal Astronomical Society, 476, 2704

Michilli D., et al., 2018b, Nature, 553, 182

Mingarelli C. M. F., Levin J., Lazio T. J. W., 2015, Astrophysical Journal Letters, 814, L20

Minkowski R., 1941, Publications of the Astronomical Society of the Pacific, 53, 224

Miralda-Escudé J., Cen R., Ostriker J. P., Rauch M., 1996, Astrophysical Journal, 471, 582

Misner C. W., 1972, Physical Review Letters, 28, 994

Mitra D., 2017, Journal of Astrophysics and Astronomy, 38, 52

Most E. R., Nathanail A., Rezzolla L., 2018, Astrophysical Journal, 864, 117

Mottez F., Heyvaerts J., 2011, Astronomy and Astrophysics, 532, A21

Mottez F., Heyvaerts J., 2020, Astronomy and Astrophysics, 639, C2

Mottez F., Zarka P., 2014, Astronomy and Astrophysics, 569, A86

Mottez F., Zarka P., Voisin G., 2020, arXiv e-prints, p. arXiv:2002.12834

Moustakas J., et al., 2013, Astrophysical Journal, 767, 50

Muller H., Wang J.-L., 1994, Biometrics, 50, 61

Murakami T., Tanaka Y., Kulkarni S. R., Ogasaka Y., Sonobe T., Ogawara Y., Aoki T., Yoshida A., 1994, Nature, 368, 127

Murase K., Kashiyama K., Mészáros P., 2016, Monthly Notices of the Royal Astronomical Society, 461, 1498

Murase K., Mészáros P., Fox D. B., 2017, Astrophysical Journal Letters, 836, L6

Müller H., 1991, Biometrika, 78, 521

Müller H., 1993, Scandinavian Journal of Statistics, 20, 313

Nakar E., 2007, Physics Reports, 442, 166

Narayan R., 1992, Philosophical Transactions of the Royal Society of London Series A, 341, 151

Narayan R., Paczynski B., Piran T., 1992, Astrophysical Journal Letters, 395, L83

Narlikar J. V., Rao K. M. V. A., Dadhich N., 1974, Nature, 251, 590

Nicastro F., et al., 2018, Nature, 558, 406

Nicholl M., Berger E., Margutti R., Blanchard P. K., Milisavljevic D., Challis P., Metzger B. D., Chornock R., 2017a, Astrophysical Journal Letters, 835, L8

Nicholl M., Williams P. K. G., Berger E., Villar V. A., Alexander K. D., Eftekhari T., Metzger B. D., 2017b, Astrophysical Journal, 843, 84

Niino Y., 2020, arXiv e-prints, p. arXiv:2005.12891

Nikitin I., 2018, arXiv e-prints, p. arXiv:1812.11801

Nikitin I., 2019, arXiv e-prints, p. arXiv:1906.09074

Nimmo K., et al., 2021, Nature Astronomy,

Norris J. P., Cline T. L., Desai U. D., Teegarden B. J., 1984, Nature, 308, 434

O'Meara J. M., Tytler D., Kirkman D., Suzuki N., Prochaska J. X., Lubin D., Wolfe A. M., 2001, Astrophysical Journal, 552, 718

Oganesyan G., Nava L., Ghirlanda G., Celotti A., 2017, Astrophysical Journal, 846, 137

Olinto A. V., 1987, Physics Letters B, 192, 71

Omand C. M. B., Kashiyama K., Murase K., 2018, Monthly Notices of the Royal Astronomical Society, 474, 573

Oostrum L. C., et al., 2020, Astronomy and Astrophysics, 635, A61

Oppermann N., Connor L. D., Pen U.-L., 2016, Monthly Notices of the Royal Astronomical Society, 461, 984

Osłowski S., et al., 2019, Monthly Notices of the Royal Astronomical Society, 488, 868

Osten R. A., Bastian T. S., 2008, Astrophysical Journal, 674, 1078

Ouyed R., Staff J., Jaikumar P., 2011, Astrophysical Journal, 729, 60

Ouyed R., Leahy D., Koning N., 2020a, Monthly Notices of the Royal Astronomical Society,

Ouyed R., Leahy D., Koning N., 2020b, Research in Astronomy and Astrophysics, 20, 027

Pacini F., 1967, Nature, 216, 567

Pakmor R., Kromer M., Röpke F. K., Sim S. A., Ruiter A. J., Hillebrandt W., 2010, Nature, 463, 61

Pakmor R., Kromer M., Taubenberger S., Sim S. A., Röpke F. K., Hillebrandt W., 2012, Astrophysical Journal Letters, 747, L10

Palaniswamy D., Li Y., Zhang B., 2018, Astrophysical Journal Letters, 854, L12

Palmer D. M., et al., 2005, Nature, 434, 1107

Pargner A., 2019, PhD thesis, KIT, Karlsruhe, IKP, doi:10.5445/IR/1000092362

Parrent J., Friesen B., Parthasarathy M., 2014, Astrophysics and Space Science, 351, 1

Paschalidis V., Etienne Z., Liu Y. T., Shapiro S. L., 2011a, Physical Review D, 83, 064002

Paschalidis V., Liu Y. T., Etienne Z., Shapiro S. L., 2011b, Physical Review D, 84, 104032

Pastor-Marazuela I., et al., 2020, arXiv e-prints, p. arXiv:2012.08348

Patel C., et al., 2018, Astrophysical Journal, 869, 181

Paterson K., et al., 2020, Astrophysical Journal Letters, 898, L32

Peccei R. D., Quinn H. R., 1977a, Physical Review D, 16, 1791

Peccei R. D., Quinn H. R., 1977b, Physical Review Letters, 38, 1440

Perley D. A., et al., 2016, Astrophysical Journal, 817, 8

Petroff E., et al., 2014, Astrophysical Journal Letters, 789, L26

Petroff E., et al., 2015a, Monthly Notices of the Royal Astronomical Society, 447, 246

Petroff E., et al., 2015b, Monthly Notices of the Royal Astronomical Society, 451, 3933

Petroff E., et al., 2016, Publications of the Astronomical Society of Australia, 33, e045

Petroff E., et al., 2017, Monthly Notices of the Royal Astronomical Society, 469, 4465

Petroff E., Hessels J. W. T., Lorimer D. R., 2019, The Astronomy and Astrophysics Review, 27, 4

Philippov A., Uzdensky D. A., Spitkovsky A., Cerutti B., 2019, Astrophysical Journal Letters, 876, L6

Philippov A., Timokhin A., Spitkovsky A., 2020, Physical Review Letters, 124, 245101

Phinney E. S., Kulkarni S. R., 1994, Annual Review of Astronomy and Astrophysics, 32, 591

Pines D., Shaham J., 1974, Comments on Astrophysics and Space Physics, 6, 37

Piro A. L., 2016, Astrophysical Journal Letters, 824, L32

Piro A. L., Burke-Spolaor S., 2017, Astrophysical Journal Letters, 841, L30

Piro A. L., Gaensler B. M., 2018, Astrophysical Journal, 861, 150

Piro A. L., Kulkarni S. R., 2013, Astrophysical Journal Letters, 762, L17

Planck Collaboration et al., 2013, Astronomy and Astrophysics, 557, A52

Planck Collaboration et al., 2014, Astronomy and Astrophysics, 571, A25

Planck Collaboration et al., 2016, Astronomy and Astrophysics, 594, A13

Platts E., Weltman A., Walters A., Tendulkar S. P., Gordin J. E. B., Kandhai S., 2019, Physics Reports, 821, 1

Platts E., Prochaska J. X., Law C. J., 2020, Astrophysical Journal Letters, 895, L49

Platts E., et al., 2021, submitted to MNRAS

Pleunis Z., et al., 2020, arXiv e-prints, p. arXiv:2012.08372

Plotnikov I., Sironi L., 2019, Monthly Notices of the Royal Astronomical Society, 485, 3816

Pols O., 1997, in Leung K.-C., ed., Astronomical Society of the Pacific Conference Series Vol. 130, The Third Pacific Rim Conference on Recent Development on Binary Star Research. p. 153

Popov S. B., 2020, Research Notes of the American Astronomical Society, 4, 98

Popov S. B., Postnov K. A., 2010, in Harutyunian H. A., Mickaelian A. M., Terzian Y., eds, Evolution of Cosmic Objects through their Physical Activity. pp 129–132 (arXiv:0710.2006)

Popov S. B., Postnov K. A., 2013, arXiv e-prints, p. arXiv:1307.4924

Popov S. B., Pshirkov M. S., 2016, Monthly Notices of the Royal Astronomical Society, 462, L16

Popov S. B., Postnov K. A., Pshirkov M. S., 2018, Physics Uspekhi, 61, 965

Press W. H., Teukolsky S. A., 1972, Nature, 238, 211

Prieto J. L., Stanek K. Z., Beacom J. F., 2008, Astrophysical Journal, 673, 999

Prochaska J. X., Tumlinson J., 2009, in Proceedings, Astrophysics in the Next Decade : The James Webb Space Telescope and Concurrent Facilities: Tucson, Arizona, September 24–27, 2007. pp 419–456, doi:10.1007/978-1-4020-9457-6_16

Prochaska J. X., Zheng Y., 2019, Monthly Notices of the Royal Astronomical Society, 485, 648

Prochaska J. X., Weiner B., Chen H.-W., Mulchaey J., Cooksey K., 2011, Astrophysical Journal, 740, 91

Prochaska J. X., et al., 2017, Astrophysical Journal, 837, 169

Prochaska J. X., et al., 2019, Science, 366, 231

Pshirkov M. S., 2017, International Journal of Modern Physics D, 26, 1750068

Punsly B., Bini D., 2016, Monthly Notices of the Royal Astronomical Society, 459, L41

Putman M. E., Peek J. E. G., Joung M. R., 2012, Annual Review of Astronomy and Astrophysics, 50, 491

Qiao G. J., Xue Y. Q., Xu R. X., Wang H. G., Xiao B. W., 2003, Astronomy and Astrophysics, 407, L25

Raby S., 2016, Physical Review D, 94, 103004

Rajabi F., Houde M., 2016a, Astrophysical Journal, 826, 216

Rajabi F., Houde M., 2016b, Astrophysical Journal, 828, 57

Rajabi F., Houde M., 2017, Science Advances, 3, e1601858

Rajabi F., Chamma M. A., Wyenberg C. M., Mathews A., Houde M., 2020, Monthly Notices of the Royal Astronomical Society, 498, 4936

Rajwade K., Chennamangalam J., Lorimer D., Karastergiou A., 2018, Monthly Notices of the Royal Astronomical Society, 479, 3094

Rajwade K., Mickaliger M., Stappers B., Caleb M., Breton R., Karastergiou A., Keane E., 2020a, arXiv e-prints, p. arXiv:2009.03795

Rajwade K. M., et al., 2020b, Monthly Notices of the Royal Astronomical Society, 495, 3551

Rane A., Lorimer D. R., Bates S. D., McMann N., McLaughlin M. A., Rajwade K., 2016, Monthly Notices of the Royal Astronomical Society, 455, 2207

Rauch M., 1998, Annual Review of Astronomy and Astrophysics, 36, 267

Ravasio M. E., Oganesyan G., Ghirlanda G., Nava L., Ghisellini G., Pescalli A., Celotti A., 2018, Astronomy and Astrophysics, 613, A16

Ravasio M. E., Ghirlanda G., Nava L., Ghisellini G., 2019, Astronomy and Astrophysics, 625, A60

Ravi V., 2019, Monthly Notices of the Royal Astronomical Society, 482, 1966

Ravi V., Shannon R. M., et al., 2016, Science, 354, 1249

Ravi V., et al., 2019, Nature, 572, 352

Rees M. J., 1977, Nature, 266, 333

Rickett B. J., 1990, Annual Review of Astronomy and Astrophysics, 28, 561

Ridnaia A., et al., 2020, The Astronomer's Telegram, 13688, 1

Rogers L. A., 2015, Astrophysical Journal, 801, 41

Romero G. E., del Valle M. V., Vieyro F. L., 2016, Physical Review D, 93, 023001

Rosa J. G., Kephart T. W., 2018, Physical Review Letters, 120, 231102

Rosswog S., 2005, Astrophysical Journal, 634, 1202

Rothschild R. E., Kulkarni S. R., Lingenfelter R. E., 1994, Nature, 368, 432

Rovelli C., Vidotto F., 2014, International Journal of Modern Physics D, 23, 1442026

Ruffini R., Bonazzola S., 1969, Physical Review, 187, 1767

Safarzadeh M., Prochaska J. X., Heintz K. E., Fong W.-f., 2020, arXiv e-prints, p. arXiv:2009.11735

Saint-Hilaire P., Benz A. O., Monstein C., 2014, Astrophysical Journal, 795, 19

Sakamoto T., Troja E., Lien A., Zhang B., Cenko S. B., Cunningham V., Berger E., 2020, arXiv e-prints, p. arXiv:2011.12555

Salem M., Besla G., Bryan G., Putman M., van der Marel R. P., Tonnesen S., 2015, Astrophysical Journal, 815, 77

Samiuddin M., El-Sayyad G. M., 1990, Biometrika, 77, 865

Sanidas S., Caleb M., Driessen L., Morello V., Rajwade K., Stappers B. W., 2018, in Pulsar Astrophysics the Next Fifty Years. pp 406–407, doi:10.1017/S1743921317009310

Sarazin C. L., Begelman M. C., Hatchett S. P., 1980, Astrophysical Journal Letters, 238, L129

Savage B. D., Narayanan A., Lehner N., Wakker B. P., 2011, Astrophysical Journal, 731, 14

Savaglio S., Glazebrook K., Borgne D. L., 2009, Astrophysical Journal, 691, 182

Savchenko V., et al., 2017, Astrophysical Journal Letters, 848, L15

Schnitzeler D. H. F. M., 2012, Monthly Notices of the Royal Astronomical Society, 427, 664

Scholz P., et al., 2016, Astrophysical Journal, 833, 177

Scholz P., et al., 2017, Astrophysical Journal, 846, 80

Schuster E., 1985, Communications in Statistics - Theory and Methods, 14, 1123

Schwab J., Quataert E., Kasen D., 2016, Monthly Notices of the Royal Astronomical Society, 463, 3461

Schwinger J., 1951, Physical Review, 82, 664

Seward F. D., Charles P. A., Smale A. P., 1986, Astrophysical Journal, 305, 814

Seymour A., Michilli D., Pleunis Z., 2019, ascl:1910.004

Shand Z., Ouyed A., Koning N., Ouyed R., 2016, Research in Astronomy and Astrophysics, 16, 80

Shannon R. M., Ravi V., 2017, Astrophysical Journal Letters, 837, L22

Shannon R. M., et al., 2018, Nature, 562, 386

Shen S., Mo H. J., White S. D. M., Blanton M. R., Kauffmann G., Voges W., Brinkmann J., Csabai I., 2003, Monthly Notices of the Royal Astronomical Society, 343, 978

Shen K. J., Bildsten L., Kasen D., Quataert E., 2012, Astrophysical Journal, 748, 35

Silverman B. W., 1986, Density Estimation for Statistics and Data Analysis. Chapman & Hall, London

Simard D., Ravi V., 2020, Astrophysical Journal Letters, 899, L21

Singh D., Wu K., Sarty G. E., 2014, Monthly Notices of the Royal Astronomical Society, 441, 800

Skare O., Blviken E., Holden L., 2003, Scandinavian Journal of Statistics, 30, 719

Skribanowitz N., Herman I. P., MacGillivray J. C., Feld M. S., 1973, Physical Review Letters, 30, 309

Smallwood J. L., Martin R. G., Zhang B., 2019, Monthly Notices of the Royal Astronomical Society, 485, 1367

Sob'yanin D. N., 2020, Monthly Notices of the Royal Astronomical Society, 497, 1001

Spergel D. N., et al., 2007, Astrophysical Journal Supplement Series, 170, 377

Spitler L. G., et al., 2014, Astrophysical Journal, 790, 101

Spitler L. G., et al., 2016, Nature, 531, 202

Spitler L. G., et al., 2018, Astrophysical Journal, 863, 150

Srednicki M., 1985, Nuclear Physics B, 260, 689

Stapledon O., 1937, Star Maker. Methuen

Stejner M., Madsen J., 2005, Physical Review D, 72, 123005

Stephens C. R., 't Hooft G., Whiting B. F., 1994, Classical and Quantum Gravity, 11, 621

Stocke J. T., Keeney B. A., Danforth C. W., Shull J. M., Froning C. S., Green J. C., Penton S. V., Savage B. D., 2013, Astrophysical Journal, 763, 148

Stone M., 1974, Journal of the Royal Statistical Society. Series B (Methodological), 36, 111

Stone M., 1977, Journal of the Royal Statistical Society. Series B (Methodological), 39, 44

Strateva I., et al., 2001, Astronomical Journal, 122, 1861

Sun S., Zhang Y.-L., 2020, arXiv e-prints, p. arXiv:2003.10527

Suresh A., Cordes J. M., 2019, Astrophysical Journal, 870, 29

Suvorov A. G., Kokkotas K. D., 2019, Monthly Notices of the Royal Astronomical Society, 488, 5887

Taam R. E., van den Heuvel E. P. J., 1986, Astrophysical Journal, 305, 235

Taggart K., Perley D., 2019, arXiv e-prints, p. arXiv:1911.09112

Tanenbaum B. S., Zeissig G. A., Drake F. D., 1968, Science, 160, 760

Tanvir N. R., Levan A. J., Fruchter A. S., Hjorth J., Hounsell R. A., Wiersema K., Tunnicliffe R. L., 2013, Nature, 500, 547

Tanvir N. R., et al., 2017, Astrophysical Journal Letters, 848, L27

Tavani M., et al., 2020, Astrophysical Journal Letters, 893, L42

Tendulkar S. P., et al., 2017, Astrophysical Journal Letters, 834, L7

Tendulkar S. P., et al., 2021, Astrophysical Journal Letters, 908, L12

Terrell G. R., Scott D. W., 1992, Ann. Statist., 20, 1236

Thirring H., 1918, Physikalische Zeitschrift, 19, 33

Thompson C., 2017a, Astrophysical Journal, 844, 65

Thompson C., 2017b, Astrophysical Journal, 844, 162

Thompson C., Duncan R. C., 1993, Astrophysical Journal, 408, 194

Thompson C., Duncan R. C., 1995, Monthly Notices of the Royal Astronomical Society, 275, 255

Thompson C., Duncan R. C., 1996, Astrophysical Journal, 473, 322

Thompson C., Duncan R. C., 2001, Astrophysical Journal, 561, 980

Thompson C., Lyutikov M., Kulkarni S. R., 2002, Astrophysical Journal, 574, 332

Thompson C., Yang H., Ortiz N., 2017, Astrophysical Journal, 841, 54

Thornton D., et al., 2013, Science, 341, 53

Thorsett S. E., 1992, IAU Colloquium, 128, 143

Tkachev I. I., 1986, Soviet Astronomy Letters, 12, 305

Tkachev I. I., 2015, Soviet Journal of Experimental and Theoretical Physics Letters, 101, 1

Tong H., Wang W., Wang H.-G., 2020, Research in Astronomy and Astrophysics, 20, 142

Totani T., 2013, Publications of the Astronomical Society of Japan, 65, L12

Tripp T. M., Savage B. D., Jenkins E. B., 2000, Astrophysical Journal Letters, 534, L1

Troja E., et al., 2017, Nature, 551, 71

Tumlinson J., et al., 2013, Astrophysical Journal, 777, 59

Tumlinson J., Peeples M. S., Werk J. K., 2017, Annual Review of Astronomy and Astrophysics, 55, 389

Tuntsov A. V., 2014, Monthly Notices of the Royal Astronomical Society, 441, L26

Turolla R., Zane S., Watts A. L., 2015, Reports on Progress in Physics, 78, 116901

Uzdensky D. A., Spitkovsky A., 2014, Astrophysical Journal, 780, 3

Vachaspati T., 2008, Physical Review Letters, 101, 141301

Valenti S., et al., 2017, Astrophysical Journal Letters, 848, L24

Van Waerbeke L., Zhitnitsky A., 2019, Physical Review D, 99, 043535

Vasisht G., Kulkarni S. R., Frail D. A., Greiner J., 1994, Astrophysical Journal Letters, 431, L35

Vedantham H. K., Ravi V., 2019, Monthly Notices of the Royal Astronomical Society, 485, L78

Vedantham H. K., Ravi V., Hallinan G., Shannon R. M., 2016, Astrophysical Journal, 830, 75

Vergani S. D., et al., 2015, Astronomy and Astrophysics, 581, A102

Vieyro F. L., Romero G. E., Bosch-Ramon V., Marcote B., del Valle M. V., 2017, Astronomy and Astrophysics, 602, A64

Viganò D., Rea N., Pons J. A., Perna R., Aguilera D. N., Miralles J. A., 2013, Monthly Notices of the Royal Astronomical Society, 434, 123

Vilenkin A., 1978, Physics Letters B, 78, 301

Vilenkin A., 1981, Physical Review Letters, 46, 1169

Wadiasingh Z., Timokhin A., 2019, Astrophysical Journal, 879, 4

Wadiasingh Z., Beniamini P., Timokhin A., Baring M. G., van der Horst A. J., Harding A. K., Kazanas D., 2020, Astrophysical Journal, 891, 82

Wang J., 2016, Advances in Astronomy, 2016, 3434565

Wang J.-S., Lai D., 2020, Astrophysical Journal, 892, 135

Wang J.-S., Yang Y.-P., Wu X.-F., Dai Z.-G., Wang F.-Y., 2016, Astrophysical Journal Letters, 822, L7

Wang W., Luo R., Yue H., Chen X., Lee K., Xu R., 2018, Astrophysical Journal, 852, 140

Wang W., Zhang B., Chen X., Xu R., 2019, Astrophysical Journal Letters, 876, L15

Wang F. Y., Wang Y. Y., Yang Y.-P., Yu Y. W., Zuo Z. Y., Dai Z. G., 2020a, Astrophysical Journal, 891, 72

Wang W.-Y., Xu R., Chen X., 2020b, Astrophysical Journal, 899, 109

Waxman E., 2017, Astrophysical Journal, 842, 34

Waxman E., Bahcall J., 1997, Physical Review Letters, 78, 2292

Werk J. K., Prochaska J. X., Thom C., Tumlinson J., Tripp T. M., Meara J. M., Peeples M. S., 2013, Astrophysical Journal Supplement Series, 204, 17

Werk J. K., et al., 2014, Astrophysical Journal, 792, 8

White S. D. M., Rees M. J., 1978, Monthly Notices of the Royal Astronomical Society, 183, 341

Williams P. K. G., Berger E., 2016, Astrophysical Journal Letters, 821, L22

Witten E., 1984, Physical Review D, 30, 272

Wong A. Y., 1977, Journal de Physique, 38, C6 27

Woosley S. E., Eastman R. G., 1997, in Ruiz-Lapuente P., Canal R., Isern J., eds, NATO Advanced Study Institute (ASI) Series C Vol. 486, Thermonuclear Supernovae. p. 821, doi:10.1007/978-94-011-5710-0_51

Xi S.-Q., Tam P.-H. T., Peng F.-K., Wang X.-Y., 2017, Astrophysical Journal Letters, 842, L8

Xu J., Han J. L., 2015, Research in Astronomy and Astrophysics, 15, 1629

Yamasaki S., Totani T., Kiuchi K., 2018, Publications of the Astronomical Society of Japan, 70, 39

Yamasaki S., Totani T., Kiuchi K., 2020, arXiv e-prints, p. arXiv:2010.07796

Yang Y.-H., Dai Z.-G., 2019, Astrophysical Journal, 885, 149

Yang Y.-P., Zhang B., 2016, Astrophysical Journal Letters, 830, L31

Yang Y.-P., Zhang B., 2017, Astrophysical Journal, 847, 22

Yang Y.-P., Zhang B., 2018, Astrophysical Journal, 868, 31

Yang Y.-P., Zhang B., Dai Z.-G., 2016, Astrophysical Journal Letters, 819, L12

Yao J. M., Manchester R. N., Wang N., 2017, Astrophysical Journal, 835, 29

Ye J., Wang K., Cai Y.-F., 2017, European Physical Journal C, 77, 720

Yi S.-X., Gao H., Zhang B., 2014, Astrophysical Journal Letters, 792, L21

Yoon S. C., Langer N., Norman C., 2006, Astronomy and Astrophysics, 460, 199

Yu Y.-W., Cheng K.-S., Shiu G., Tye H., 2014, Journal of Cosmology and Astroparticle Physics, 2014, 040

Yuan F., Lin J., Wu K., Ho L. C., 2009, Monthly Notices of the Royal Astronomical Society, 395, 2183

Yuan F., Bu D., Wu M., 2012, Astrophysical Journal, 761, 130

Yuan Y., Beloborodov A. M., Chen A. Y., Levin Y., 2020, Astrophysical Journal, 900, L21

Zadorozhna L. V., 2015, Advances in Astronomy and Space Physics, 5, 43

Zakharov V. E., 1972, Soviet Journal of Experimental and Theoretical Physics, 35, 908

Zanazzi J. J., Lai D., 2020, Astrophysical Journal Letters, 892, L15

Zel'Dovich Y. B., 1971, Soviet Journal of Experimental and Theoretical Physics Letters, 14, 180

Zhang B., 2014, Astrophysical Journal Letters, 780, L21

Zhang B., 2016, Astrophysical Journal Letters, 827, L31

Zhang B., 2017, Astrophysical Journal Letters, 836, L32

Zhang B., 2018, Astrophysical Journal Letters, 854, L21

Zhang B., 2020, Astrophysical Journal Letters, 890, L24

Zhang M., Low B. C., 2005, Annual Review of Astronomy and Astrophysics, 43, 103

Zhang Y., Geng J.-J., Huang Y.-F., 2018a, Astrophysical Journal, 858, 88

Zhang Y. G., Gajjar V., Foster G., Siemion A., Cordes J., Law C., Wang Y., 2018b, Astrophysical Journal, 866, 149

Zhang G. Q., Yi S. X., Wang F. Y., 2020a, Astrophysical Journal, 893, 44

Zhang S. N., et al., 2020b, The Astronomer's Telegram, 13687, 1

Zhitnitsky A. R., 2003, Journal of Cosmology and Astroparticle Physics, 2003, 010

Zhong S.-Q., Dai Z.-G., 2020, Astrophysical Journal, 893, 9

Zink B., Lasky P. D., Kokkotas K. D., 2012, Physical Review D, 85, 024030

Zouros T. J., Eardley D. M., 1979, Annals of Physics, 118, 139

Zwicky F., 1937, Astrophysical Journal, 86, 217

da Silva L. A. L., 1993, Astrophysics and Space Science, 202, 215

van Paradijs J., McClintock J. E., 1995, in X-ray Binaries. pp 58–125

van Paradijs J., Taam R. E., van den Heuvel E. P. J., 1995, Astronomy and Astrophysics, 299, L41

van Paradijs J., et al., 1997, Nature, 386, 686

van Putten T., Watts A. L., Baring M. G., Wijers R. A. M. J., 2016, Monthly Notices of the Royal Astronomical Society, 461, 877

van Straten W., Bailes M., 2011, Publications of the Astronomical Society of Australia, 28, 1

van Straten W., Demorest P., Oslowski S., 2012, Astronomical Research and Technology, 9, 237

van der Horst A. J., et al., 2012, Astrophysical Journal, 749, 122

van der Klis M., 2000, Annual Review of Astronomy and Astrophysics, 38, 717

APPENDIX A

Data Reduction Guide

The following steps were taken to clean and process the MeerKAT data in Chapter 4. I encountered numerous GCC compiling issues when trying to install SIGPROC on my local machine. As such, I used a Docker container[1] for filterbank and archive manipulation. In the following, angle brackets < > are used to denote user-specified input.

Filterbank files from MeerKAT were converted into archive files, which can be manipulated. The filterbank files were assigned values with which to generate the archive files (such as DM, number of bins, etc.) and were given details about the data (such as the telescope, file length and event names). The available filterbank details can be viewed using the `header` command in SIGPROC[2] (Lorimer, 2011):

```
➜ ~ header <filename>.fil
```

The archive files `<filename>.ar` were created by running:

```
➜ ~ dspsr <filename>.fil -c <filfile_length> -T <filfile_length> -k meerkat -D
    565 -b 16384 -N FRB121102
```

The dispersion measure (`-D`) of DM = 565 pc cm^{-3} is an approximate value from literature. The number of bins (`-b`) is such that the archive resolution is close to the native resolution of the telescope (306.24 µs). In other words, the duration of the filterbank ($t_{\rm filt}$) divided by the number of bins ($N_{\rm bin}$) should be approximately 306.24 µs:

$$\frac{t_{\rm filt}}{N_{\rm bin}} = \frac{4.5\,{\rm s}}{16834} = 267.316\,\mu{\rm s}\ . \tag{A..1}$$

Next, we used PSRCHIVE[3] (van Straten et al., 2012) to create RFI masks for the archives. For easy manipulation, we created a bin scrunched file using `pam`, but maintained the frequency resolution. `-b` dictates the factor by which to reduce the bins and `-e` creates a file with the extension `.B`. We ran `pazi`, which brings up an GUI to remove bad channels interactively.

```
➜ ~ pam -b 16 -e B <filename>.ar
```

```
➜ ~ pazi <filename>.B
```

Once clean, we pressed `p` to print a `paz` command and the channels to be zapped. We saved this in shell script `.sh`, e.g.

```
#!/bin/bash
paz "<channels>" -e zap <filename>.ar
```

Running the above will created a clean archive with the extension `.zap`. To view the archive:

```
➜ ~ psrplot -pfreq+ -jD <filename>.zap -c x:unit=bin -c y:reverse=1 -c
    x:win=<start:stop> -j "F 64"
```

[1] Available at https://github.com/scienceguyrob/Docker/tree/master/Images/pulsardsd.
[2] Latest version available at https://github.com/SixByNine/sigproc.
[3] Available at http://psrchive.sourceforge.net.

where `-c x:win=bin` is the x-axis in bins (or `-c x:win=ms` for milliseconds), `-c y:reverse=1` flips the y-axis to the correct orientation, `-c x:win=<start:stop>` is the bin window within which the pulse lies, and `-j "F 64"` scrunches in frequency to 64 channels.

To find the structure-optimised DM, we created multiple archives over a trial DM range of DM = 540−590 pc cm^{-3} with a step size of 0.1 pc cm^{-3}. To de-disperse to different DMs, used the `pam` command:

```
➔ ~ pam -e <DM>.dm -D -d <DM> -V <filename>.zap
```

where `-e` gives the extension name, `-D` is to de-disperse, and `-d` is the value to de-disperse to. To save the output to a text file, we ran:

```
➔ ~ pdv -F -t -jD <filename>.dm > <filename>.txt
```

Here, `-F` scrunches by frequency and `-t` prints the data as ASCII text. These commands were used in a shell script to de-disperse over the entire trial DM range. The `.txt` files were then ready for data analysis. See the documentation for `pdv` for more data options.